# QUANTIFICATION OF COLLAGEN FIBER ORGANIZATION IN BIOLOGICAL TISSUES AT CELLULAR AND MOLECULAR SCALES USING SECOND-HARMONIC GENERATION IMAGING

BY

RAGHU AMBEKAR RAMACHANDRA RAO

DISSERTATION

Submitted in partial fulfillment of the requirements
for the degree of Doctor of Philosophy in Electrical and Computer Engineering
in the Graduate College of the
University of Illinois at Urbana-Champaign, 2012

Urbana, Illinois

Doctoral Committee:

Professor J. Gary Eden, Chair
Professor Umberto Ravaioli
Assistant Professor Kimani Toussaint, Advisor
Assistant Professor Gabriel Popescu

**ABSTRACT**

Collagen is the most abundant structural protein found in the human body, and is responsible for providing structure and function to tissues. Collagen molecules organize naturally into structures called fibers on the scale of the wavelength of light and lack inversion symmetry, thus allowing for the process of second harmonic generation (SHG) when exposed to intense incident light. Consequently, SHG microscopy has been frequently employed in medicine and biology to obtain high-contrast 3D images of collagen fibers without the need for staining. Quantification of collagen fiber organization at the scales of the optical diffraction limit (cellular scales) and sub-diffraction limit (molecular scales) is quintessential for understanding structure and function, assessing the health of the tissue, and identifying traits of a specific disease or damage early. In this regard, we have developed two quantitative techniques: Fourier transform-second-harmonic generation (FT-SHG) imaging and generalized $\chi^2$ second-harmonic generation ($\chi^2$-SHG) imaging.

FT-SHG imaging involves extracting quantitative metrics through the application of spatial Fourier analysis on the images of collagen-based tissues obtained from an SHG microscope (cellular scale). Simple metrics such as preferred orientation, maximum spatial frequency, and fiber spacing are defined and used to quantify differences in collagen fiber organization among several porcine tissues: ear cartilage, trachea, and cornea. Further, we quantitatively compare the information content between SHG images obtained from the forward and backward direction for three tissue types: porcine tendon, sclera, and ear cartilage. We find that both signal types yield consistent information on the preferred orientation of collagen fibers and several overlapping peaks in the magnitude spectrum for these tissues. This strengthens the application of backward SHG imaging for potential clinical diagnostics.

In order to show that FT-SHG imaging can be used as a valuable diagnostic tool for real-world biological problems, we first investigate collagenase-induced injury in horse tendons. Clear differences in collagen fiber organization between normal and injured tendon are quantified. In particular, we observe that the regularly oriented organization of collagen fibers in normal tendons is disrupted in injured tendons leading to a more random organization. We also observe that FT-SHG microscopy is more sensitive in assessing tendon injury compared

to the conventional polarized light microscopy. The second study includes quantifying collagen fibers in cortical bone using FT-SHG imaging and comparing it with scanning electron microscopy (SEM). Further, as an example study, we show how FT-SHG imaging could be used to quantify changes in bone structure as a function of age. Some initial work and future directions for extending FT-SHG to 3D are also discussed.

The second technique, $\chi^2$-SHG imaging, takes advantage of the coherent nature of SHG and utilizes polarization to extract the second-order susceptibility (*d* elements) which provides information on molecular organization, i.e., it provides access to sub-diffractional changes "optically". We use $\chi^2$-SHG in combination with FT-SHG imaging to investigate a couple of biological problems. First, we quantify differences in collagen fiber organization between cornea and sclera of the eye in order to investigate their properties of transparency and opacity, respectively. We find from $\chi^2$-SHG imaging that there is no statistical difference in the values of *d* elements between cornea and sclera, indicating that the underlying collagen structure generating SHG from the two is similar at the level of detection of SHG microscopy. However, the difference lies in the spatial organization of these collagen fibers as observed from FT-SHG imaging. We find that cornea contains lamellae with patches of ordered and uniform diameter collagen fibers with axial order, which could be the reason for its transparent behavior. Conversely, there are no lamellae in sclera (i.e., no axial order), and fibers are thicker, denser, have inconsistent diameters, and possess relatively inhomogeneous orientations, leading to its opaque nature.

We also utilized the two techniques to assess differences in stromal collagen fibers for several human breast tissue conditions: normal, hyperplasia, dysplasia, and malignant. Using FT-SHG imaging, we note differences between malignant and other pathological conditions through the metric A.I. ratio. Using generalized $\chi^2$-SHG imaging, we observe structural changes in collagen at the molecular scale, and a particular *d* element showed a more sensitive differentiation between breast tissue conditions, except between hyperplasia and normal/dysplasia. We also find that the trigonal symmetry (*3m*) is a more appropriate model to describe collagen fibers in malignant tissues as opposed to the conventionally used hexagonal symmetry (*C6*). Furthermore, the percentage of abnormal collagen fibers could potentially be used as a metric for differentiating breast tissue conditions.

We also introduce a technique for extending $\chi^2$-SHG to fibers with curvature which is useful for generating $\chi^2$-image maps (in terms of *d* elements) instead of the conventional SHG intensity images. The spatial variations in *d* elements will provide additional information. For example, in breast cancer tissues, it may help in observing how fibers change from normal to malignant spatially, especially around region of cancerous cells. Finally, we discuss some of the interesting immediate and later future work of quantitative SHG imaging we aim to carry out in our lab.

*To my parents, A.V. Ramachandra Rao and J. Prameela Bai, my sister, Lakshmi Ambekar, my brother-in-law, Raghu Chelikavada, and my cute little nieces, Aksheytha Chelikavada and Adwytha Chelikavada.*

“Science is a way of thinking much more than it is a body of knowledge."

-Carl Sagan

“People are usually more convinced by reasons they discovered themselves than by those found by others.”

- Blaise Pascal

“The whole of science is nothing more than a refinement of everyday thinking.”

-Albert Einstein

## ACKNOWLEDGMENTS

It gives me pleasure to thank all those who have contributed to this thesis. First and foremost, I owe my deepest gratitude to my PhD advisor, Dr. Kimani Toussaint. It has been a privilege to be his first PhD student. He taught me not only how good experimental optics is done, but also how to manage time and priorities with research projects to do well in graduate school. I appreciate his constant support and guidance throughout, even during the tough times, that has made my PhD experience productive and stimulating. I have always enjoyed interacting with him, be it a regular discussion, or bouncing ideas (crazy or not) for grants, or just a regular chit-chat. I also appreciate him for giving me numerous chances to present at conferences and see some of the giants in optics. He has been more than an advisor for me; he never hesitated to offer guidance on career prospects and job search, and even picked me up from the train station when I first came to Champaign! I wish him, his wife, and son (and hopefully many more to join) a great future, both in professional and personal life.

The University of Illinois is a special place for me, and I thoroughly enjoyed my PhD studies here at a research institution that hosts some of the greatest minds. I have enjoyed taking classes here, and it was real joy to take classes from great teachers, particularly Dr. Gabriel Popescu and Dr. Gary Eden. I thank Dr. Popescu and Dr. Eden for explaining several complex concepts and equations in optics in the most intuitive and simplest way possible, often with practical examples. This has had a significant positive impact on the way I learn new things in optics and the way I work in the lab. I also thank Dr. Eden for offering me valuable advice on my job search and career prospects.

I also thank Dr. Umberto Ravaioli for being on my doctoral committee and for being available whenever I needed help. I also thank our collaborators, Dr. Rohit Bhargava, Dr. Iwona Jasiuk, and Dr. Amy Wagoner Johnson, for fruitful and insightful discussions that have had a positive impact in finishing the interesting research projects we have worked on. I also thank Dr. Mayandi Sivaguru and Donna Epps for valuable help with the microscope and cryostat machine at IGB. I also appreciate the generosity of Larry Schook and Laurie Rund, who provided fresh samples whenever they were needed.

I am extremely grateful to have enjoyed the time together with my fellow group members, former and current: Nalwanda Shamutete, Monal Mehta, David Luedke, Erik Misawa, Kaspar Ko, Santosh Tripathi, Brian Roxworthy, Mehdi Zaman, and Tony Lau. I will cherish all those philosophical chats on life, going to Chinese buffets, short relaxing strolls, and walks back to home, which have become regular habits in our schedules.

Finally, I would like to thank my parents, sister, brother-in-law, and nieces, who have always supported me in my endeavors, always given me the strength and encouragement to follow my dreams, and never left me in doubt of their love for me.

**TABLE OF CONTENTS**

# CHAPTER 1: INTRODUCTION

## 1.1 Overview

Collagen is the most abundant structural protein found in the human body, accounting for about one-third of the total protein mass [1, 2]. In particular, it is found in the extracellular matrix surrounding the cells. Collagen molecules organize into hierarchical fibrillar structures that form fiber bundles which display a high degree of spatial organization. These fibers can be found abundantly in cornea, tendon, bone, cartilage, and skin [3-8]. Depending on the way they organize, they provide diverse functions to the tissues. For example, they can organize in such a way that it provides optical transparency and flexibility to cornea, while it provides density and toughness to the bone [4, 6]. Besides providing structure and function, it also has a wide range of other functions such as tissue repair, cell regulation, adhesion, migration, angiogenesis, and tissue scaffolding [9, 10]. Since collagen is a vital component of the tissues, monitoring their structure and organization would provide a wealth of information regarding the health of the tissue. Moreover, collagen is known to be altered due to physical injury such as tendonitis or diseases such as keratoconus, osteogenesis imperfecta, and several types of cancers [11-14]. Alterations in collagen could also disrupt the cell-to-cell relations leading to aberrant behavior of the cells. Therefore, it is essential to monitor the collagen fiber organization and structure in order to understand its role within the tissue, assess the health of the tissue, detect early pathological changes, and eventually to develop treatments.

There are several ways of imaging collagen fiber organization through techniques such as magnetic resonance imaging (MRI), ultrasound, X-ray (or computed tomography), electron, and optical imaging [15-18]. Figure 1 shows a plot with rough estimates of the maximum spatial resolution and penetration depth for the commonly used imaging techniques. Note that the plot is based on their conventional types and does not include its special variants, e.g., sub-diffraction optical imaging. Depending on the research or clinical problem being studied, one imaging technique may be preferred over the other. For example, currently, whole body *in vivo* imaging can only be performed through MRI or X-ray. Even though optical imaging is far from imaging the whole body *in vivo* (limited by strong scattering and absorption of optical waves by tissue), it does offers several advantages. Firstly, it does not use ionizing

radiation, unlike x-rays and electron microscopy, thereby permitting relatively noninvasive imaging. Secondly, it provides high spatial resolution images (~ 200 nm - 1 μm) compared to magnetic resonance and ultrasound (~70 μm - 250 μm). And finally, it is the simplest in terms of experimental implementation and image interpretation among all. Interestingly, the attainable spatial resolution with optical imaging matches closely to the length scale of cells and sub-cellular features, the spatial scale over which many events in normal and disease-state biology are occurring.

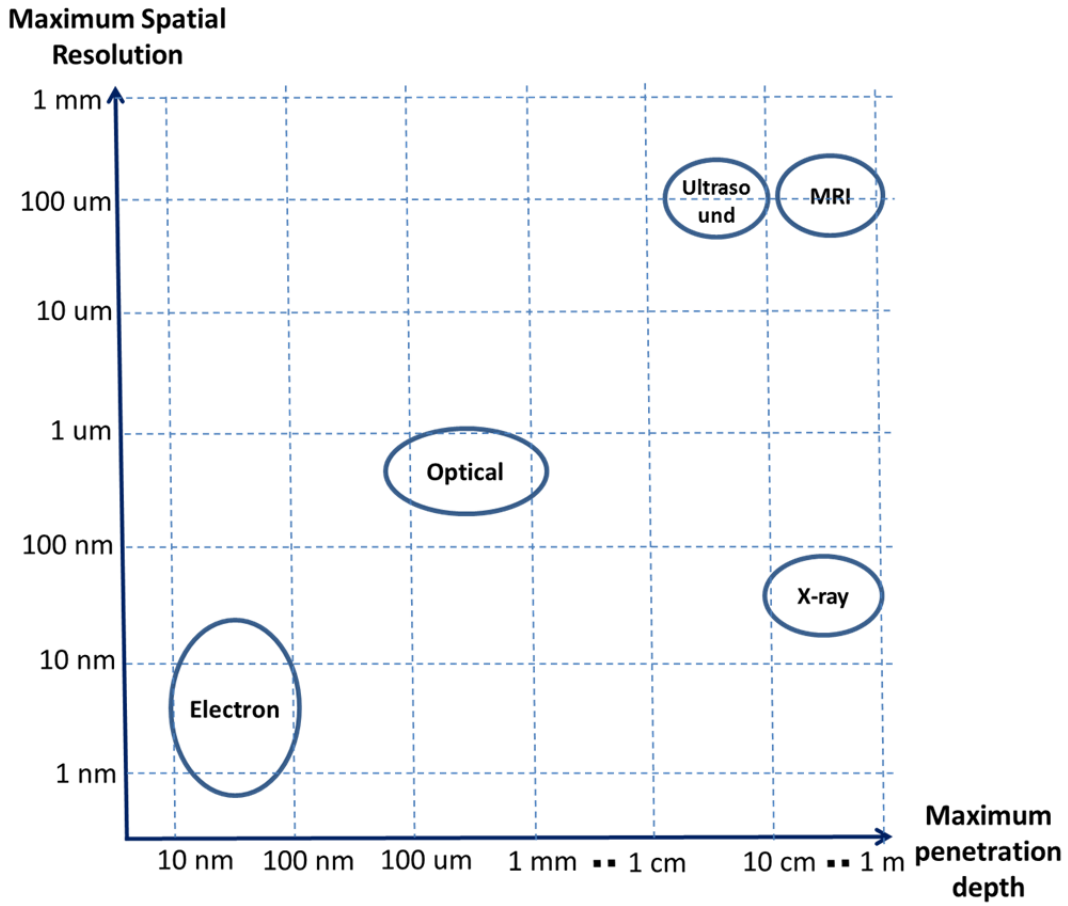


**Figure 1. Comparison of common imaging techniques in terms of maximum spatial resolution and penetration depth.**

Among all the optical imaging techniques, a nonlinear optical technique called second-harmonic generation (SHG) imaging is best suited for imaging collagen fibers [19-23]. This is because collagen fibers possess non-centrosymmetric structure and large second-order

susceptibility — conditions necessary for generation of strong SHG signal. Since SHG emission is intrinsic to collagen, all other biological structures appear dark, resulting in high-contrast images of collagen fibers without the need for staining. However, SHG being a nonlinear (second-order) optical process requires the high intensities, which are obtained through strong focusing and femtosecond pulses. Nevertheless, an advantage of SHG being a nonlinear optical process is that the generated signal is confined to a sub-femtoliter focal volume where the high intensity requirement is met, thereby permitting 3D imaging of collagen-based tissues. SHG microscopy has thus become a popular technique for obtaining high contrast 3D images of collagen fibers in biological tissues [19-21, 24-30].

Although there have been impressive advances in SHG imaging, most studies in the past have relied on the qualitative assessment of obtained images for analysis [27, 30, 31]. Recently, researchers have made major strides in developing quantitative metrics for this imaging modality [25, 28, 29, 32, 33]. Development of quantitative metrics is important since they result in a non-biased, more accurate, thorough, and faster analysis of the tissue structure as opposed to the qualitative evaluation that is frequently performed in hospitals. It also leads to extraction of sensitive changes in collagen fiber organization, and, thus, may help in early diagnosis. With regards to this, we have developed two quantitative second-harmonic generation techniques — Fourier transform-second-harmonic generation (FT-SHG) and generalized $\chi^2$-second-harmonic generation ($\chi^2$-SHG) imaging for quantifying collagen fiber organization in biological tissues at the cellular and molecular scales, respectively. FT-SHG imaging involves extracting quantitative metrics through the application of spatial Fourier analysis on the images of collagen-based tissues obtained from an SHG microscope. On the other hand, the second technique, $\chi^2$-SHG imaging, involves utilizing polarization to extract the second-order susceptibility which provides information on molecular organization.

### 1.2 Organization of Chapters

This thesis focuses on the aforementioned two quantitative second-harmonic generation techniques, especially their methodology, experimental implementation, analysis, and their diagnostic potential to real-world biological problems where the structure of collagen fibers

changes due to damage from disease or injury. The thesis is organized as follows: First, I will provide the necessary background material for collagen and second-harmonic generation in chapter 2. Then, in chapter 3, I will discuss the first technique, FT-SHG imaging, in detail. Specifically, the method of extracting quantitative metrics is provided in section 3.2 followed by details on the histological sample preparation (section 3.3.1) and experimental setup (section 3.3.2). I will then discuss the results obtained using FT-SHG imaging in section 3.4. I first introduce the technique for quantifying biological tissues such as ear cartilage, trachea, and cornea in section 3.4.1. In section 3.4.2, I discuss how FT-SHG imaging can be used to compare the information contained in forward and backward SHG images. Then, FT-SHG imaging is applied to solve a few biological problems (section 3.4). In particular, the technique is used to assess tendon injury in horses (section 3.4.3.1), and quantify bone structure with an example study (section 3.4.3.2). Later, the technique is used to understand fiber organization in cornea and sclera to investigate their properties of transparency and opacity, respectively (section 3.4.3.3). I also discuss a recent study we performed on breast cancer using FT-SHG imaging in section 3.4.3.4. Finally, I discuss the generalization of FT-SHG to three-dimensions (3D).

Chapter 4 focuses on the second technique, $\chi^2$-SHG. I first discuss the theory in section 4.2 followed by details on the experimental set up in section 4.3. I then provide the theory for generalizing $\chi^2$-SHG from *C6* to *3m* class symmetry (section 4.4), which we show is an appropriate way to model collagen fibers that have undergone damage or been affected by a disease. I then discuss the results obtained using generalized $\chi^2$-SHG in section 4.5 to study a few biological problems involving cornea and sclera (section 4.5.1.1), and breast cancer (section 4.5.1.2). I then discuss the sensitivity of $\chi^2$-SHG to fiber diameter in section 4.5.2. Finally, I discuss a method of obtaining $\chi^2$-image maps by extending the technique to account for curved fibers in section 4.5.3.

Chapter 5 discusses the results obtained from the combination of two techniques in understanding fiber organization in cornea and sclera (section 5.1), and breast cancer (section 5.2). I then discuss the general conclusions from the two techniques (section 5.3), and finally the future work in section 5.4

# CHAPTER 2: BACKGROUND

## 2.1 Collagen

In this section, a basic background on collagen is provided. Its fundamental structure and five classification groups are discussed. Then, we look at the biosynthesis of collagen inside the cell and how it is secreted into the extracellular space. The diseases that occur due to mutations in collagen gene are also listed. Finally, the current understanding of the role of collagen matrix in cancer metastasis is discussed.

### 2.1.1 Structure and composition

Figure 2 shows the structure of a collagen molecule known as tropocollagen [34-37]. Each molecule consists of three polypeptide chains (α-chains) possessing regular arrangement of amino acids conformed into a left-handed helix. Two sequences of amino acids are often observed: Glycine-Proline-X and Glycine-Y-Hydroxyproline, where X and Y are other amino acids. These left-handed helices are arranged into a right-handed triple helix structure held together by hydrogen bonds. Each tropocollagen is 1.5 nm in diameter and 300 nm long. There are at least 28 different types of collagens found in the human body [1, 10, 38, 39]. Over 90% of them is type I collagen and will be the focus for this thesis. The three α-chains forming the triple helix could be same (homotrimeric) as in Type II collagen or they may be different (heterotrimeric) as in Type I collagen [38].

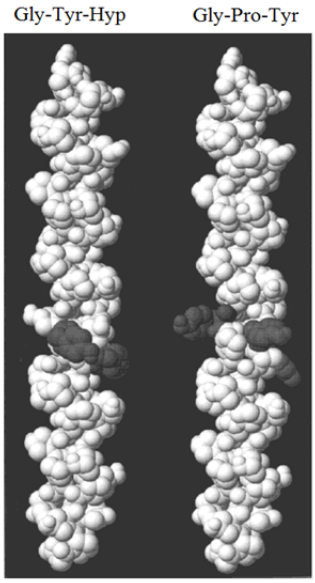


**Figure 2. Triple helical structure of the collagen molecule, tropocollagen [34].**

### 2.1.2 Classification and assembly of collagen

Collagens are classified based on their function and organization. They are fibril-forming, network-forming, fibril-associated, beaded-filament, and anchoring collagens [38].

#### *2.1.2.1 Fibril-forming collagens*

Fibrillar collagens (or fibrillar collagen) are found abundantly in the human body, particularly in tissues such as skin, bone, tendon, and cornea. These collagens are long rope-like structures which have no interruptions in the triple helix and they regularly arrange to form the characteristic banded structures as shown in Fig. 3a [10]. Each unit is called "D" and has a period of 67 nm as observed from the electron microscopy image in Fig. 3b. The diameter of these fibrils ranges from 50 to 500 nm depending on the tissue. The fibril-forming collagens are stabilized by covalent cross-links that involve amino acids in the triple helix [40]. These cross-links are the chief source of tensile strength in most collagen-based tissues. Examples of fibril-forming collagens include collagen type I, II, III, V, and XI.

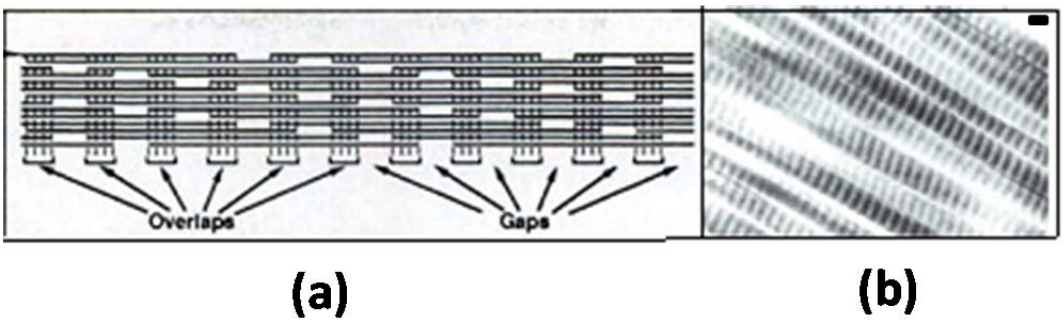


**Figure 3. Fibril-forming collagen. (a) There are no interruptions in the triple helix forming a regular arrangement of collagen molecules. (b) A transmission electron microscope image of the characteristic 67-nm 'D' bands of fibril-forming collagens [10]. Scale bar: 100 nm.**

Figure 4 summarizes the hierarchical organization of fibrillar collagens [1]. The three α-chains form collagen molecule, which in turn organize to form fibrils. These collagen fibrils further aggregate to form fibers, whose diameters range from 0.25 - 100 μm depending on the tissue and its location.

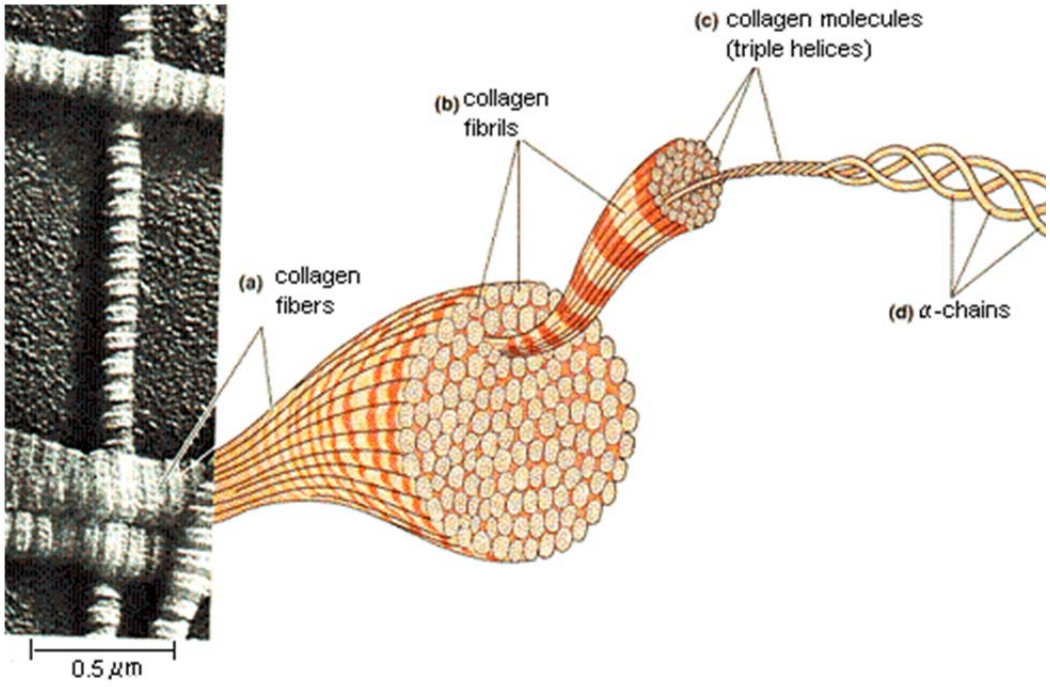


**Figure 4. Hierarchy of fibrillar collagen: α-chains, triple helices, fibrils and fibers [1].**

*2.1.2.2 Network-forming collagens*

As the name indicates, network-forming collagens form sheets or networks as shown in Fig. 5a [10]. The network is formed by the interactions between two trimeric N domains resulting in a hexamer which is stabilized by covalent cross-links [41]. Four collagen molecules then establish cross-links between them and other groups resulting in an extended network. Figure 5b shows an electron microscope image of the basement membrane, which is a typical example of network-forming collagens.

Examples of network-forming collagens include collagen types IV, VIII, and X. They are found in basement membrane (collagen IV), Descemet's membrane (collagen VIII) in the cornea of the eye, and growth-plate cartilage (collagen X) in the knee [42, 43]. The main function of network-forming collagen is molecular filtration and protection.

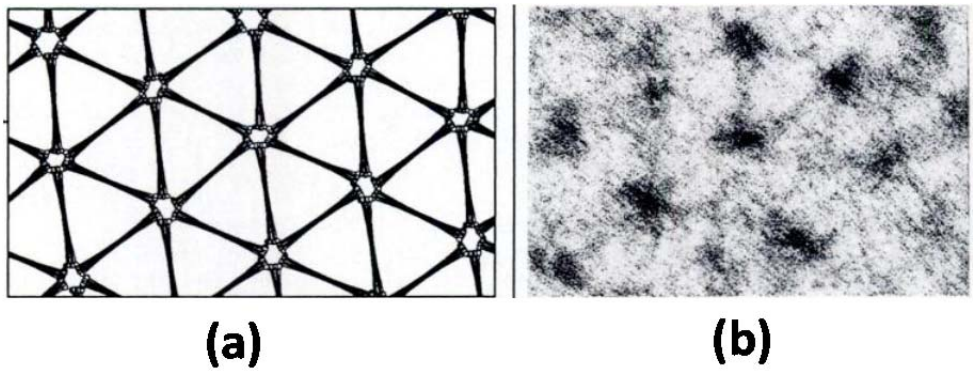


**Figure 5. Network-forming collagen. (a) Network-like arrangement of collagen molecules. (b) Electron microscope image of the basement membrane [10].**

*2.1.2.3 Fibril-associated collagens with interrupted triple helices (FACITs)*

Figure 6 shows the individual molecules of fibril-associated collagens and their assembly [10]. Fibril-associated collagens are short collagens with interrupted triple helices as shown in Fig. 6a. They can also be covalently linked to type II collagen and carry a glycosaminoglycans side chain. They are found at the surface of fibril-forming collagens such as Type II collagen as shown in Fig. 6b. They serve as means of attachment of new

functionalities to the fibrillar collagen. An electron microscope image of a *FACIT* is shown in Fig. 6c. Examples of fibril-associated collagens include collagen type XI, XII, and XIV.

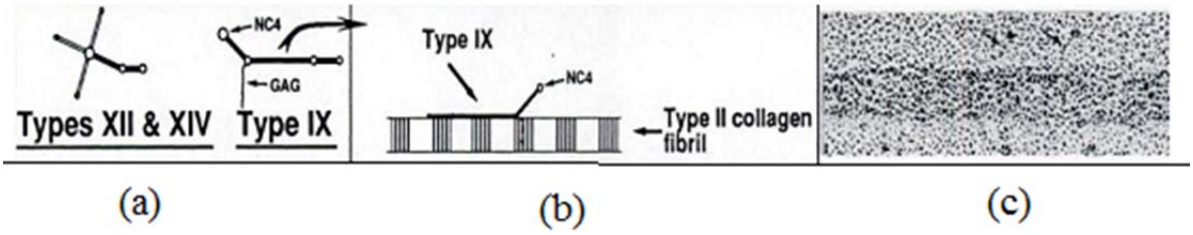


**Figure 6. Fibril-associated collagens. (a) Individual fibril-associated collagen molecule contains interruptions and a glycosaminoglycan side chain. (b) Covalent linkage to Type II collagen. (c) An electron microscope image showing a *FACIT* [10].**

*2.1.2.4 Anchoring collagens*

Anchoring collagens are one of the least understood collagens. Their overall structure and mode of aggregation are shown in Figure 7. The molecules form dimers, which in turn aggregate to form an anchoring fibril as shown in Fig. 7a, thus providing integrity by holding the interstitial collagen fibrils in the stroma with the basement membrane epithelium [44]. An electron microscope image in Fig. 7b shows an anchoring fibril connected to the basement membrane and trapping a collagen fibril. The ends, NC1 domains are responsible for binding the anchoring fibril to the collagen type IV of the basement membrane. One good example of an anchoring collagen is collagen type VII.

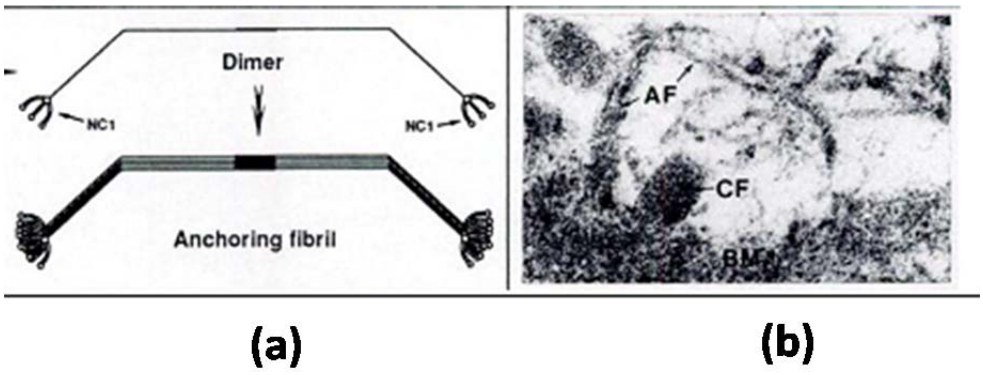


**Figure 7. (a) Anchoring collagen molecule contains interruption and aggregate as dimers which in turn form fibrils. (b) EM image of an anchoring fibril connected to the basement membrane [10].**

*2.1.2.5 Beaded filament-forming collagens*

Type VI collagen is a typical beaded filament-forming collagen. It is found in most tissues where it forms structural links with cells. An individual beaded filament–forming molecule has a short triple helical domain with noticeable globular ends as shown in Fig. 8a. Collagen VI dimers crosslink into tetramers through antiparallel association to assemble into long molecular chains known as beaded microfibrils, which have a beaded repeat of 105 nm (see Fig. 8b) [45].

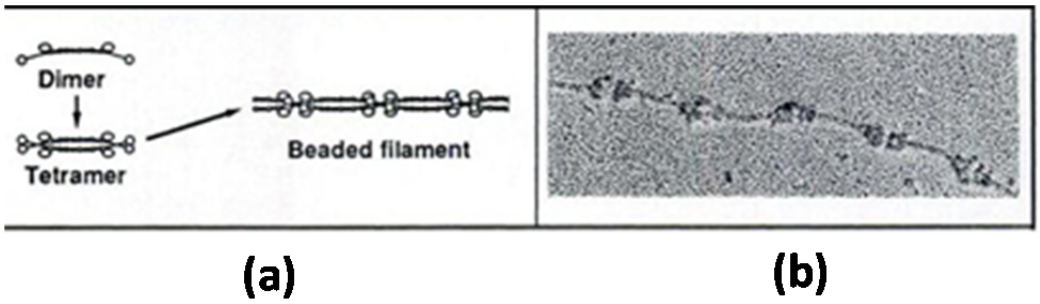


**Figure 8. Beaded filament-forming collagens. (a) Individual beaded filament-forming collagen molecules aggregate as tetramers, which in turn form beaded filaments by associating its extremes. (b) EM image showing a beaded filament fibril [10].**

### 2.1.3 Collagen fiber biosynthesis

The biosynthesis of collagen fibers involves several steps that include both intracellular and extracellular events as shown in the Fig. 9. The steps are listed below [1].

1. First, individual polypeptide chains (pro-α chains) are synthesized by membrane-bound ribosomes. These pro-α chains are then transported into the endoplasmic reticulum.
2. Then, selected aminoacids, prolines and lysines within the α-chains undergo hydroxylation. This process forms interchain hydrogen bonds that help stabilize the triple-helix structure.
3. Then, selected aminoacids called hydroxylysines undergo glycosylation, which helps the α-chains fold correctly.
4. Then, the three α-chains start self-assembling.
5. The self-assembly process completes to form a triple-helical structure called procollagen, which is a precursor for collagen molecule.
6. Procollagen is then packaged into secretory vesicles within the Golgi apparatus and secreted into the extracellular space.
7. The propeptide of the procollagen is cleaved and forms tropocollagen which is nothing but a collagen molecule.
8. Collagen molecules then undergo further self-assembly to form collagen fibrils, which have a diameter of ~ 10 - 300 nm.
9. Collagen fibrils further aggregate to form collagen fibers of diameters in the range 0.5 - 3 μm.

The information on the arrangement of fibrils in tissues is encoded in the chain recognition sequence of C-propeptides, which are shown in the Fig. 10 [46]. In tendons, the type I collagen fibrils align parallel to each other and form banded and crimped bundled structure, whereas in the skin, the fibrils are more random with a complex network of interlaced fibrils. Hydrophobic and electrostatic forces are also involved in the arrangement of collagen molecules to form fibrils. The fibrils are further stabilized by intermolecular covalent cross-links which contribute to the overall physical and mechanical properties of collagen fibers [47].

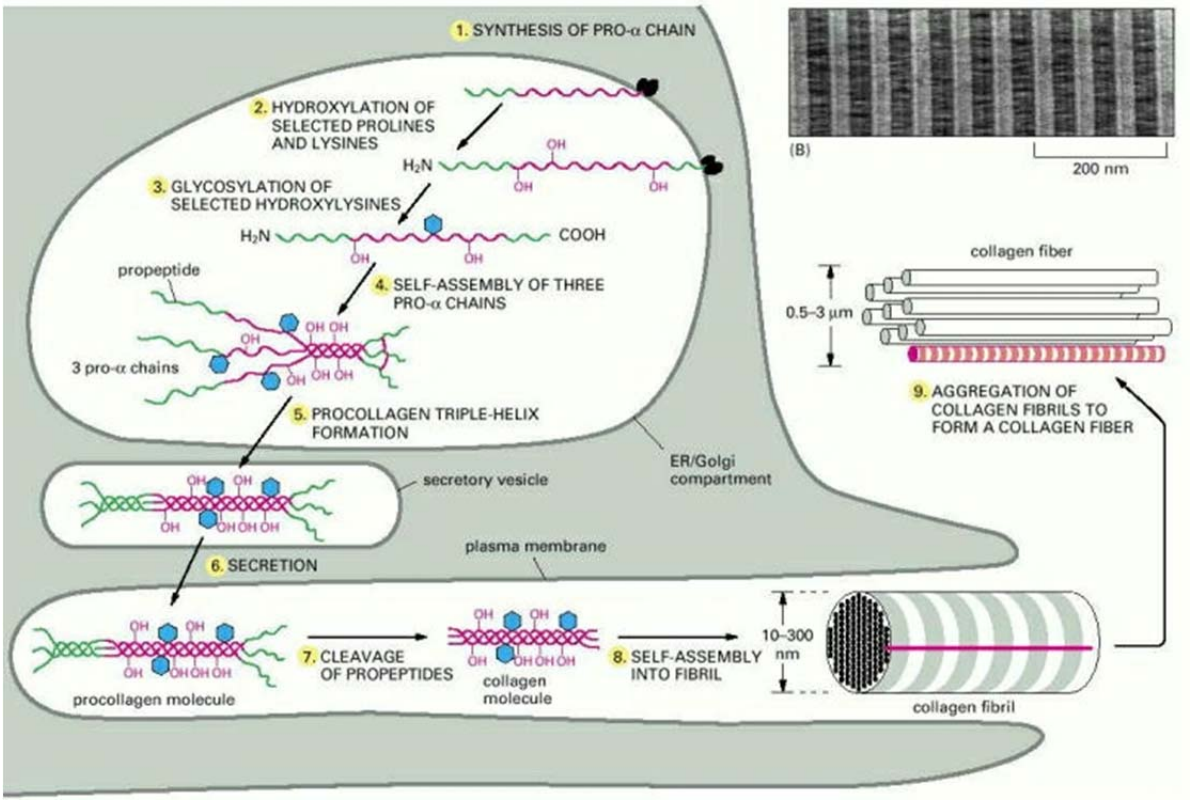


**Figure 9. Steps involved in the biosynthesis of collagen fiber [1].**

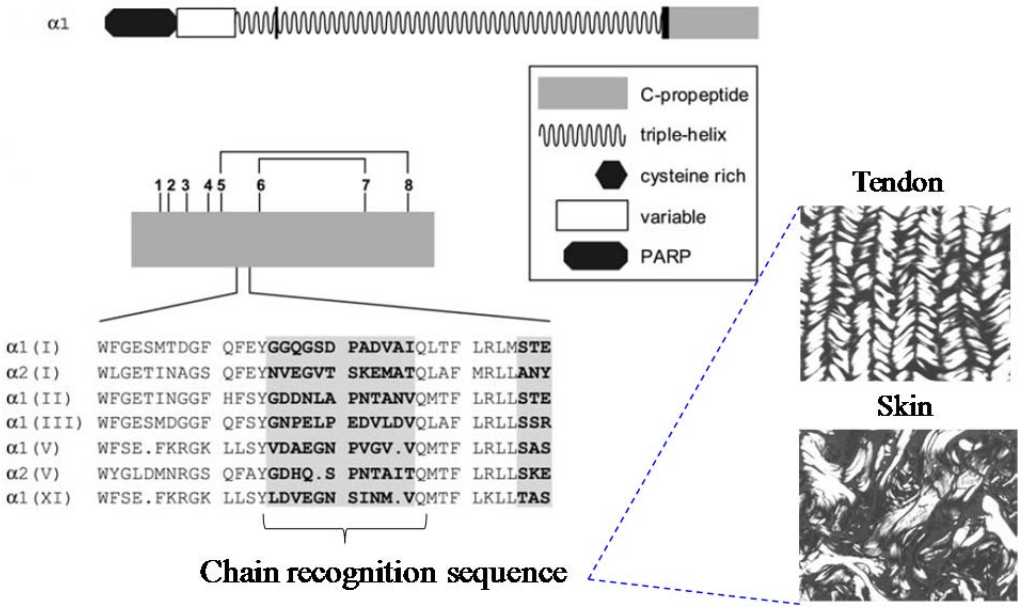


**Figure 10. Fibril assembly is determined by chain recognition sequence [46].**

### 2.1.4 Diseases associated with collagen

Collagen gene mutations are rare since collagen is an important structural protein and is well preserved in the human body through evolution. However, when mutations occur, they usually result in detectable disorders. Table 1 summarizes some common diseases associated with collagen [48, 49]. The table only includes diseases that arise due to mutations in collagen; however, in many diseases such as cancer, collagen has been recognized as being important for the initiation and progression [12, 50].

**Table 1. Summary of some common collagen disorders.**

| Disease | Mutated collagen | Brief description of disease |
|---|---|---|
| Osteogenesis imperfecta | Types I | Characterized by fragile bones, reduced bone mass, blue sclera, and hearing loss |
| Ehlers-Danlos Syndrome | Types I and V | Fragile and tender skin, easy bruising and atrophic injury |
| Alport syndrome | Type IV | Affects some of the basal membranes and is characterized by renal failure, loss of hearing and lens abnormalities |
| Epidermolysis Bullosa | Types VII and XVII | Blistering of the skin and mucous membranes due to small injury |
| Bethlem myopathy | Type VII | Muscle weakness and distal joint contractures |
| Arterial aneurysms | Type III | Weakening of the vessel wall leading to hemorrhage in heart and brain |
| Stickler syndrome | Types II, IX and XI | Distinctive facial appearance, eye abnormalities, hearing loss, and joint problems |

### 2.1.5 Role of collagen in metastasis

#### *2.1.5.1 Metastasis*

Metastasis is the spread of cancer from a primary tumor site to distant (secondary) sites in the body. It is the defining feature of cancer and involves several sequential steps as shown in the Fig. 11 [51]. They are: escape of the tumor cells from the primary tumor site (invasion), entry

into the blood circulation system (intravasation), survival and transportation within the circulation system, exit out of the circulation (extravasation), and growth of tumor cells at the secondary tumor site. The cancerous cells grow abnormally at the both the primary and secondary tumor sites, and this requires the recruitment of blood vessels and development of resistance to the immune system (angiogenesis). Only a fraction of the cancerous cells succeed in formation of metastasis, making it an inefficient process. In principle, cancer could be treated if any one of these steps is interrupted. However, it is a complex process. Several players take part in metastasis, and what makes it complicated is the fact that the players can either assist or promote cancer depending on its stage.

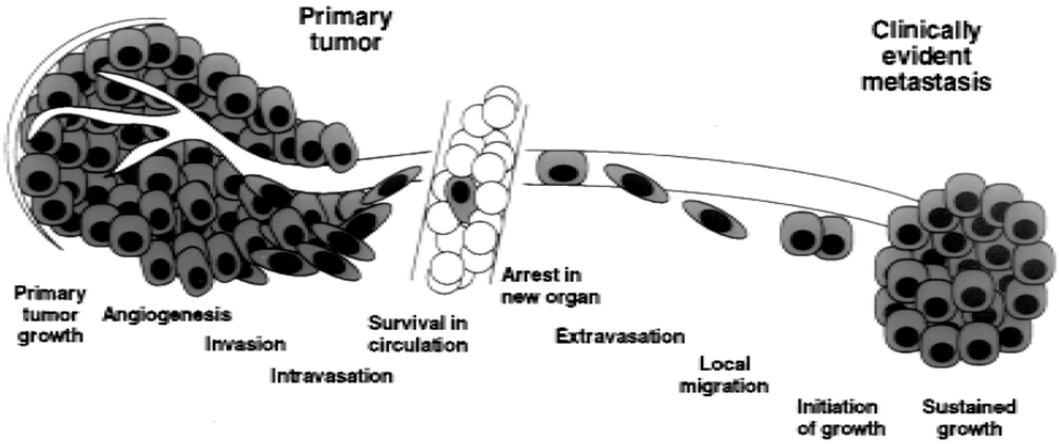


**Figure 11. Steps involved in metastasis [51].**

*2.1.5.2 Role of collagen matrix in metastasis and tumor growth*

Both the cellular and non-cellular components of the tissue are actively involved in metastasis. While the cellular components such as fibroblasts, endothelial cells, and mesenchymal stem cells directly affect the different stages of metastasis, the non-cellular components such as extracellular matrix (mainly collagen) and hypoxia (deficiency of oxygen) affect either directly by disrupting the tissue integrity and promoting tumor invasion, or indirectly through angiogenesis by promoting tumor cell survival and growth [44, 52-54]. There are several review articles covering the importance of cellular components to metastasis [55-57]. Here, I briefly summarize some important concepts regarding the role of extracellular matrix (in particular, collagen) in metastasis.

The extracellular matrix is a three-dimensional structure surrounding the cell and consists of two major components: basement membrane and interstitial matrix. The basement membrane underlies the epithelium and endothelium and is predominantly made of collagen type IV and reticular collagen type III [43]. The interstitial matrix which makes up the majority of the ECM is responsible for the mechanical strength of the tissue. It consists of mainly collagen type I and III, and other components such as febronectin and proteoglycans [58]. The collagen matrix regulates the cell behavior by providing it with external mechanical or chemical stimuli. However, during tumor growth, the collagen matrix undergoes remodeling in both its structure and composition, and also disrupts cell-cell relations leading to malignant behavior of the cells.

A family of extracellular proteinases called matrix metalloproteinases (MMPs) also plays a major role in metastasis. MMPs are capable of digesting the ECM and basement membrane under physiologic conditions, which is essential for tumor cell growth and migration [59]. Usually, experiments have found that at the tumor sites, there are increased levels of MMPs and reduced levels of TIMPs (tissue inhibitors of metalloproteinases) [60]. Hence, pharmacological inhibition of MMPs was thought to cure cancers. However, the clinical uses of these products were not successful since metastasis is a far more complicated process. The contribution of MMPs to collagen denaturation in every stage and type of cancer needs to be well understood.

## 2.2 Second-Harmonic Generation

In this section, I first discuss briefly the regime of nonlinear optics and some common nonlinear microscopy techniques. Then, I provide the theory of second-harmonic generation (SHG) from first principles, starting from Maxwell's equations. I then discuss how phase matching is achieved in crystals in order to generate strong SHG signal. Later, I discuss how SHG can also be generated from biological tissues through non-perfect phase matching. A qualitative picture of dipole SHG emission and its predominant forward emission is explained. Finally, an experimental setup of the SHG microscope and its advantages and disadvantages are discussed.

### 2.2.1 Introduction

Nonlinear optics deals with the interaction between optical fields in a nonlinear medium. Such interaction between fields is prohibited under low optical intensities, in which case the medium is treated linearly, and the properties of the medium such as refractive index and absorption coefficient are effectively independent of intensity; optical phenomena that fall under this category are referred to as linear optics. However, under high intensities (~$10^6$ - $10^{14}$ W/cm$^2$) the medium properties become intensity dependent, and as a result the medium acts as a mediator for interaction between optical fields. This is the domain of nonlinear optics, and media that facilitate this interaction are referred to as nonlinear. Nonlinear optical processes were observed only after the advent of lasers, which could provide the required high intensities.

To further elucidate things, consider a Lorentz oscillator model. In this classical harmonic oscillator model, an electron (charge) is viewed as being bound to a much more massive atom (nucleus) by a hypothetical spring. When an oscillating electromagnetic field (light) is incident on this system, the electron experiences a force due to the electric field that causes it to oscillate at the frequency of the incident light. This oscillating electron in turn generates a wave at the same frequency as that of the incident light. This process is commonly referred to as Rayleigh scattering, and can be described by Hooke's law when operating in the linear regime. However, in the nonlinear regime, the applied force is such that Hooke's law is no

longer valid, and additional frequencies can be produced by the oscillating spring. Depending on the strength of the nonlinearity, many different nonlinear effects can arise. The focus of this chapter is to discuss second-harmonic generation (SHG), a specific case of a degenerate three-wave mixing process, and its application to microscopy.

### 2.2.2 Nonlinear microscopy

Traditionally, two-photon fluorescence microscopy has been the most commonly used nonlinear microscopy technique. However, in the past decade, second-harmonic generation microscopy has gained popularity in imaging specific biological structures due to the following advantages: 1) reduced phototoxicity; 2) inherent (endogenous) contrast; 3) preservation of phase information; and 4) specificity to molecular structure organization. The first three points can be understood by invoking the use of the Jablonski diagram as shown in the Fig. 12, and comparing to the cases of one- and two-photon fluorescence. In linear (one-photon) fluorescence, a fluorophore is driven into an excited energy (electronic) state upon absorption of a photon. Subsequently, some of this energy is lost via vibrational relaxation and then re-radiated as a photon of lower energy as the fluorophore returns to its ground state (shown in Fig. 12a). Alternatively, as shown in Fig. 12c, this process can be carried out if one were to use two photons, each with energy that is half of that of the incoming photon discussed in the previous case, and with the assistance of an intermediate "virtual" state. Again, the transition from electronic ground state to excited state involves molecular absorption, resulting in the emission of a lower energy fluorescence photon. It is this absorption of energy by the system that destroys the coherence between the emitted fluorescence photon and the original excitation photons. For many incoming photons, this process could lead to potential photodamage of the fluorophore. SHG operates by a different mechanism. As shown in Fig. 12c, at first glance the SHG process looks similar to the two-photon fluorescence case. However, here only virtual transitions are employed. Two lower-energy photons are annihilated while a single higher energy photon (with twice the wavelength) is simultaneously created in a single quantum-mechanical event. Thus, no molecular absorption takes place, rather only scattering. As a result, photodamage is greatly

reduced, and coherence is maintained between the incoming photons and the emitted SHG photon.

Nonlinear microscopy typically utilizes one of these multiphoton processes; for example, those based on $m$-photon excitation/absorption or harmonic generation, where $m$ represents the number of photons that participate in the specific quantum-mechanical process. The primary advantage is that the signal generated from an $m^{th}$-order nonlinear process depends on $I^m$, where $I$ is the incident intensity. The requirement for high intensity for a nonlinear process means that when the incident beam is strongly focused (e.g., by a high-numerical-aperture microscope objective lens) onto the sample, the nonlinear effects are primarily restricted to the focal region. This results in lower phototoxicity. Furthermore, due to excitation typically at near-infrared wavelengths, the resulting penetration depth is compared to linear fluorescence microscopy techniques. In fact, penetration depths as large as 1.5 mm have been obtained [61]. The next few sections present an abbreviated derivation of SHG beginning with Maxwell's equations, and discuss the effect that energy and momentum conservation has on this process.

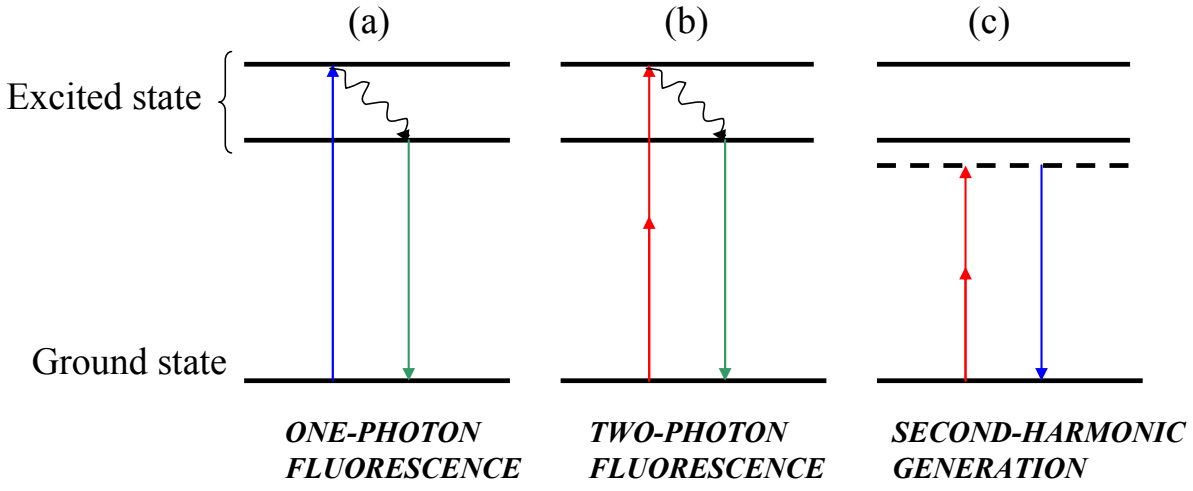


**Figure 12. Jablonski diagram of linear and nonlinear processes showing a) one-photon fluorescence, b) two-photon fluorescence, and c) second-harmonic generation.**

### 2.2.3 Theory of second-harmonic generation (Electromagnetics picture)

To understand the origin of SHG using (classical) electromagnetic optics, we consider Maxwell's equations for a source-free medium as given by [62, 63]

$$\nabla \times E = -\frac{\partial B}{\partial t} \tag{1}$$

$$\nabla \times H = \frac{\partial D}{\partial t} \tag{2}$$

$$\nabla \bullet D = 0 \tag{3}$$

$$\nabla \bullet B = 0, \tag{4}$$

where $E$ is the electric field, $H$ is the magnetic field, $D$ is the electric flux density, and $B$ is the magnetic flux density, respectively. Note that all of these fields are functions of position and time, and the SI units will be used throughout this chapter.

The constitutive relations that define the material properties are

$$D = \varepsilon E = \varepsilon_0 E + P \tag{5}$$

$$B = \mu_0 H, \tag{6}$$

where $\varepsilon_0$ is the free space (electric) permittivity, $\mu_0$ is the free space (magnetic) permeability, and $P$ is the polarization density, i.e., sum of the induced dipole moments, respectively. In linear optics, the polarization density $P$ is directly proportional to the electric field $E$, and is given by

$$P = \varepsilon_0 \chi^{(1)} E, \tag{7}$$

where $\chi^{(1)}$ is the linear susceptibility of the material. It is related to the relative permittivity $\varepsilon_r$ through the following equation

$$\chi^{(1)} = \varepsilon_r - 1. \tag{8}$$

In nonlinear optics, $P$ can be expressed as a power series in $E$ such that

$$P = \varepsilon_0 [\chi^{(1)} E + \chi^{(2)} E^2 + \chi^{(3)} E^3 + ...], \tag{9}$$

where $\chi^{(2)}$ and $\chi^{(3)}$ represent the second- and third-order susceptibilities. The first term varies linearly with the electric field and describes common processes that occur in nature, such as the linear absorption, reflection, and scattering of light. The second term varies quadratically with the electric field and describes second-order nonlinear processes such as SHG, sum and difference frequency generation. Finally, the third term describes third-order processes such as stimulated Raman scattering and third harmonic generation.

For simplicity, equation (9) can be written as

$$P = P^{(1)} + P^{(2)} + P^{(3)} + P^{(4)} + ..., \tag{10}$$

or

$$P = P^{(1)} + P^{(NL)}, \tag{11}$$

where $P^{(NL)} = P^{(2)} + P^{(3)} + P^{(4)} + ...$ .

*2.2.3.1 Nonlinear wave equation*

Here, we derive the wave equation for propagation of light in a nonlinear medium. We begin by taking the curl on both sides of equation (1) to obtain

$$\nabla \times \nabla \times E = -\nabla \times \frac{\partial B}{\partial t}. \tag{12}$$

This can be re-written as

$$\nabla(\nabla \bullet E) - \nabla^2 E = -\mu_0 \frac{\partial \nabla \times H}{\partial t}. \tag{13}$$

Using equations (3) and (5),

$$\nabla \bullet \varepsilon E = 0 \Rightarrow \nabla \bullet E = 0. \tag{14}$$

Substituting equations (2) and (14) into (13), we get

$$-\nabla^2 E = -\mu_0 \varepsilon_0 \frac{\partial^2 E}{\partial t^2} - \mu_0 \frac{\partial^2 P^{(1)}}{\partial t^2} - \mu_0 \frac{\partial^2 P^{(NL)}}{\partial t^2}. \tag{15}$$

Next, we note that the velocity of light in vacuum $c$ is

$$c = \frac{1}{\sqrt{\mu_0 \varepsilon_0}}, \tag{16}$$

and the relative permittivity

$$\varepsilon_r = n^2, \tag{17}$$

where $n$ is the refractive index of the material.

Using equations (7), (8) and (17), equation (15) becomes

$$\nabla^2 E - \frac{n^2}{c^2}\frac{\partial^2 E}{\partial t^2} = \mu_0 \frac{\partial^2 P^{(NL)}}{\partial t^2} \tag{18}$$

This is the wave equation used to describe the nonlinear processes.

*2.2.3.2 Second-order nonlinear polarization*

Let us take a closer look at the second-order nonlinearity. We can express $E$ in terms of its complex amplitude $\widetilde{E}$ such that $E(t) = \widetilde{E}e^{i\omega t} + \widetilde{E}^* e^{-i\omega t}$. For a second order nonlinearity,

$$P^{(2)} = \varepsilon_0 \chi^{(2)} E^2 = \varepsilon_0 \chi^{(2)} \left[\widetilde{E}e^{i\omega t} + \widetilde{E}^* e^{-i\omega t}\right]^2 = \varepsilon_0 \left[\chi^{(2)} \widetilde{E}^2 e^{i2\omega t} + \chi^{(2)} \widetilde{E}^{*2} e^{-i2\omega t} + 2\chi^{(2)} \left|\widetilde{E}\right|^2\right].$$

The last term leads to generation of a static DC field in the nonlinear medium, while the first and second terms create polarization densities at +2ω, and -2ω, leading to the generation of SHG. Thus, $\widetilde{P}^{(2)}(2\omega) = \varepsilon_0 \chi^{(2)} \widetilde{E}^2$ or

$$\widetilde{P}^{(2)}(2\omega) = 2d_{eff} \widetilde{E}^2, \tag{19}$$

where $d_{eff}$ is the effective value of the second-order susceptibility.

*2.2.3.3 Determination of second-harmonic generation intensity*

To determine an expression for the SHG intensity, we recognize that the complex amplitude of the incident field can be written as

$$\widetilde{E} = A_1 e^{-ik_1 z}. \tag{20}$$

Substituting it into equation (19), we get

$$\widetilde{P}^{(2)}(\omega_3) = 2d_{eff} A_1^{\,2} e^{-i2k_1 z} . \tag{21}$$

Let us write the generated electric field for SHG as

$$E = E_3 = A_3 e^{-i(k_3 z - \omega_3 t)} + A_3^{\,*} e^{i(k_3 z - \omega_3 t)}, \tag{22}$$

and express the nonlinear polarization to be in the form

$$P_{NL} = \widetilde{P} e^{i\omega_3 t} + \widetilde{P}^{*} e^{-i\omega_3 t} . \tag{23}$$

For SHG,

$$P_{NL} = \widetilde{P}^{(2)}(\omega_3) e^{i\omega_3 t} + \widetilde{P}^{(2)^{*}}(\omega_3) e^{-i\omega_3 t}, \tag{24}$$

where $\omega_3 = 2\omega$. Substituting equations (21), (22), and (24) into the nonlinear wave equation, neglecting the complex conjugate part, and after simplifying, (8) becomes

$$\left( \frac{\partial^2 A_3}{\partial z^2} + 2ik_3 \frac{\partial A_3}{\partial z} - A_3 k_3^{\,2} + A_3 \frac{n_3^{\,2} \omega_3^{\,2}}{c^2} \right) e^{-i(k_3 z - \omega_3 t)} = -2d_{eff} A_1^{\,2} e^{-i2k_1 z} e^{i\omega_3 t} \omega_3^{\,2} .$$

The third and fourth terms cancel since

$$k_3 = \frac{n_3 \omega_3}{c} . \tag{25}$$

Assuming that the spectrum of the source is narrow-band, the slowly varying amplitude approximation can be applied, i.e.,

$$\frac{\partial^2 A_3}{\partial z^2} << \frac{\partial A_3}{\partial z} . \tag{26}$$

This leads to

$$\frac{\partial A_3}{\partial z} = \frac{-d_{eff} A_1^{\,2} \omega_3^{\,2}}{2ik_3} e^{-i(2k_1 - k_3)z}. \tag{27}$$

Integrating over the length $L$ of the nonlinear medium

$$A_3 = \frac{-d_{eff} A_1^{\,2} \omega_3^{\,2}}{2ik_3} \int_0^L e^{-i(2k_1 - k_3)z} dz. \tag{28}$$

Solving, we get

$$A_3 = \frac{d_{eff} A_1^{\,2} \omega_3^{\,2} L}{2ik_3} e^{-\frac{i\Delta kL}{2}} \sin c\left(\frac{\Delta kL}{2}\right), \tag{29}$$

where $\Delta k = 2k_1 - k_2$ is called the phase mismatch factor.

The intensity is given by

$$I = \frac{|A_3|^2}{2\eta}, \tag{30}$$

where $\eta$ is the material optical impedance, given by

$$\eta = \sqrt{\frac{\mu_r \mu_0}{\varepsilon_r \varepsilon_0}}. \tag{31}$$

For a nonmagnetic material, $\mu_r$=1, and using equation (17), it follows that

$$\eta \propto \frac{1}{n}. \tag{32}$$

Using equations (31) and (32), (30) becomes

$$I = \frac{d^2{}_{eff} c^2 I_1{}^2 \omega_3{}^2 L^2}{2 n_1{}^2 n_3} Sinc^2\left(\frac{\Delta kL}{2}\right), \tag{33}$$

or,

$$I \propto Sinc^2\left(\frac{\Delta kL}{2}\right). \tag{34}$$

Figure 13 is a plot of the normalized SHG intensity vs. phase mismatch factor $\Delta k$.

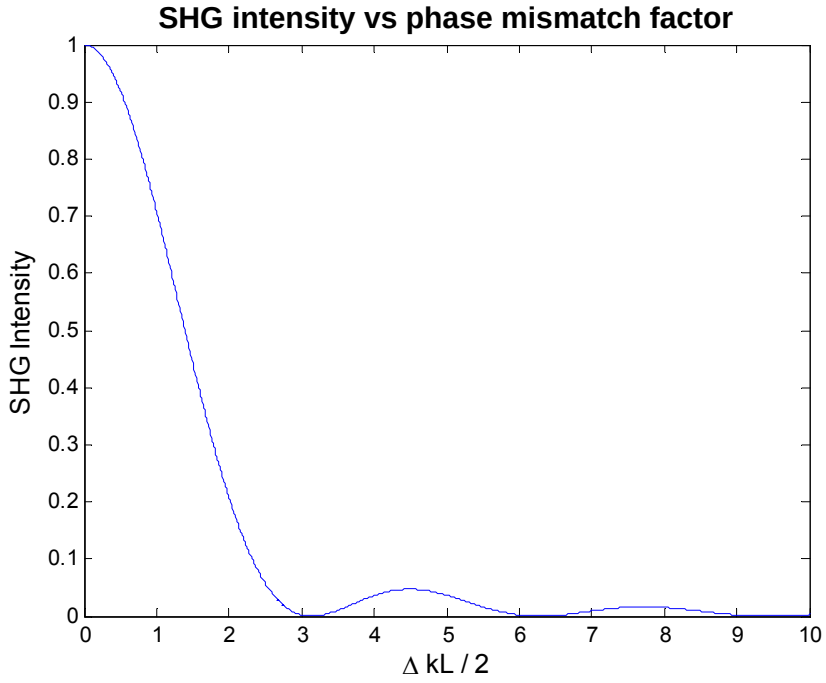


**Figure 13. SHG intensity vs. phase mismatch factor.**

As we can see, the SHG intensity peaks at $\frac{\Delta kL}{2} = 0$, i.e., $\Delta k = 2k_1 - k_3 = 0$. Using equation (25), we have $\frac{2\omega_1 n_1}{c} - \frac{\omega_3 n_3}{c} = 0$. We note that $\omega_3 = 2\omega_1$, and thus

$$n_3 = n_1. \tag{35}$$

Since many materials are naturally dispersive (i.e., refractive index changes with wavelength), this condition is difficult to achieve for isotropic samples. Hence, a common practice is to use birefringence in anisotropic materials. Here the polarization of the incident wave and angle of the anisotropic crystal is chosen such that $n_3 = n_1$. This condition of $\Delta k = 0$ is called *perfect phase matching*.

### 2.2.4 Non-perfect phase matching

Now let us consider the case where a material is not adjusted for perfect phase matching, the so-called *non-perfect phase matching*, i.e., $\Delta k \neq 0$. As discussed before, the SHG intensity has a sinc$^2$ dependence on the phase mismatch factor $\Delta k$. We observe that SHG is generated until the argument of the sinc function $\frac{\Delta kL}{2} = \pi$. This defines the coherence length of SHG generation, and $L_c$ is given by

$$L_c = \frac{2\pi}{|\Delta k|} = \frac{\lambda}{2|n_1 - n_3|}. \tag{36}$$

It is preferred that the value of $\Delta k$ be small so that the coherence length is large. Larger coherence lengths allow longer interactions lengths L, which in turn allow higher SHG intensities according to the equation (33). However, in practice, natural materials may be arranged in such a way that $\Delta k$ may not be small. On such example is the biological tissues where SHG intensities have been observed from as small as few hundred nanometers. The SHG intensities generated are much less than that of materials for which $\Delta k = 0$ or $\Delta k$ is comparatively smaller, because of the smaller coherence lengths (therefore smaller interaction lengths). According to equation (33), the SHG intensity is also sensitive to the sample property $d_{eff}$. Crystalline samples such as collagen type I have large values of $d_{eff}$ and thus produce stronger SHG signal compared to collagen type III which is less crystalline.

### 2.2.5 Non-centrosymmetry

Yet another condition for the generation of SHG is non-centrosymmetry, which describes materials having no inversion symmetry. Inorganic materials such as beta barium borate (BBO), lithium niobate ($LiNbO_3$) and potassium dihydrogen phosphate (KDP) possess this trait, but even biological structures such as collagen, microtubulin, and myosin display non-centrosymmetry. The requirement for non-centrosymmetry can be understood by considering equation (9) [62],

$$\widetilde{P}^{(2)}(2\omega) = \chi^{(2)}\widetilde{E}^2, \tag{37}$$

and comparing to the expression for the induced polarization in a centrosymmetric medium (when the applied electric field is phase shifted by 180°) given by

$$-\widetilde{P}^{(2)}(2\omega) = \chi^{(2)}(-\widetilde{E})^2 = \chi^{(2)}\widetilde{E}^2. \tag{38}$$

Comparing the two equations, one sees that they can only be equal when $\chi^{(2)} = 0$. Hence the medium needs to be non-centrosymmetric in order to produce SHG. It can also be understood qualitatively in terms of the dipole emission, which is discussed in section 2.

### 2.2.6 Quasi-phase matching

Under non-perfect phase matching condition, $\Delta k \neq 0$. As we know, this limits the SHG intensity that can be generated. However, there is a way of increasing the SHG intensity by fabricating the material such that its second-order susceptibility is spatially modulated, according to the equation

$$d(z) = d\exp(-iQz). \tag{39}$$

The phase matching condition in this case becomes

$$\Delta k = 2k_1 - k_3 - Q, \tag{40}$$

and perfect phase matching is obtained when $Q = \Delta k$. However, it is difficult to fabricate a structure that has periodic variations in its second-order coefficient *d*. This type of periodic fabrication is called *poling*. With quasi-phase matching (QPM), the sign of *d* is alternated by a period equal to the coherence length. This occurs naturally in some biological structures, as will be discussed in section 2.2.11.

### 2.2.7 Phase-matching bandwidth

So far, we have assumed that the incident beam is strictly monochromatic. However, for polychromatic light, dispersion in a nonlinear medium affects phase matching. Consider the case of second-harmonic generation from a nonlinear medium which exhibits first-order dispersion (and negligible higher-order dispersion). Here, fundamental and second harmonic waves become separated upon propagation in the medium due to the differences in their respective group velocities, $\nu_1$ and $\nu_3$. This walk-off effect, as it is known, limits the generation of SHG to a walk-off length $L_g = \tau/2|1/\nu_3 - 1/\nu_1|$, where $\tau$ is the pulse-width of the laser [63]. Hence, when using broadband sources, group velocity is an important parameter and phase matching requires that the group indices $N_1$ and $N_3$, at the fundamental and second-harmonic frequencies, respectively, are matched.

The phase-matching bandwidth is given by [63]

$$\Delta\nu = \frac{c_o}{2L|N_1 - N_3|}. \tag{41}$$

The group velocity phase matching can be achieved either by using a thin crystal so that there is little walk-off or designing the crystal such that $N_1 \sim N_3$. In many situations, $L_c$ is smaller than $L_g$, and hence the phase velocity mismatch usually dominates.

### 2.2.8 Theory on the second-harmonic generation (Dipole picture)

As discussed before, second-harmonic generation (SHG) is a second-order nonlinear process wherein a non-centrosymmetric material (frequency) up-converts the incident light of frequency $\omega$ to light of frequency of $2\omega$.

Here we briefly discuss the mechanism of generation for SHG from a molecular dipole picture. A detailed explanation can be found in [22]. When light of frequency $\omega$ is incident on a centrosymmetric molecule, the associated electron cloud begins to symmetrically oscillate at that frequency. In turn, a wave is emitted at the same frequency in a dipole-like emission pattern, commonly referred to as Rayleigh scattering as shown in the Figure 14a. However, when light of the same frequency is incident on a non-centrosymmetric molecule the oscillation becomes asymmetric, resulting in the generation of additional frequency components at 0 (DC) and $2\omega$ (see Fig. 14b). This wave at $2\omega$ is referred to as the hyper-Rayleigh scattered (HRS).

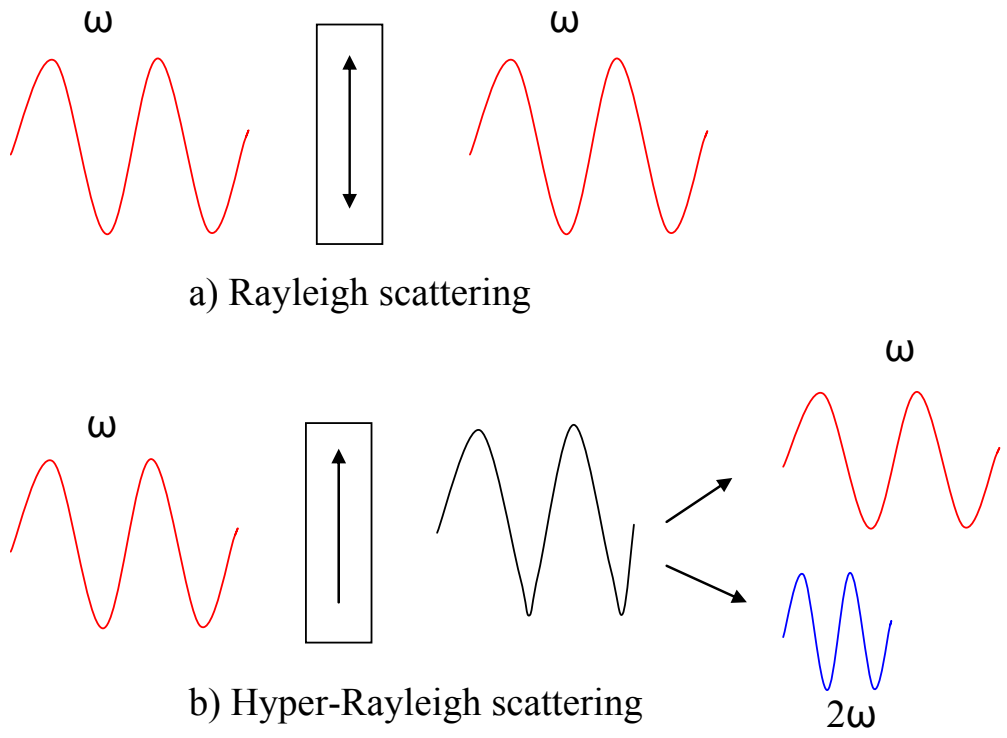


**Figure 14. Scattering phenomenon of a) centrosymmetric and b) non-centrosymmetric molecules.**

For a single non-centrosymmetric molecule, the HRS emission is dipole-like as shown in the Fig. 15a. However, when there is regular arrangement of such molecules (scatterers) in a material, then there is constructive interference between the generated waves occur, leading to a significant amount of signal generated predominantly in the forward direction (Fig. 15b). This signal is referred to as SHG. Thus, we can think of SHG as a macroscopic equivalent of HRS with ordered arrangement of scatterers. This is an important principle to keep in mind since it explains why not all non-centrosymmetric structures (proteins such as DNA) emit SHG. DNA may emit HRS; however it is not ordered at the scale of the wavelength of light, and thus does not produce measurable SHG. On the other hand, structures such as collagen and myosin have regularly arranged molecules that coherently build up the HRS to produce SHG.

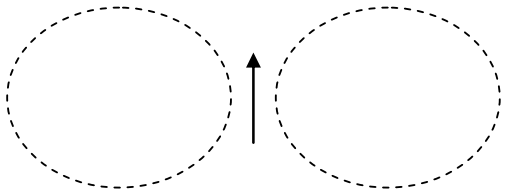

a) Dipole-like HRS emission from a single molecule

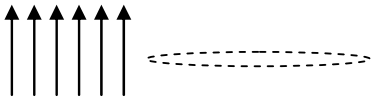

b) Directional forward SHG emission from multiple HRS scatterers

**Figure 15. a) HRS emission from a single non-centrosymmetric molecule. b) SHG emission from multiple HRS scatterers.**

*2.2.8.1 Directionality*

It is also important to note that the emitted dipole pattern for SHG is extremely directional, i.e., SHG is emitted predominantly in the forward direction. This is due to the momentum conservation that follows directly from the phase matching condition, $\Delta k = 2k_1 - k_3 = 0$ , as shown pictorially in the Fig. 16. However, there are (two) scenarios when SHG can be directed in the backward direction. This is discussed in the next section.

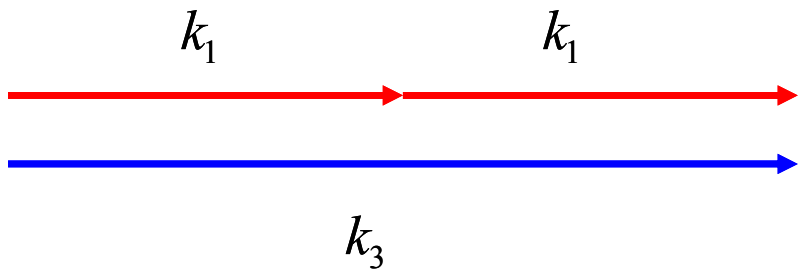


**Figure 16. Predominant forward propagation of SHG due to phase matching**

### 2.2.9 Backward second-harmonic generation

Backward SHG can be generated when the axial scatterers are spaced by $\lambda_{SHG}/2$. This leads to constructive interference in the backward direction as shown in the Fig. 17a. Here, the emission is directional in both the forward and backward directions, as indicated by the small emission cone. Moreover, the emission is coherent since phase is preserved through interference. Backward SHG may also be generated through multiple scattering of the forward-generated SHG in the backward direction as shown in Fig. 17b. In this case, due to the potentially multiple scattering events, phase information is lost and emission is no longer directions. This is frequently observed in the turbid media.

### 2.2.10 Effect of focusing

As we have just discussed, SHG emission is typically in the forward direction along the optical (propagation) axis. However, usually in microscopy high NA objective lenses are

employed to create high-spatial-resolution SHG images. For a focused Gaussian beam, there is an inherent Gouy phase shift when compared to a collimated beam. This results in a retardation in phase of the incident beam, which requires the SHG to propagate off-axis due to momentum conservation. Hence, this must be taken into account in practice if one is interested in efficient SHG collection. Details on this are provided in Ref. [22].

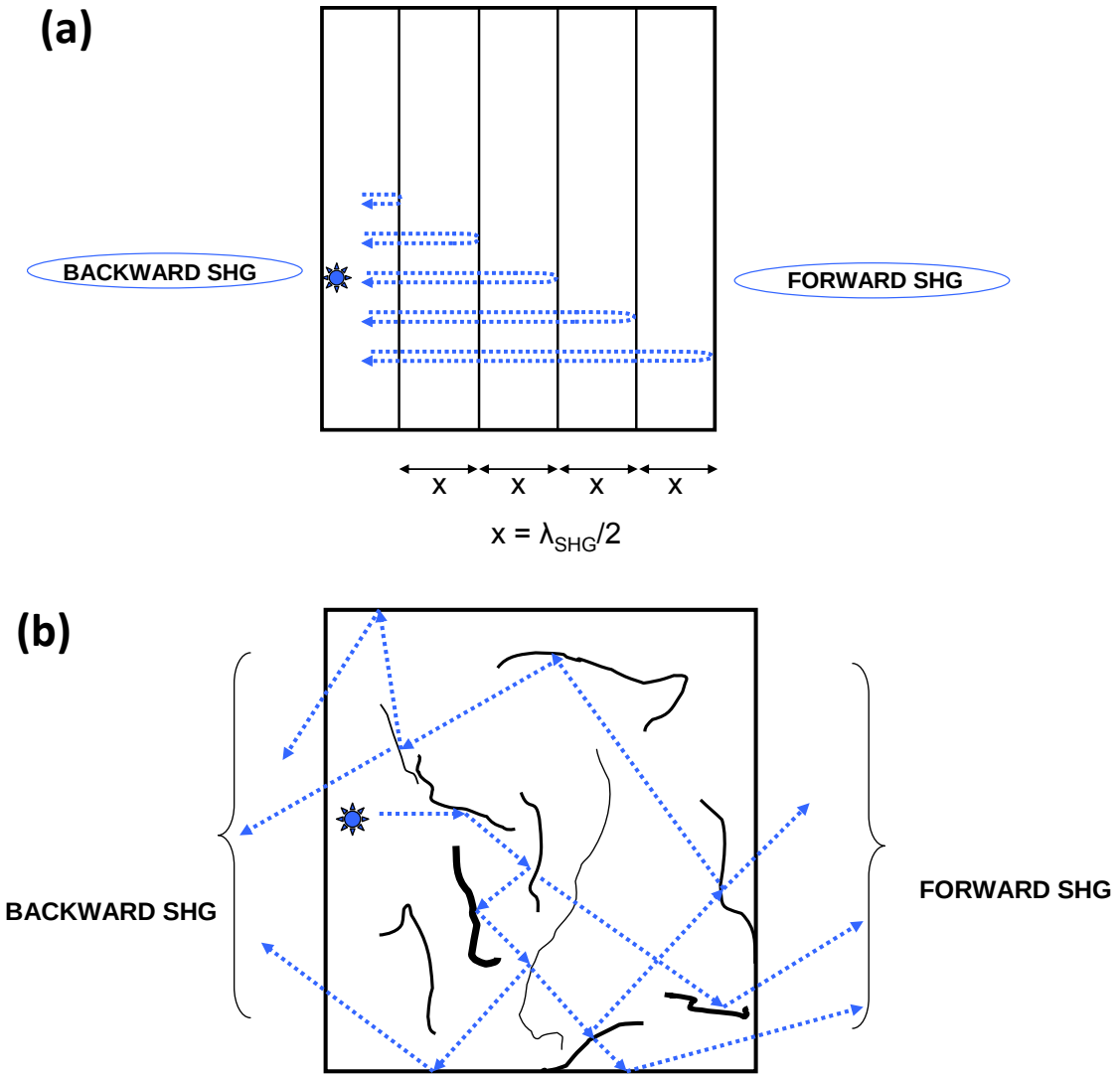


**Figure 17. a) Coherent backward SHG generation through constructive interference of scatterers spaced $\lambda_{SHG}/2$. Both emissions are directional. b) Incoherent backward SHG generation from multiple scattering of forward SHG. Both emissions are no longer directional.**

### 2.2.11 Phase matching in biological tissues

As discussed before, for perfect phase matching $\Delta k = 0$. For nonlinear crystals, this is achieved by adjusting the angle of the optical axis of the crystal relative to the incident wave polarization and propagation direction. However, in non-centrosymmetric biological tissues, such as collagen fibers, we have the case of non-perfect phase matching. Thus, the thickness of a fiber should be on the order of the coherence length of SHG. This ensures that there are a sufficient number of dipoles participating in the generation of SHG to provide a measurable signal. Therefore, two conditions are absolutely necessary for efficient generation of SHG. The material should possess a sufficient density of non-centrosymmetric structures, and it should be ordered at the molecular level to generate an efficient SHG signal. Moreover, the generation of SHG in biological tissues is somewhat "relaxed". This is because the arrangement of collagen fibers along the axial direction is similar to that of quasi-phase matching—not exactly quasi-phase matching, since the collagen fibers are not poled [64].

### 2.2.12 Experimental configuration

The schematic of the experimental setup for the SHG microscope is shown in Fig. 18. It is basically a two-photon fluorescence microscope that is modified to include both the transmission and reflection collection geometries. The beam is obtained from a wavelength-tunable (690 to 1020 nm) Ti:Sapphire laser that produces 100 femtosecond-duration, linearly polarized, pulses at 80 MHz repetition rate. The Ti:Sapphire laser is well-suited for nonlinear microscopy techniques. A high repetition rate of 80 MHz ensures that there are enough pulses incident on the sample for high speed scanning. Pulsewidths significantly greater than 100 fs could lead to multiphoton ionization. The choice of wavelength depends on the biological tissue under investigation. Next, the beam is spatially filtered and collimated before sending it to the galvanometer-driven *x*-*y* scanner, which generates raster-scan pattern. The beam is then reflected by a short-pass 680-nm dichroic beam splitter. After passing through a combination of relay lenses (scan and tube lens), it is focused onto the sample using a high-numerical-aperture (high-NA) oil-immersion illumination objective. For thick biological tissues, a water-

immersion objective is preferable to avoid aberrations due to refractive-index mismatch. The transmitted signal from the sample is collected by a second objective. For efficient SHG collection, it is better that the collection objective has an NA equal to or greater than the illumination objective. This is a direct consequence of the Gouy phase discussed earlier. The SHG signal is collected through spectral filtering using a laser blocking filter followed by a bandpass filter that transmits only the SHG signal. The SHG intensity is recorded with a photo-multiplier, and image stacks are acquired from various depths ($z$) into the sample. The power settings should be optimized for image contrast, and avoiding unwanted multiphoton effects such as optical breakdown.

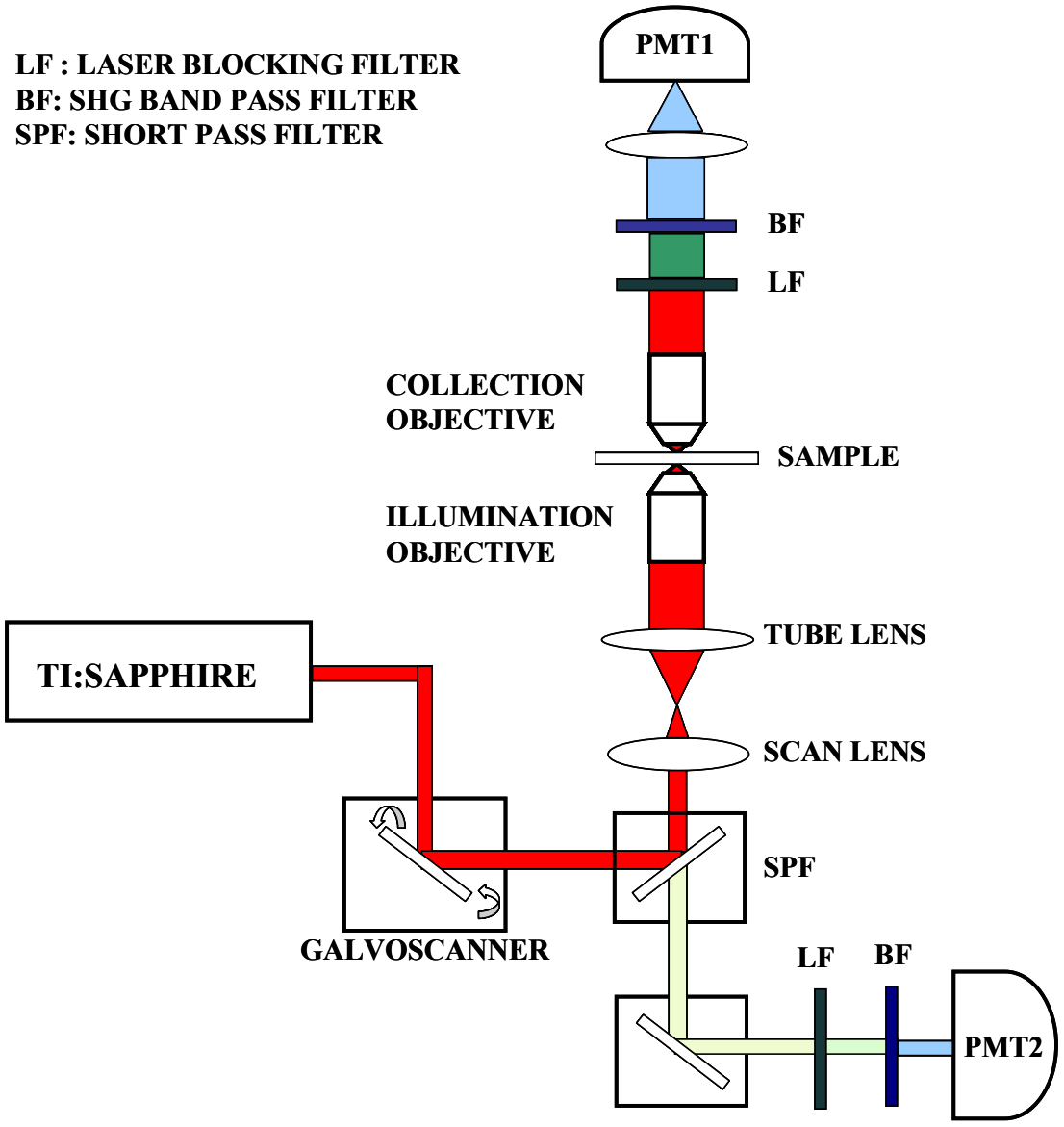


**Figure 18. Experimental setup of the SHG microscope.**

### 2.2.13 Practical considerations

*2.2.13.1 Distinguishing SHG*

There are several ways of distinguishing SHG from other signals. A simple way is to look at its spectrum. The spectral width of SHG is ~ 70% of the illumination bandwidth which is significantly narrower compared to fluorescence. Moreover, SHG is polarized. A simple polar

plot obtained from rotation of a polarizer either before or after the sample provides information on the degree of polarization of the emitted signal.

*2.2.13.2 Resolution and penetration depth*

The resolution of SHG is similar to that of TPF. The transverse resolution is given by [65]

$$w_t = \frac{0.7\lambda_{em}}{NA}. \quad (42)$$

While the axial resolution is

$$w_z = \frac{2.3\lambda_{em} n}{NA^2}, \quad (43)$$

where $n$ is the refractive index of the immersion fluid, and $\lambda_{em}$ is the emission wavelength.

For example, an objective of NA=1.4 and $\lambda_{em}$ = 400 nm (for excitation at 800 nm) gives a transverse spot size of 200 nm and axial resolution of 700 nm.

The penetration depth depends on the tissue under observation. However, as discussed previously, SHG (and two-photon) microscopy employ photons in the near-IR, where biological tissue absorption is low. This translates to a deeper penetration depth compared to linear microscopy techniques. Moreover, only a small region at the focus is excited, thus allowing for optical histology to be performed. Depths as large as 500 μm for sclera in the eye, and 400 μm in brain tissue, have been imaged using SHG microscopy [21, 66].

*2.2.13.3 Power limitations*

Once the SHG is generated at the focus, there is an unavoidable absorption of the SHG photons due to Rayleigh scattering. Moreover, there can be photo-thermal effects at high intensities, e.g., the generation of singlet oxygen which is highly reactive and damages the

tissue. Under extremely high intensities, there can be multiphoton ionization of the tissue. Hence, it is best to keep the power as low as possible as long as there is enough SHG signal to create good image contrast. Some tissues such as tendon have been shown to withstand powers as high as 40-50 mW without visible damage [67].

### 2.2.14 Advantages and disadvantages of SHG

The relative advantages and disadvantages of SHG microscopy, compared to other microscopy techniques, are summarized in Table 2.

**Table 2. Advantages and disadvantages of SHG microscopy**

| Advantages | Disadvantages |
|---|---|
| No staining | Expensive hardware requirements |
| Deeper penetration | Signal strength could be weak for some |
| Low phototoxicity | Sensitive to specific biological structures |
| Intrinsic sectioning capability (3D images) | |
| Highly sensitive to structural information | |
| Phase carries “extra” information | |

# CHAPTER 3: FOURIER TRANSFORM-SECOND-HARMONIC GENERATION IMAGING

In this chapter, we will discuss in detail the first technique, Fourier transform-second-harmonic generation imaging (FT-SHG imaging) for quantifying collagen fiber organization in biological tissues. Specifically, FT-SHG imaging involves extracting quantitative metrics through the application of spatial Fourier analysis on the images of collagen-based tissues obtained from an SHG microscope. We define simple metrics, preferred orientation, maximum spatial frequency, and fiber spacing and show how it could be used for quantification. In particular, we quantify differences in collagen fiber organization among several porcine tissues: ear cartilage, trachea, and cornea. We also investigate structural changes through a 3D stack of cornea.

Ultimately, the clinical application of SHG microscopy requires the use of backward geometry. However, SHG is emitted predominantly in the forward direction; and unlike fluorescence, the forward and backward emitted signals may not necessarily contain the same information. Hence, we also quantify the differences in the information content between SHG images obtained from the forward and backward direction for three tissue types: porcine tendon, sclera, and ear cartilage using Fourier transform-second-harmonic generation (FT-SHG) microscopy. In particular, two metrics are used: preferred orientation and peaks in the magnitude spectrum of the Fourier transform.

We then show that FT-SHG imaging can be used as a valuable diagnostic tool for real-world biological problems where the structure of collagen fibers changes due to damage from disease or physical injury. In particular, we investigate the potential of FT-SHG imaging in evaluating collagenase-induced injury in horse tendons. The differences in collagen fiber organization between normal and injured tendon are quantified. FT-SHG microscopy is also compared with the conventional polarized light microscopy for assessing injured tendons.

Later, we propose the use of FT-SHG imaging for quantifying collagen fibers in porcine femoral cortical bone. The technique is compared with scanning electron microscopy (SEM); and the pros and cons of each are discussed. Furthermore, we provide an exploratory study

where we quantitatively assess collagen fiber organization of bone structure as a function of age, from very young to mature bone.

We also investigate differences in collagen fiber organization between cornea and sclera of the eye. In particular, we investigate their properties of transparency and opacity for cornea and sclera, respectively. The lamellar ordered structure of cornea is also investigated.

We also utilized FT-SHG imaging to investigate differences in stromal collagen fibers for human breast tissues from different pathologic conditions, namely normal, hyperplasia, dysplasia, and malignant. Specifically, we apply a parameter that computes the regularity in collagen fiber orientation (A. I. ratio) and use it to compare across the tissue conditions. Finally the extension of FT-SHG to 3d is proposed. Some initial work and future directions are provided.

### 3.1 Brief Introduction and Background

As mentioned in the introduction (Chapter 1), recently, researchers have made major strides in developing quantitative metrics for SHG imaging [25, 28, 29, 32, 33]. Its advantages include non-biased, more accurate, and faster analysis of the tissue of interest. It also leads to extraction of sensitive changes in collagen fiber organization, and, thus, may help in early diagnosis. We briefly discuss a few recent approaches to quantitative SHG imaging. One approach uses forward-to-backward (F/B) ratio of the emitted SHG signal to reveal additional information about the environment of collagen fibers [29]. It was found that solutions (NaCl) of high ionic strength reduced the F/B ratio for adult tendons, and was attributed to sub-diffraction structural changes in collagen fibers. In another study, the F/B ratio was used to differentiate between types of collagen [20]. Type I collagen, which is highly crystalline, produces strong a F/B SHG signal, while Type III and IV collagens, which are less crystalline, produce a weaker signal. Yet another metric is the relative components of the second-order nonlinear susceptibility tensor [25]. These tensor elements are extracted from the SHG images in order to determine the orientation angle of myosin and collagen harmonophores in gastrocnemius muscle and tendon. Recently, these elements were used to differentiate between different SHG generators within the human dermis and the collagen-

muscle junction of a chicken wing [25]. Another measure is the distribution of length of structures in a tissue [32]. In particular the SHG signals emitted from the myosin filaments of sarcomeres were quantified by length distribution to investigate mice and human skeletal muscle tissue. It was thus possible to examine the disease stage, recovery, and aging of the muscle tissues. In addition to these approaches, Fourier analysis could be used to derive quantitative markers for assessment of biological structures [33]. Very recently, along with other parameters, the geometric distribution of spatial frequencies in the 2D Fourier transform (FT) was used to quantify the disorganization of collagen fibers due to photo-thermal damage in porcine corneas. It was found that regularity in fiber organization leads to an elliptical FT distribution whereas randomness leads to a more circular distribution. Aside from this work, to our knowledge, Fourier analysis has yet to be fully utilized in SHG imaging as a means of deriving quantitative measures for biological structures. In this chapter, we propose the use of Fourier transform-SHG (FT-SHG) microscopy to obtain information on collagen fiber orientation and maximum spatial frequency in an image. Such a tool could aid in identifying parameters that represent the organization of collagen fibers, which could lead to the development of quantitative biomarkers help discriminate between healthy and damaged tissues.

### 3.2 Method

The Fourier transform (FT) is a valuable mathematical tool that has been used in a variety of fields to analyze the frequency content of acquired signals and is typically carried out in 1D [68]. The technique can be applied to images through the use of the 2D FT, whereby image contents are decomposed into a superposition of harmonic functions (of varying amplitudes and phases) along horizontal and vertical axes [69-71]. The associated spatial frequencies are simply the modulations in intensity in the image per unit distance [63, 72]. Lower frequencies are closer to the origin (point at which spatial frequency is zero), while higher frequencies are further away.

### 3.2.1 Quantitative metrics

The first parameter that we extract from the Fourier space is "preferred" orientation, which refers to the average direction in which fibers are oriented in a given plane. Improved accuracy in Fourier space is often used to determine the orientation of an image in real space [73]. When structures in an image have a preferred orientation, the high amplitudes on average align along a direction perpendicular to the preferred orientation in the 2D FT. Although there are other methods to obtain the orientation of structures, we employ simple methods that do not invoke the use of complex algorithms or polarization modulation techniques [74-76]. Four simple methods of calculating preferred orientation and their pros and cons are discussed below.

The first method, called the "line-fit method," used for calculating preferred orientation is shown pictorially in Fig. 19. Let us consider the image of ear cartilage shown in Fig. 19a for which the preferred orientation needs to be calculated. First, a 2D Fourier transform (FT) of the region of interest is obtained using the fast Fourier transform in Matlab as shown in Fig. 19b. Then, a binary image is created by isolating dominant spatial frequencies (higher amplitudes) using a desired amplitude threshold. The isolated frequencies are assigned an amplitude of 1, and all other frequencies are given an amplitude of zero (see Fig. 19c). Finally, a best-fit line is applied to this binary image as shown in Fig, 19d, which is along a direction that is perpendicular to the preferred orientation, i.e., the orientation of the best-fit line minus 90° gives the preferred orientation of fibers in the image. The standard error in fitting a line gives one a measure of the randomness in fiber orientation within the image which we call "spread". This is also a useful metric to quantify fiber organization. The advantages of the technique are that it is intuitive and fairly fast (< 5 seconds). However, it suffers from inaccuracies especially when fiber orientation is close to 0° with respect to the horizontal axis. Note that most of the analysis in this thesis is performed using Matlab 2012a on an Intel dual-core processor with 3GB RAM. Note that a single absolute value of preferred orientation itself is not meaningful since it depends on how the tissue is cut and placed on the microscope slide. However, when all the tissues are cut in consistent orientation (through some kind of known biological marker) and placed on the microscope slide the same way, the preferred orientations carry information "relative" to each other. This ensures that the

preferred orientations measured within the sample (intra-sample) and across samples (inter-sample) are meaningful. The spread in orientation, however, is an absolute measure and is thus meaningful since it does not rely on all samples having the same reference calibration of cut.

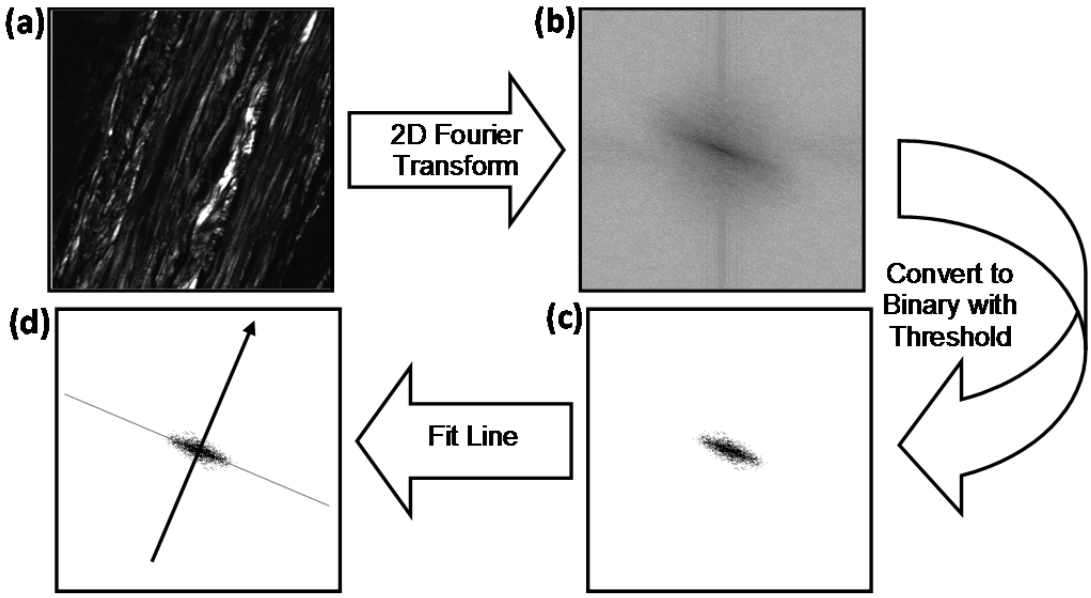


**Figure 19. Line-fit method for calculating preferred orientation. (a) SHG image of ear cartilage, (b) its 2D Fourier transform, (c) conversion to binary image, and (d) best line fit.**

The second method of calculating preferred orientation is called "radial integration" or "polar sum". Figure 20a shows a test image with 3 different orientations. Here again, we first take the 2D Fourier transform of the region of interest (Fig. 20b). However, in this method, instead of making it a binary image, the 2D FT is then integrated radially across different angles which results in a plot of orientation angle as a function of radial amplitude strength (see Fig. 20c). This plot is then fitted with Gaussians; the center of Gaussian fits give the orientation of fibers (multiple fits for several orientations), and the width provides a measure of how randomly the fibers are oriented in the region of interest (see Fig. 20d). The advantage of this method is that not only the preferred orientation but also other dominant orientations present in the image can be calculated. Moreover, the method is robust and accurate (<0.5°). It can also be used on extremely small images as tiny as 16 x 16 pixels. However, the only

disadvantage is that the method is slow since it requires integration at fine angles. It can take up to 30 seconds to calculate preferred orientation for an image of size 1024 x 1024 pixels.

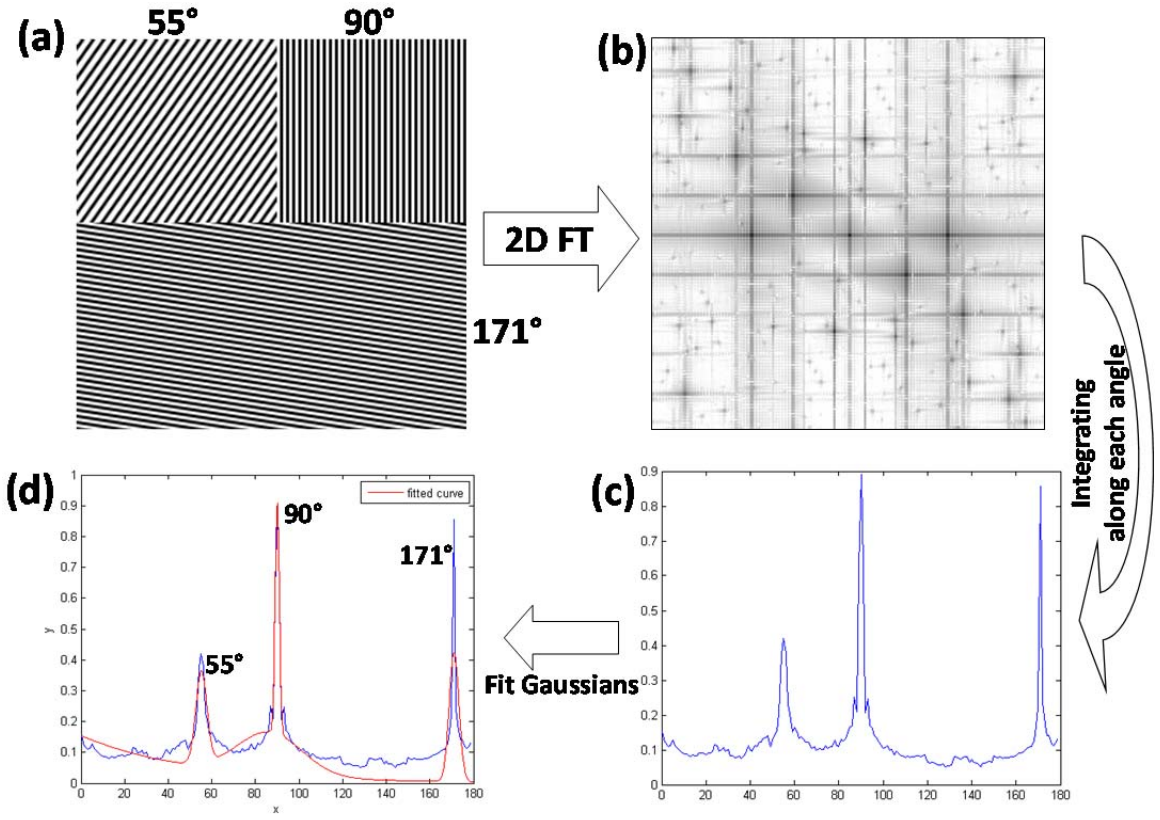


**Figure 20. Radial integration method for calculating preferred orientation. (a) Test image, (b) its 2D Fourier-transform, (c) line plot of strength of spatial frequencies vs. orientation, and (d) Gaussian fits.**

The third method of calculating preferred orientation is called the "gradient method". Here, we use image gradients in order to calculate the orientations present in the image. Consider an image of tendon shown in Fig. 21a. First, the gradients along horizontal axis ($\Delta x$) and vertical axis ($\Delta y$) are calculated. The local orientation of the feature is given by the $\theta = \tan^{-1}(\Delta x / \Delta y)$, which is then expressed in degrees as shown in the Fig. 21b. It is important to note that most of the real images contain noisy (low signal-to-noise ratio) regions, and this induces artifacts in the gradient leading to erroneous orientations, which typically occur at 0°, 45°, 90°, 135° and 180°. These artifacts are removed through a logically indexed search in Matlab. Needless to say, wherever possible, logical indexing and efficient coding is a must in Matlab in order to

make the program computationally efficient leading to fast computations even on a regular desktop computer. Finally, a histogram distribution of orientations is plotted as shown in Fig. 21c. From this distribution, it is possible to extract information on orientation such as preferred orientation and spread.

There are several advantages of this method. It can also calculate other orientations including preferred orientation. However, the major advantage of this method is its speed. It only takes 0.15 seconds to calculate preferred orientation for an image of size 1024 x 1024 pixels. The method is fairly accurate (<1°). It can also work with images as small as 8 x 8 pixels. However, as mentioned, the only disadvantage is that the outlier needs to be removed, especially for noisy images. If there are fibers actually oriented at 45°, we have to rely on the standard deviation in fiber orientation in order to calculate its nearest angle. Thus, for fibers aligned at those angles, the accuracy may be <1°, while at other angles it might be better than 0.5°. However, the method stills reasonably good estimate of orientation.

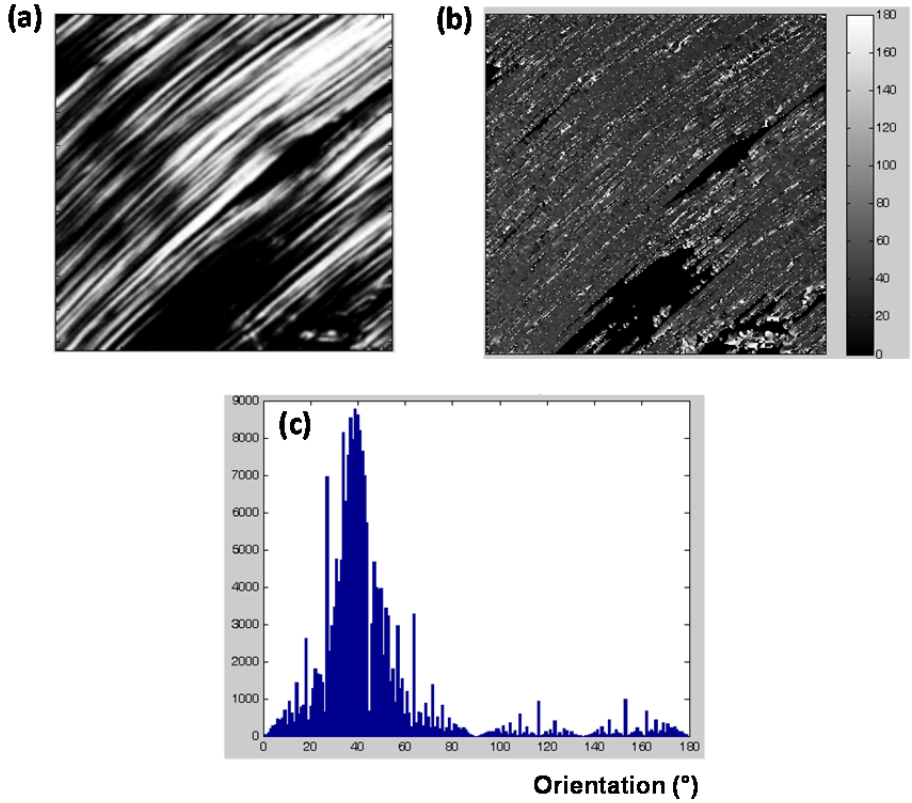


**Figure 21. Image gradient method for calculating preferred orientation. (a) SHG image of tendon, (b) local orientation image, (c) histograms of the orientations present in (b).**

The last method of calculating preferred orientation is called “peak extraction” method. Here, the x, y coordinate of the points with higher amplitudes within the 2D FT are directly extracted using threshold or sorting (first few points selected) as shown in Fig. 22; this figure is basically the same as Fig. 20b. The DC is located in the center and from the x, y coordinates of other dominant spatial frequencies, it is possible to extract the preferred orientation as well as several of other orientations present in the image. The main advantage of this method is that it is fastest among all the mentioned methods, taking only 0.04 seconds to calculate preferred orientation for an image of size 1024 x 1024 pixels. However, there is a glitch to this method. The assumption that there is a distinct peak away from the DC causes concerns in images where there is no clear peak. Images with repetitive structures at a fixed spatial frequency have a peak in the Fourier transform, however, not all images have regular repetitions; for example, a real image of tendon does not produce a peak in the FT. In such cases, the frequencies with high amplitudes lie close to the DC, oftentimes, a pixel away from the DC, and this leads to significant rounding, i.e., a fiber oriented at 35 can be incorrectly estimated as 45. In order to avoid such a problem, we do not consider a circle whose center is DC with a radius of ~ 5 pixels. This significantly reduces the rounding problem; however, it also puts a constraint on the minimum size of the image for which the preferred orientation can be accurately calculated. From experience, the minimum size is ~ 64 x 64 pixels. Therefore, if the image size is ≥ 64 x 64 pixels in size, this method can calculate orientation extremely fast.

Instead of quantifying a particular region of interest within an image or the whole image as we have seen so far, we can divide an image into smaller “sub-images” or with a grid and determine the local fiber orientation within each of these smaller regions. This is particularly useful for understanding the structural correlation between different spatial regions within an image. Additional parameters are obtained by further characterizing a region as dark, anisotropic, or isotropic. A region is considered dark if the SHG intensity from the region is low or negligible. Areas with fibers having a preferential orientation are categorized as anisotropic, while those with fibers aligned along several different orientations (with no preferred orientation) are considered isotropic. To decide whether a region is isotropic or

anisotropic, we look at the angular power spectrum, i.e., the strength of the various orientations that exists in a particular region. For example, a group of fibers all oriented along the same direction would give a single sharp peak in the angular power spectrum corresponding to that direction. This is the "anisotropic" case, with respect to orientation. In contrast, in the "isotropic" case, multiple fibers, each pointing along different directions, would yield multiple peaks in the angular power spectrum. From experience, we have observed that a region visually appears to be isotropic when more than 4 peaks in the angular power spectrum appear. These parameters give further insight on the structural organization of fibers.

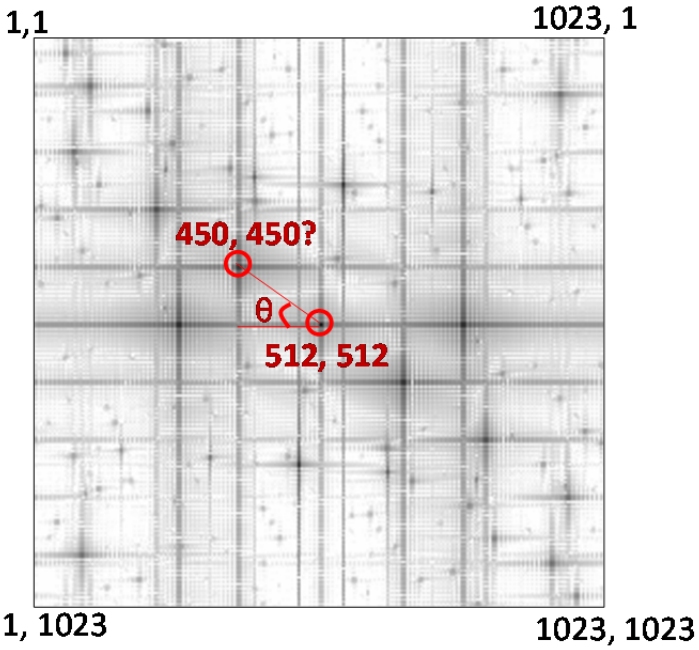


**Figure 22. Peak extraction method for calculating preferred orientation.**

Figure 23 shows an example where we apply FT-SHG to quantify collagen fiber organization in porcine cortical bone. Specifically, Fig. 23a shows an SHG image of a region in bone overlaid with an orientation map, along with dark and isotropic regions. Figures 23b and 23c are a histogram plot of orientations, and bar plot of the dark, anisotropic, and isotropic regions, respectively. The mean of orientations from the anisotropic regions is ~85.6° with an associated large spread (standard deviation) of 77.9°. In addition, there are

several isotropic (7) and dark regions (4), indicating that the collagen fibers in this particular area of bone are less ordered.

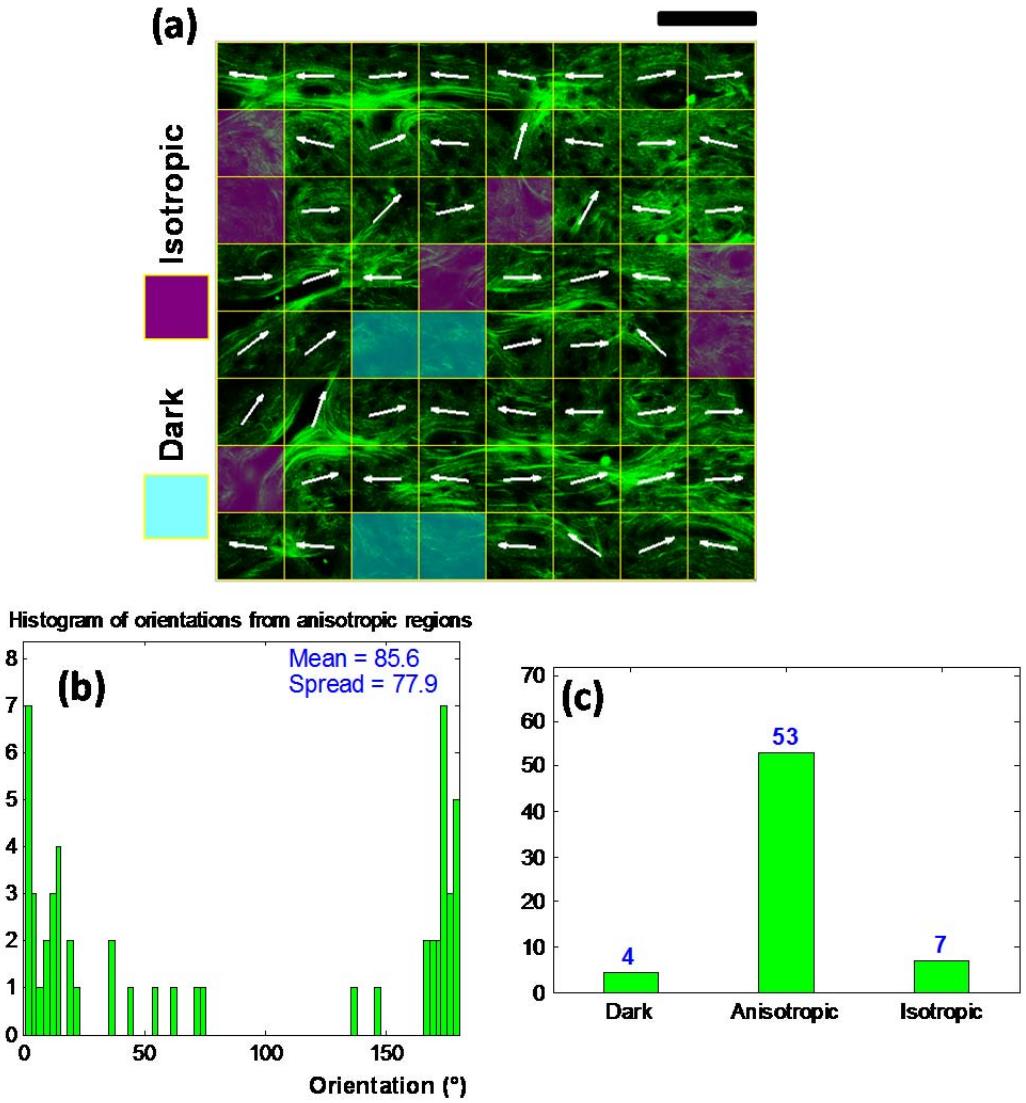


**Figure 23. (a) SHG image of collagen fibers in porcine cortical bone overlaid with orientation grid. (b) Histogram of orientations from anisotropic regions, and (c) bar plots of the number of dark, anisotropic, and isotropic regions. Scale bar: 75 µm.**

The second parameter is the maximum spatial frequency, $F_{high}$, which informs us about the minimum observable size (or feature) in real space. In general, the thickness and spacing of a 1D periodic structure can be determined via the spectrum in Fourier space. For an aperiodic structure, the Fourier transform is more complex, making it more challenging to extract

information about features in real space. In reality, our images of biological systems are between these two extremes, and often data analysis is complicated by noise due to the scattering of the photons used to acquire the image. This limits the spatial resolution that could be obtained in optical microscopy to less than the theoretical value, and hence the fidelity with which the maximum spatial frequency can be determined in Fourier space [63, 72, 77]. In our approach, we determine $F_{high}$ by extracting a line spectrum from a 2D FT either along the direction of interest or along the direction of strong frequencies, i.e., perpendicular to the preferred orientation. Then, a smoothing spline is applied to the profile using the curve fitting toolbox in Matlab. Finally, in order to mitigate the unwanted contributions of (photon) noise to our spectrum, we use a threshold of 10% above the noise floor, which is chosen from the FT of an area that clearly produces no SHG signal (black areas in images). Using this method, the threshold is determined for each specimen. The frequency at which the amplitude just reaches above the threshold is selected as $F_{high}$ as shown in the Fig. 24, which represents the minimum feature size that can be discerned above the noise floor.

Yet another parameter of interest is peaks in the magnitude spectrum of the Fourier transform, or "Fourier peaks". The peaks in the FT are basically the inflection points calculated using differentials as shown in the Fig. 25. These peaks mainly represent the spacing between the dominant fibers within the image across the preferred orientation. Figure 25 shows an example where we calculate spacings between the collagen fibers (Fig. 25a) present in tendon which is extracted from the Fourier peaks in the FT (Fig. 25b) along the direction orthogonal to the preferred orientation.

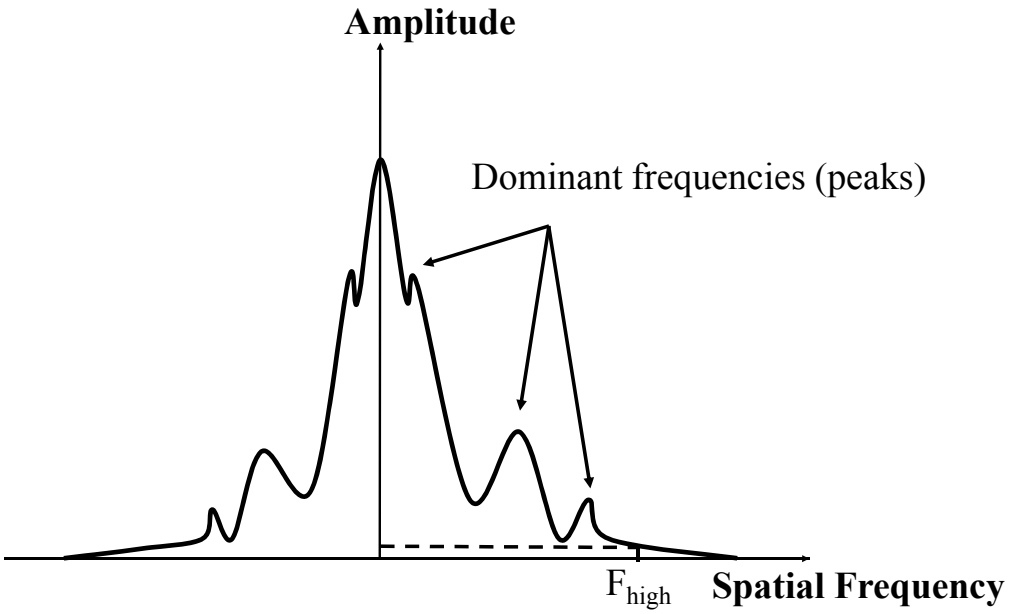


**Figure 24. Extraction of maximum spatial frequency $F_{high}$ and Fourier peaks.**

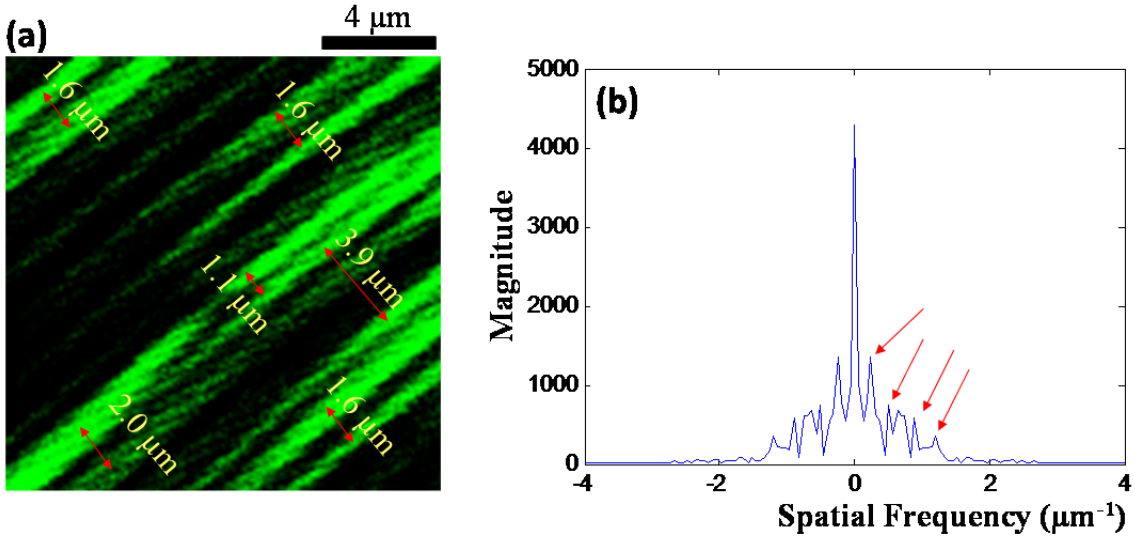


**Figure 25. Fiber spacings in tendon calculated from Fourier peaks.**

## 3.3 Experimental

### 3.3.1 Histological tissue (sample) preparation

All studies reported in this thesis are obtained from pig except when stated otherwise. The tissue samples were harvested from a local abattoir just after euthanasia, and stored in a fixative which could be 10% formalin, ethanol or 4% paraformaldehyde. All procedures were approved by the University of Illinois Institutional Animal Care and Use Committee. They are stored for at most a week; however, most of the time we prefer to perform experiments on the samples within 2-4 days. The tissues are taken out of the fixative and appropriate regions from the tissue are cut into thin slices by a surgical knife. The tissue sectioning is prepared in one of three ways:

#### *3.3.1.1 Embedding in paraffin wax*

Here, the cut slices of the tissue are placed in tissue cassettes. They are then processed for 24 hours using a standard xylene/ethanol gradient series. This ensures complete dehydration which is essential for thorough wax infiltration into the tissue. The samples are then embedded in fresh paraffin wax using a tissue processor such as Leica ASP300. 5-50 μm thick sections are cut using a motorized microtome, e.g., Leica RM 2255. These tissue sections are then mounted onto #1 glass coverslips using a permanent mounting media.

The main advantage of this technique is that the samples can be stored indefinitely for years without worrying about the integrity of the tissue structure. However, the wax is not completely transparent and scatters some light due to which the image quality is worse compared to other sample preparation techniques.

#### *3.3.1.2 Staining*

Staining basically involves the same procedure as paraffin wax embedding, but it involves a few further steps. Before mounting it between the coverslips, the samples are dewaxed and stained with either H&E or picrosirius red stain. H & E stain stains both cellular and extracellular structures; however, the picrosirius red stains only collagen fibers and also enhances the birefringence of collagen fibers, which in our experience leads to generation of

stronger SHG signal. Finally, the sections are dehydrated and secured between two glass cover slips using a permanent mounting media.

The advantage of this method is not only that the samples can be stored for long periods of time, but it also produces excellent image quality due to the absence of paraffin wax. Moreover, stain such as picrosirius red produces strong SHG signal resulting in high contrast images. The disadvantage of staining is that it may not necessarily keep the tissue in its natural state.

#### *3.3.1.3 Cryostat sectioning*

Cryostat sectioning involves working with frozen samples. Here, the tissues cut from the animal are embedded directly in OCT compound using vinyl molds and flash-frozen to preserve them at -80° C. The samples are then brought to -20° C before cutting and 5-150 μm thick sections are cut using a cryostat such as Leica CM3050S. The tissue section is then placed on a coverslip, let to thaw, and the OCT compound is washed away using PBS. It is then secured with another coverslip on top and glued on the sides using clear nail polish.

The advantage of this method is that the samples are fresh and comparatively close to their natural state. It also produces good image quality. However, since the samples cannot be preserved, they need to be imaged fresh, i.e., within 24 hrs.

### 3.3.2 Experimental setup

The schematic of the experimental setup for the SHG microscope is shown in Fig. 26. An epi-configuration two-photon fluorescence microscope is modified into a trans-configuration SHG microscope. The beam is obtained from a tunable Ti:sapphire laser (Spectra-Physics Tsunami) that produces 100 femtosecond-duration pulses at 80 MHz repetition rate. The pulses are linearly polarized and spectrally centered at 780 nm for the experiments reported here. The beam is spatially filtered and collimated before sending it to the galvanometer based *xy* scanner (Cambridge Technology) which is driven in a raster-scan pattern. After passing through a combination of relay lenses (scan and tube lens), the beam is reflected by a short-pass 680-nm dichroic beam splitter (Semrock FF670-SDi01-25X36) and subsequently

focused onto the sample using an oil-immersion objective (Leica 63X HCXPLAPO). The emitted backward SHG signal was collected by the same objective, whereas the forward signal was collected by a 0.65 NA objective. In both geometries the same two filters were used: one filter (Semrock FF01-680/SP-25) was used to block the laser wavelengths, and the other (Semrock FF01-390/18-25) was a band-pass filter to transmit the SHG signal (390 nm). A photomultiplier tube (Hamamatsu R6357 multialkali) in both geometries was used to record the forward and backward SHG images. For all samples, the average power at the input to the objective was 3-10 mW, and it provided optimum image contrast.

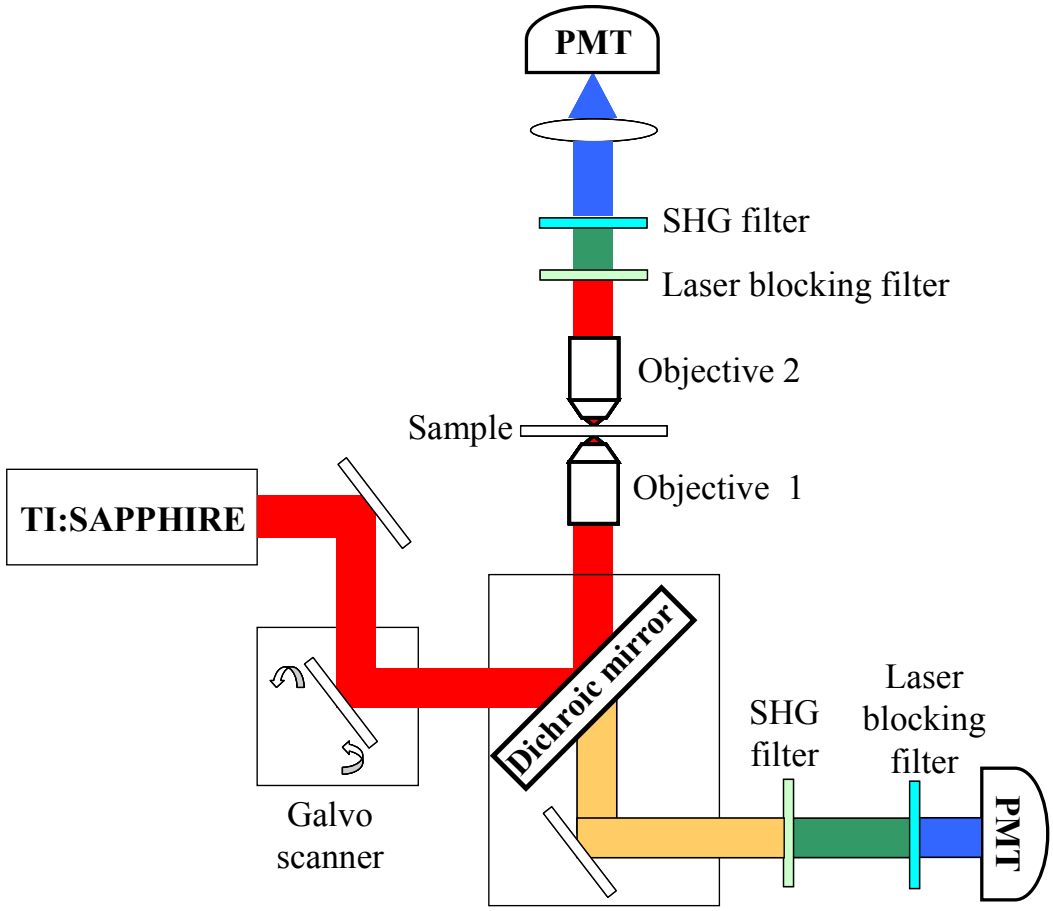


**Figure 26. Experimental setup of the SHG microscope with both forward and backward collection geometries.**

## 3.4 Results and Discussion

### 3.4.1 Introduction of FT-SHG for quantification of collagen-based tissues

In this section, we introduce how FT-SHG imaging could be potentially useful in quantifying collagen fiber organization in biological tissues [78]. In particular, we calculate two parameters: preferred orientation and maximum spatial frequency for several porcine tissues such as trachea, ear cartilage, and cornea of the eye. The FT-SHG technique is applied to 2D images as well as a 3D image stack of the cornea.

#### *3.4.1.1 SHG microscopy of trachea, ear, and cornea*

Figure 27 shows SHG images of unstained paraffin-embedded slices of adult porcine trachea (27a), ear (27b), and cornea (27c). The collagen fibers in trachea arrange in a matrix with elliptical gaps as observed in Fig. 27a. This is the expected structure of hyaline cartilage [79]. The image of the ear shows rope-like regularly oriented collagen fibers as shown in Fig. 27b. However, the cornea contains patches of collagen fibers. SHG imaging of human cornea has previously been reported [31, 33], and shows similar features to those observed in Fig. 27c. The optical sectioning capability of SHG microscopy is observed in Fig. 27d, where a 3D rendering of fibers in ear is shown.

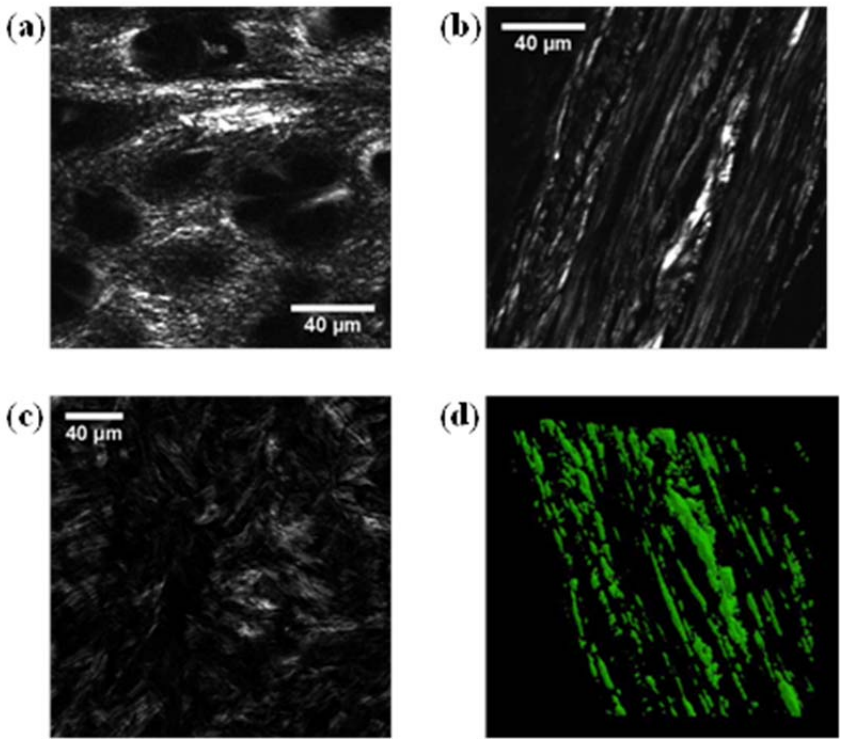


**Figure 27. SHG intensity images of porcine tissue specimens from the a) trachea and b) ear cartilage, and c) cornea for an incident wavelength of 780 nm and a second-harmonic wavelength of 390 nm; d) 3D reconstructed view of porcine ear cartilage.**

*3.4.1.2 Preferred orientation*

To estimate the preferred orientation, selected regions of the collagen fibers in porcine ear and trachea are considered as shown in Figs. 28a and 28b. Their respective 2D FT after being converted to binary images are shown in Fig. 28c. For the ear, the estimated preferred orientations for the three regions are 71.3°, 69.0°, and 69.4°, respectively. This is consistent across the regions of interest to within ~ 5°. The standard deviation (SD) is an indicator of the number of fibers that deviate from the preferred orientation. Thus, the standard deviation is higher for randomly oriented features. It is observed that the fibers are more random in region 3 (SD= 4°) compared to those in region 2 (SD=1.6°).

For the trachea, the preferred orientations in regions 4 and 5 are 45.5° and 51.8°, respectively, while the orientation in region 6 is completely different with a value of 108°.

The standard deviations are larger for trachea (on average) compared to those obtained for the ear, indicating that the collagen fibers are more randomly organized in the trachea.

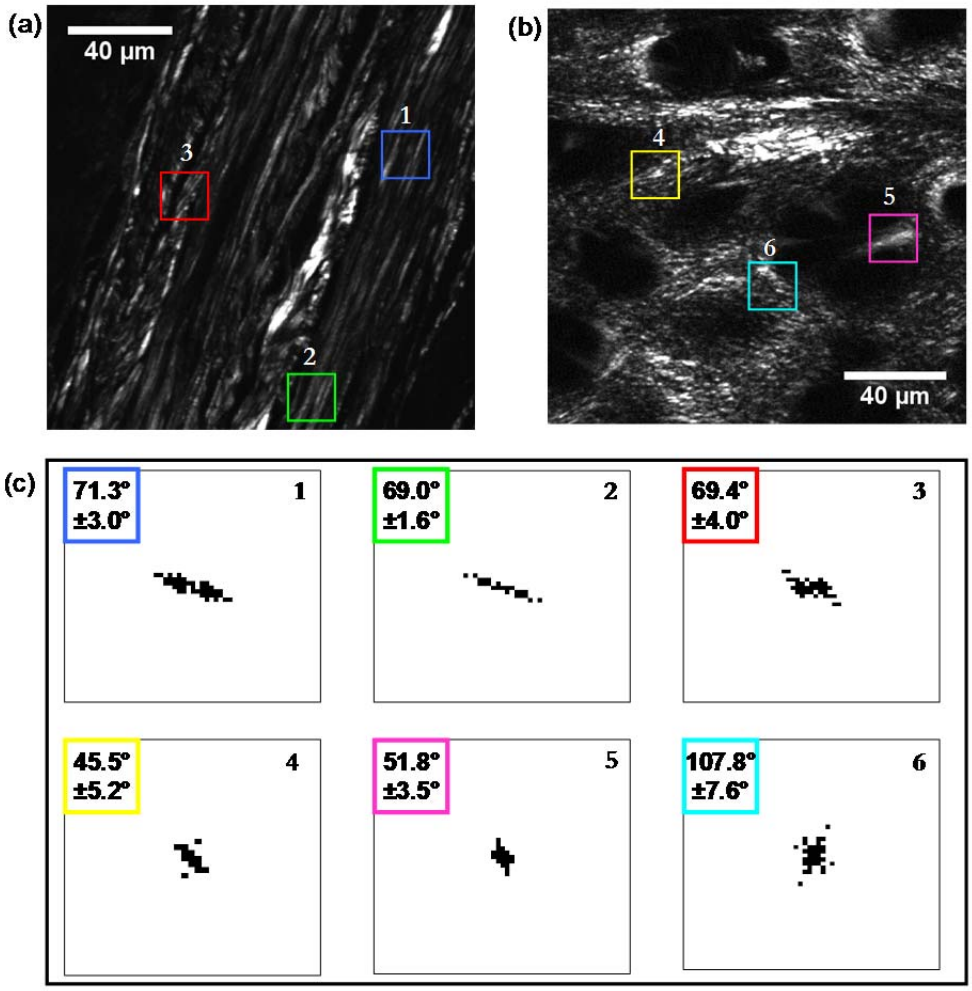


**Figure 28. SHG image of porcine a) ear and b) trachea cartilage with selected regions of interest (colored and labeled boxes), and c) estimated preferred orientation for each corresponding region as observed in Fourier space.**

*3.4.1.3 Maximum spatial frequency of biological tissues*

Maximum spatial frequencies are obtained by dividing the SHG images of porcine ear and trachea cartilage into horizontal rectangular regions of interest (for representation, we only show one) as shown in Figs. 29a and 29b, respectively. Since the preferred orientation of the

ear is relatively consistent at 70° as shown in Fig. 29c, we rotate the image of the ear by 20° so that the fibers are oriented preferentially along the vertical axis. This allows us to access the spatial frequencies along the direction of maximum variation which, in this case, is along the horizontal direction. With regards to the trachea, since the orientation varies from at least 45° to 108°, we are free to apply the same window of observation used on the ear, but without the need for any rotation of the image.

Histograms of the values of $F_{high}$ from all regions of interest of the ear and trachea are shown in Fig. 29c and 29d, respectively. Overall, the image of the ear (Fig. 29a), as observed in real space (space domain), shows consistency in its structure. This is confirmed by the narrow distribution of the values of $F_{high}$ as shown in the histogram (Fig. 29c), where the values for $F_{high}$ remain between 0.51 and 0.79 $\mu m^{-1}$. In contrast, changes in the structure of the trachea (Fig. 29b) are clearly observed in the space domain across various regions, which are confirmed by the wider distribution in the values of $F_{high}$ as shown in the Fig. 29d. Here, $F_{high}$ varies from 0.34 and 1.47 $\mu m^{-1}$. This indicates that the size of the smallest feature in the trachea changes more in comparison to the ear. The error in all values of $F_{high}$ is 0.006 $\mu m^{-1}$, which corresponds to the separation between data points in the discrete Fourier domain.

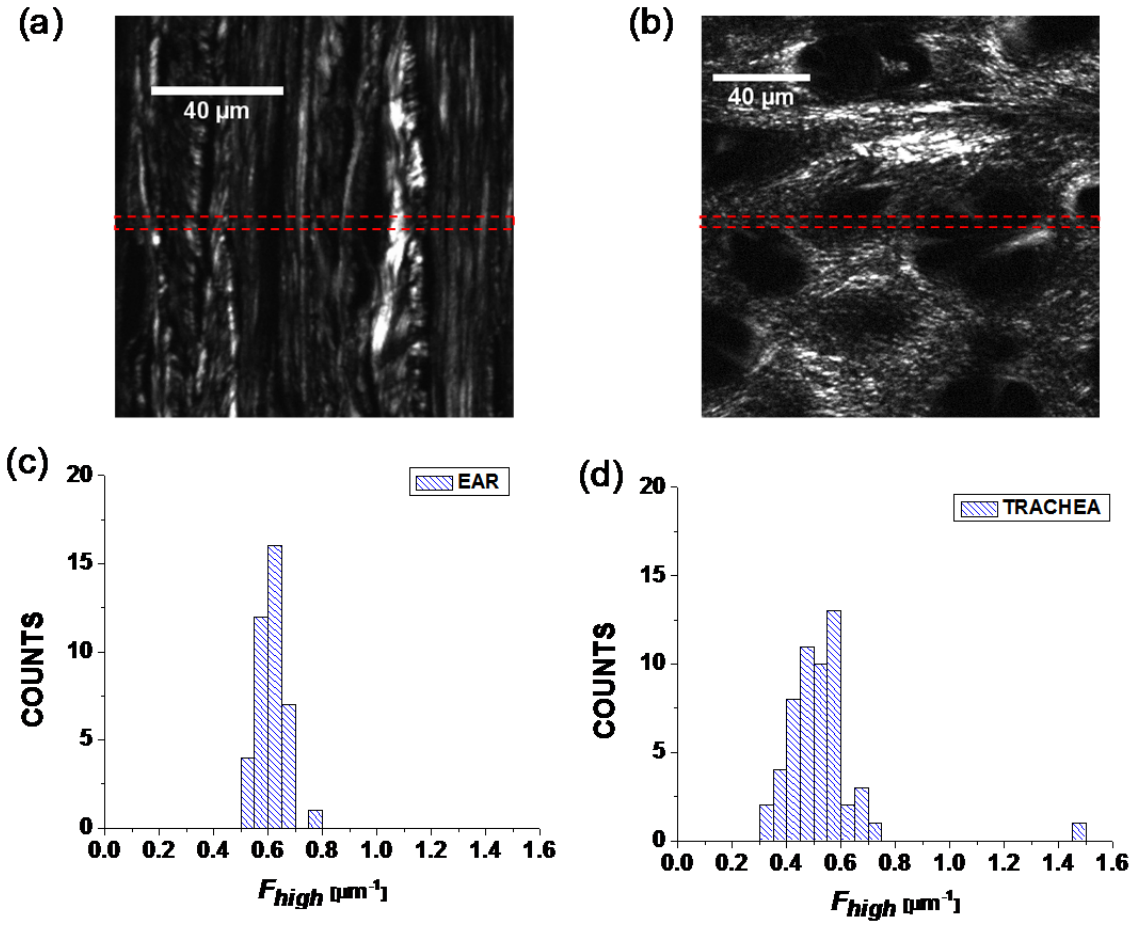


**Figure 29. SHG image of porcine a) ear and b) trachea cartilage. The region of interest for estimating $F_{high}$ is a rectangular box of height 2.87 µm. A histogram of the values of $F_{high}$ from all the regions of interest for the c) ear and d) trachea.**

*3.4.1.4 Image stack of the cornea*

Figure 30 shows the regions of interest 1-3 for a slice in the image stack of the cornea. Region 1 has a relatively large standard deviation (6.1°) due to the random orientation of its fibers. It also has lower $F_{high}$ (0.69 µm$^{-1}$) indicating that the smallest feature size is ~1.45 µm. However, regions 2 and 3 have regularly oriented fibers and thus have low standard deviations (~1.5°). In these regions, the values of $F_{high}$ are relatively large (~ 1.02 µm$^{-1}$), corresponding to smallest feature size in each region of ~ 0.98 µm. Thus, regions 2 and 3 have comparatively thinner and closer spaced features than those in region 1.

Until now, we have determined the preferred orientation and highest spatial frequency in a plane for 2D images. Next, we extend the technique to 3D by using an image stack of the porcine cornea (3-μm thick specimen). The variations in the calculated preferred orientation and $F_{high}$ versus depth, for the three regions in the image stack, are shown in Fig. 31. An image of the variations in the two quantitative parameters, preferred orientation and $F_{\text{high}}$ versus depth, for three regions of interest in the 3D image stack is shown in Fig. 31a. The arrows represent the preferred orientation of the regions, and the color of the border for each region of interest corresponds to a value of $F_{high}$ as indicated by the color bar.

For region 1, the preferred orientation appears to oscillate around 120°. The standard deviation in orientation remains relatively large (4.9° to 7.8°). This indicates that the fibers in region 1 are more randomly oriented throughout the stack. The values of $F_{high}$ are relatively small. The average value of $F_{high}$ throughout the depth is 0.77 $\mu m^{-1}$, which corresponds to a minimum feature size of 1.3 μm.

In the case of region 2, the preferred orientation decreases from 37° to 27° over a depth of 0.49 μm. It then remains constant over a depth of 1.47 μm and then increases gradually to 37° at the end of the stack. $F_{high}$ ranges from 0.73 to 1.50 $\mu m^{-1}$. It increases initially and then stays roughly the same (1.27 $\mu m^{-1}$) before it decreases to 0.80 $\mu m^{-1}$ at the end of the stack. As can be seen from Fig. 30, region 2 has more regularly oriented structures, and thus the standard deviations in orientation are smaller compared to those obtained for region 1.

For region 3, we observe that the preferred orientation remains consistent at ~ 125° throughout the stack. However, $F_{\text{high}}$ initially decreases from 0.77 to 0.44 $\mu m^{-1}$ over a depth of 0.33μm and then gradually increases until the end of the stack. This indicates that fibers become more closely packed yet maintain the same orientation. For example, the minimum feature size decreases from 2.27 μm (at a depth of 0.33 μm) to 0.79 μm (at a depth of 2.77 μm), while the orientation stays at ~ 122° without deviating by more than 5°. Moreover, the standard deviation in orientation decreases at the end of the stack indicating that fibers become more regular.

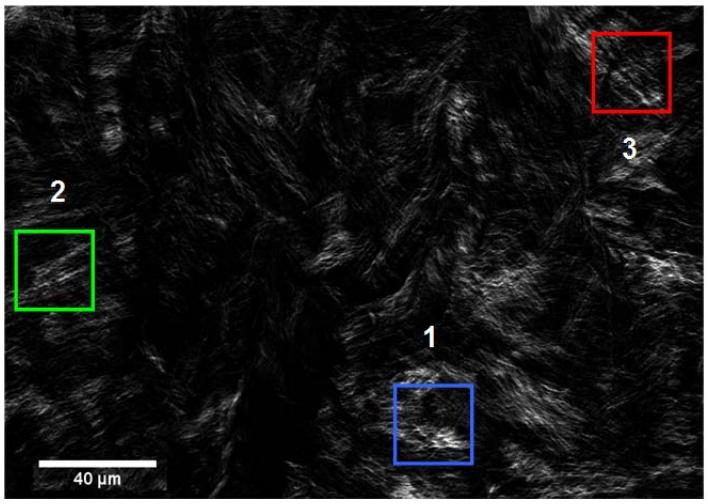


**Figure 30. Regions of interest for estimating the highest spatial frequencies in the cornea. The image shown is cropped to 238 x 163 µm.**

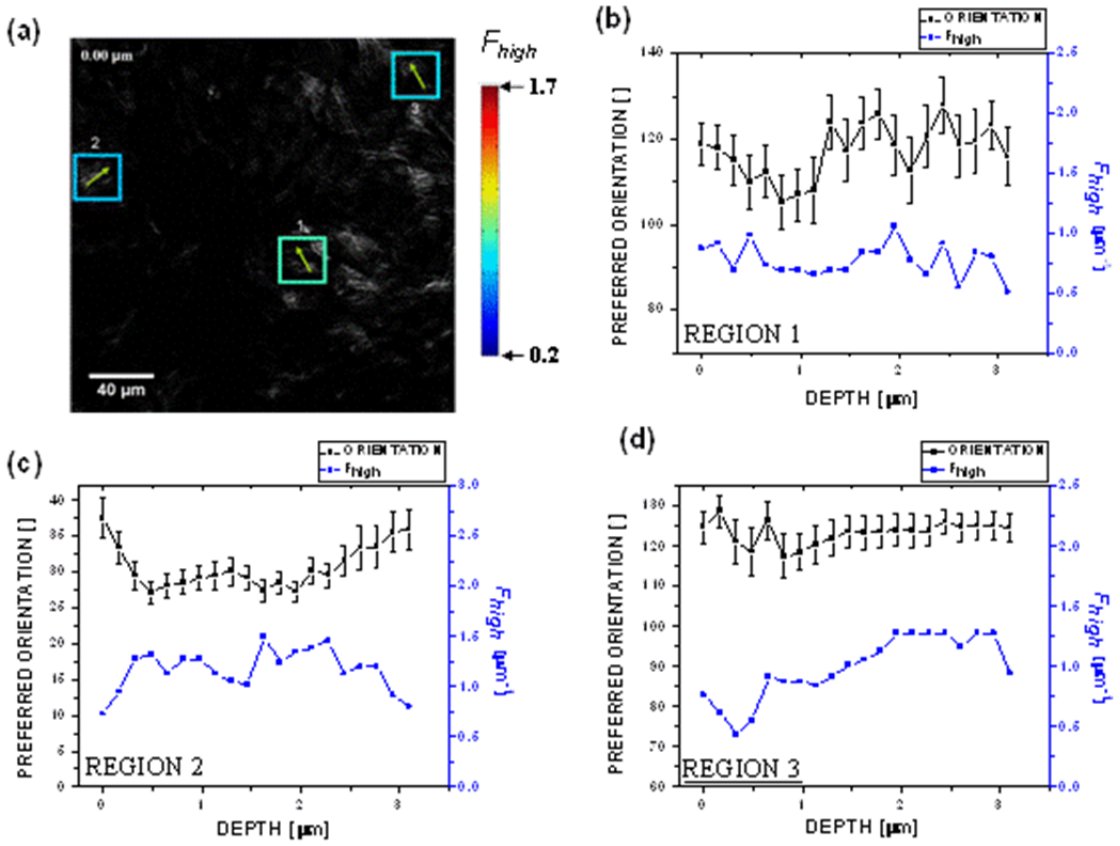


**Figure 31. a) An image showing the variations of the two quantitative markers, preferred orientation and $F_{high}$ versus depth. b-d) Plot of the estimated preferred orientation, and $F_{high}$ as a function of depth in an SHG image stack of the cornea for regions 1-3 from Fig. 30.**

We note that the size of the box chosen for estimating the preferred orientation and spatial frequency is not arbitrary. It should be chosen in such a way that it is not so small that it probes too few fibers leading to possible errors in the calculation of preferred orientation, such as those arising from a reduced number of pixels used in the FT.

#### *3.4.1.5 Conclusion*

We demonstrated the use of Fourier transform-second-harmonic generation (FT-SHG) imaging of collagen fibers as a means of performing quantitative analysis of obtained images. FT-SHG was applied to selected spatial regions in SHG images of collagen fibers in porcine trachea, ear, and cornea. Two quantitative markers, preferred orientation and maximum spatial frequency, $F_{high}$, were proposed for differentiating structural information between various spatial regions of interest in the specimens. The ear showed consistent maximum spatial frequency and orientation both in its real-space image as well as with respect to the obtained parameters. However, there were observable changes in the orientation and minimum feature size of fibers in the trachea which were quantified using our proposed parameters. Finally, the analysis was applied to a 3D image stack of the cornea. It was observed that the standard deviation of the orientation was sensitive to the variation in fiber orientation and that $F_{high}$ was sensitive to the minimum feature size. Regions that had variations in $F_{high}$ while orientation remained relatively constant, suggested that this parameter is useful as an independent marker for characterizing changes in fiber structure. We emphasize that FT-SHG is a simple, yet powerful, tool for extracting information from images that is not obvious in real space.

### 3.4.2 Quantitative analysis of forward and backward second-harmonic images using FT-SHG

Due to phase matching conditions, SHG is emitted predominantly in the forward (transmitted) direction [80, 81]. However, backward SHG (coherent) can be generated when axial scatterers are separated by distances of $\lambda_{SHG}/2$ [29, 82]. Furthermore, a backward SHG signal may also be produced from multiple scattered forward (incoherent) SHG [83]. Eventually, clinical applications and studies require the use of the backward SHG signal, and thus, it is important to understand its structural information in comparison to that of the forward SHG [82, 84]. In terms of the quantitative analysis, little has been done comparing the structural differences between the forward and backward SHG images. Typically, previous work comparing both signals has relied on quantifying the ratio of their intensities (F/B ratio) [29, 85, 86]. For example, the F/B ratio has been used to assess the thickness of fibril shells and the ionic strength of the surrounding medium [29]. In other studies, the dependence of F/B ratio on both the scattering properties of the tissue and the focal depth within the sample has been reported [85, 86]. In this section, we characterize the structural differences in collagen fiber organization for porcine tendon, sclera, and ear cartilage by comparing forward and backward SHG images using Fourier transform-second-harmonic generation (FT-SHG) microscopy [87].

In comparing the forward to backward SHG signal, we consider two quantitative metrics from FT-SHG imaging: preferred orientation, and peaks in the magnitude spectrum (Fourier transform), which are sensitive to both modulations in the signal intensity as well as the spacing between the collagen fibers. We calculate the preferred orientation for the forward and backward SHG images and use their difference ($\Delta\gamma$) as a parameter for comparison. With regard to the peak analysis, intensity peaks are simply isolated from line spectra (1D FT) taken along a direction perpendicular to the preferred orientation. Both metrics are applied to all forward and backward SHG images of the tissues studied, and at various depths into the tissues.

*3.4.2.1 Experimental*

Porcine tissue specimens of the Achilles tendon, sclera, and ear cartilage were cut, tissue sections were prepared on coverslips using Cryostat sectioning. The experimental setup is the same as that discussed in section 3.3.2. For all samples, the average power is ~ 40 mW, and the scan area is ~ 65 x 65 μm.

*3.4.2.2 Results and Discussion*

Figure 32 shows forward and backward SHG images of the tendon, sclera, and ear cartilage, collected at varying depths of 0, 10, and 20-μm into the sample. The arrows show the direction of preferred orientation for the collagen fibers within a given ROI. For the tendon and ear, it is observed that the collagen fiber orientation is fairly consistent throughout the depth of the entire sample as can be seen in both forward and backward SHG images. For the sclera, changes in preferred orientation can be seen along its depth. It is also observed that the backward SHG is lost at a depth of 20 μm for the tendon, while for the sclera it persists until a depth of 35 μm (not shown). A random arrangement of collagen fibers in sclera allows a larger portion of the forward SHG to be scattered back in the backward direction.[20]

The difference in preferred orientation $\Delta\gamma$ for forward and backward SHG (for each ROI) versus depth into the sample is shown in Fig. 33. ROIs are the same as those in Fig. 32. The plots corresponding to the tendon and ear extend to depths of 17.5 μm and 22.5 μm, respectively, after which the backward SHG signal can no longer be detected. In contrast, the difference in orientation can be plotted against a depth as far as 35 μm for the sclera. For the tendon, $\Delta\gamma$ for the forward and backward SHG images remains < 3.8° and the standard deviation remains < 4.5°. Also, region B has a smaller value of $\Delta\gamma$ compared to regions A and C. The sclera exhibits the largest value of $\Delta\gamma$ (11°) and standard deviation (8°). These large variations can be explained by randomness in collagen fiber organization. Also, $\Delta\gamma$ in region C changes less than regions A and B. For the ear, $\Delta\gamma$ remains below 5.3° and the standard deviation below 5.2°. Overall, the tendon has the smallest $\Delta\gamma$ and standard deviation compared to the sclera and ear, suggesting regular orientation as perceived by both the forward and backward SHG images. Overall, for all images $\Delta\gamma$ remains fairly small (< 11°),

indicating that a backward SHG image is sufficient to obtain information on preferential fiber orientation.

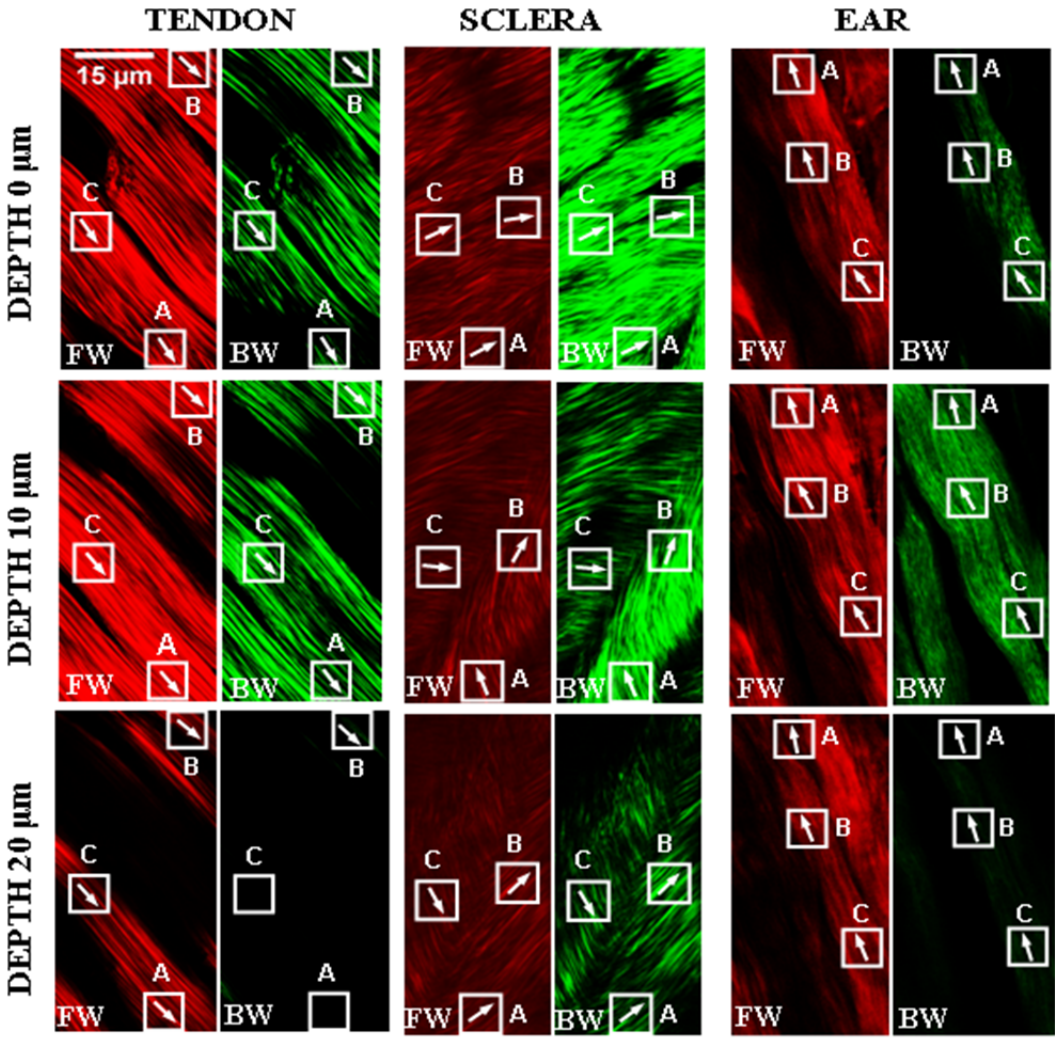


**Figure 32. Forward (red) and backward (green) SHG images of collagen fibers in the tendon, sclera and ear cartilage at various depths. Scale bar: 15 µm (same for all samples).**

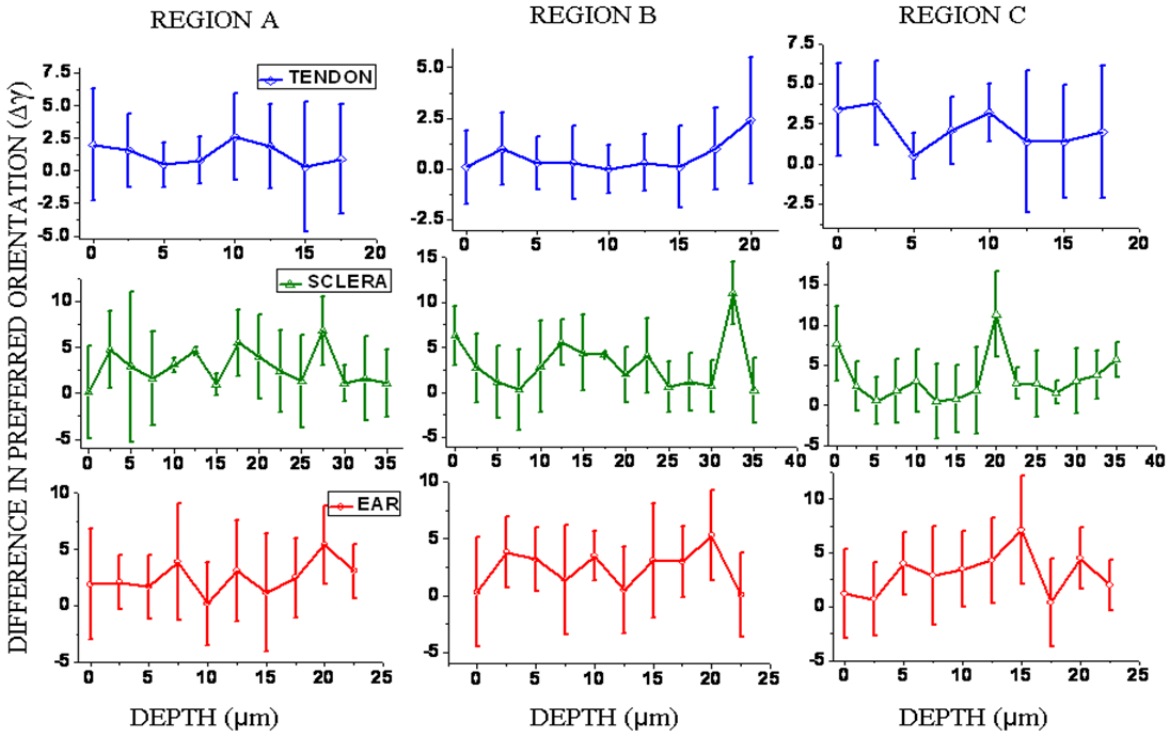


**Figure 33. Plots of the difference in the preferred orientation $\Delta\gamma$ of collagen fibers between forward and backward SHG versus depth for the same ROIs in tendon, sclera, and ear.**

Peaks in the normalized magnitude spectrum of the same ROIs for the three tissues are shown in Fig. 34. The insets show the plots at 10 and 20-μm depths into the tissues. The error in spatial frequencies is 0.015μm$^{-1}$ for these images, which is equal to the separation between data points in the discrete Fourier domain. The yellow asterisk in Fig. 34 represents peaks in the spectrum that are common to both forward (shown in black) and backward (shown in blue for tendon, green for sclera, and red for ear) SHG images. The black asterisk represents peaks in the spectrum that lie within the error in spatial frequency. Overall, there are many peaks shown that overlap between forward and backward images across all samples, suggesting that backward SHG provides a significant amount of information that can be recovered from forward SHG. It is observed that the extent of information overlap between forward and backward is related to the tissue and depth into that tissue. The backward SHG signal

provides some information that is present in the forward signal, which is encouraging for the application of backward SHG to diagnostic settings.

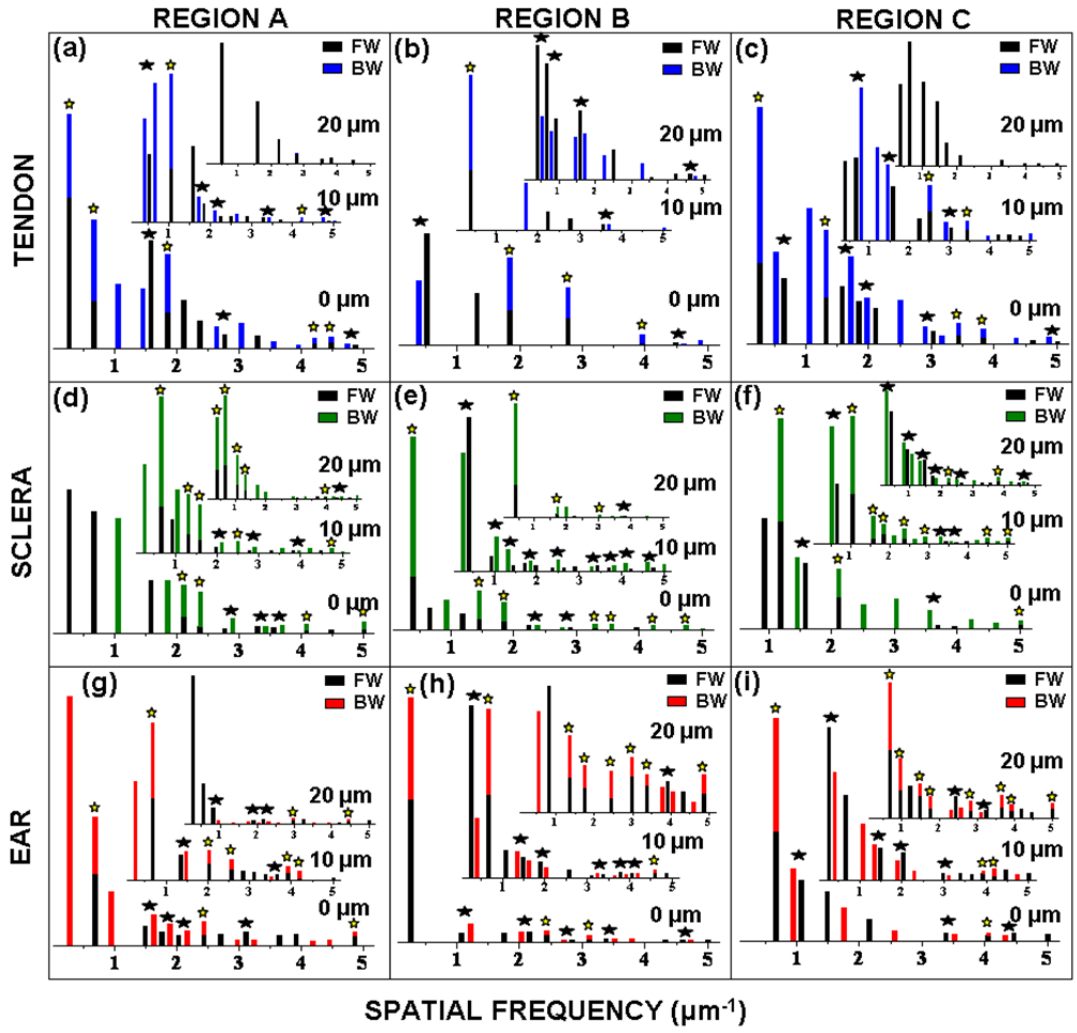


**Figure 34. Plots of spatial frequency peaks of the three ROIs at various depths for the tendon, sclera, and ear.**

In conclusion, it is observed that backward SHG images provide the same information as forward SHG images in terms of orientation (with minimal differences) for the tendon, sclera, and ear. In addition, similar information can be obtained between the backward and forward SHG images as evident from the many overlapping peaks in their spectra. The extent of information overlap between forward and backward depends on depth into the specific tissue. This study strengthens the applicability of backward SHG as a practical diagnostic tool for imaging collagen fibers. It is important to note that the information content is similar for

the aforementioned tissues; however, there exist a few tissues such as cornea for which the forward and backward do not provide similar information.

### 3.4.3 Applications to biological problems

As mentioned in the previous sections, we propose that Fourier transform-second-harmonic generation (FT-SHG) imaging could be a valuable diagnostic tool for real-world biological problems where the structure of collagen fibers changes due to damage from disease or physical injury.

#### *3.4.3.1 Quantitative analysis of collagen fiber organization in injured tendons using FT-SHG imaging*

In this section, we investigate the potential of FT-SHG imaging in evaluating collagenase-induced injury in horse tendons. The differences in collagen fiber organization between normal and injured tendon are quantified. FT-SHG microscopy is also compared with the conventional polarized light microscopy for assessing injured tendons.

##### *3.4.3.1.1 Brief introduction and background*

Tendonitis (or tendinitis) is a common and major orthopedic problem among human and equine athletes [88-90] wherein the overused tendon loses its smooth gliding (lubrication) function. This results in inflammation and chronic pain, and subsequently a long rehabilitation period. The tendon contains predominantly type I collagen which is optically birefringent in nature. Thus, several studies have utilized polarized light microscopy for converting birefringence into measurable intensity contrast for evaluating tendonitis [91-94]. It has thus become a common method for imaging collagen-based tissues and in particular for assessing tendon injury and diseases. However, polarized light microscopy suffers from a couple of drawbacks: it involves staining the collagen fibers with picrosirius red to enhance the birefringence (and hence, invasive), and is limited to two-dimensional imaging. Fortunately, as we know, collagen fibers also possess non-centrosymmetry and high second-order susceptibility—properties that allow emission of second-harmonic generation (SHG). SHG

microscopy has thus become a popular technique for obtaining high contrast and highly specific images of collagen fibers in biological tissues. The technique has also been used to study several diseases that affect collagen fiber organization [31, 95, 96]. However, according to our knowledge, it has not been heretofore applied to assessing collagenase-induced tendon injury/disease—an approach used to simulate the effects of tendonitis.

In this chapter, we compare SHG microscopy with conventional polarized light microscopy to determine its effectiveness in differentiating between normal and diseased tendon. We utilize FT-SHG imaging to quantify collagen fiber organization in various biological tissues. Here, we apply FT-SHG, along with the forward-to-backward (F/B) ratio of the emitted SHG signal, to quantify the comparison between normal and diseased tendon.

*3.4.3.1.2 Sample preparation and experimental setup*

*Sample preparation*

One clinically normal Quarter horse (age - 4 yrs) was used for the study. All procedures were approved by the University of Illinois Institutional Animal Care and Use Committee. Ultrasonographic evaluation of the flexor tendon and lameness exams were performed prior to inclusion in this study. The horse was pre-medicated with phenylbutazone (2.2 mg/kg), procaine penicillin G (22,000 IU/kg), and received a tetanus toxoid vaccine before induction of collagenase. The superficial digital flexor (SDF) tendon was injected with sterile bacterial collagenase at the mid-metacarpal region, followed by an additional dose of penicillin and phenylbutazone. The horse was maintained on strict stall confinement for 8 weeks and hand walked twice per day for the subsequent 8 weeks (total 16 weeks post-injection). Next, the subject was humanely euthanized and the collagenase-induced injured tendon sample was collected. Control (normal) tendon was also collected from the SDF tendon of the other contra lateral fore limb.

The sample preparation procedures for polarization and SHG microscopy are different; while the SHG microscopy uses cryostat sectioned samples, polarization microscopy utilizes paraffin embedded samples. For the latter procedure, the tendon samples were fixed in 4% paraformaldehyde, dehydrated, and mounted with fresh paraffin wax using a tissue processor

(Leica ASP300). 6-µm thick sections were cut using a motorized microtome (Leica RM 2255). The sections were de-waxed and subsequently stained with picrosirius red to enhance the birefringent contrast of collagen fibers. Finally, the sections were dehydrated and secured between two glass cover slips using permount mounting medium.

For cryostat sectioning, the tendon samples were embedded in OCT compound and preserved at -80° C. The samples were brought to -20° C before cutting and 25-µm thick sections were cut using a cryostat (Leica CM3050S). The orientation of the samples was similar to that of paraffin embedded samples. The samples were then thawed and secured between two glass cover slips. In this case, since the samples could not be preserved, they were imaged fresh, i.e., within 24 hrs.

*Experimental setup*

The polarized light microscope used in this study was a standard Axiovert 200M microscope (Zeiss). A halogen lamp was used as the source to illuminate the samples, and a 1388 x 1030-pixel color CCD camera (Zeiss Axiocam MRc) was used for collecting the images. The samples were illuminated through a condenser and the transmitted light scattered from the sample was collected by a 0.8 numerical aperture (NA) objective. The two crossed polarizers placed above and below the sample ensured that the birefringence introduced by stained collagen fibers was converted to intensity for visualization. Polarized images of paraffin-embedded sections of both normal and injured tendons were collected by the camera using the image acquisition software Axiovision (version 4.8.1).

The experimental setup of the SHG microscope is the same as that discussed in section 3.3.2. For all samples, the average power at the input to the objective was 3 mW. Other parameters such as pixel dwell time, detector gain, offset, and frame averaging were maintained constant between normal and injured tendon samples in both forward and backward directions to enable F/B ratio analysis.

*3.4.3.1.3 Results and discussion*

*Fourier analysis on polarized light images of normal and injured tendon*

Images of normal and injured tendon acquired using the polarized light microscope are quantified using Fourier analysis. A summary of the Fourier analysis on normal tendon is shown in Fig. 35. Images from three adjacent sites of the sample were considered for validation purposes, but only a representative image is shown (Fig. 35a). The image is overlaid with an orientation plot to display the preferred orientation of the observed structures (such as collagen fibers and crimps). The alternating bright and dark bands (along the horizontal direction) are due to the crimps in the tendon; we also observe sample preparation artifacts such as splits. These structures, along with collagen fibers, influence the calculation of orientation. It is apparent that most structures in normal tendon are oriented roughly in the range ~ 80°- 125°. Regions that are considered dark (regions with low or negligible signal) and isotropic (regions with fibers aligned along several different orientations) are counted for comparison. It is clear that there are no dark regions; however, a few isotropic regions are observed. In addition, the 2D Fourier transform is applied to the entire tendon image in Fig. 35b in order to provide an estimate of the preferred orientation of the bulk. Here, we observe a broad distribution of spatial frequencies indicating a relatively wide range of orientations as evident from Fig. 35a. A bar plot of the average number of dark, anisotropic, and isotropic regions between the three images of normal tendon is shown in Fig. 35c. The mean values of the number of dark, anisotropic, and isotropic regions are 0, 62.33, and 1.67, respectively, suggesting that most regions are anisotropic (Fig. 35c). In addition, a histogram depicting the distribution of orientation values between the three images is plotted in Fig. 35d. The associated Gaussian fit has a mean of 98.4° and a standard deviation (or spread in orientation angles) of 10.0°.

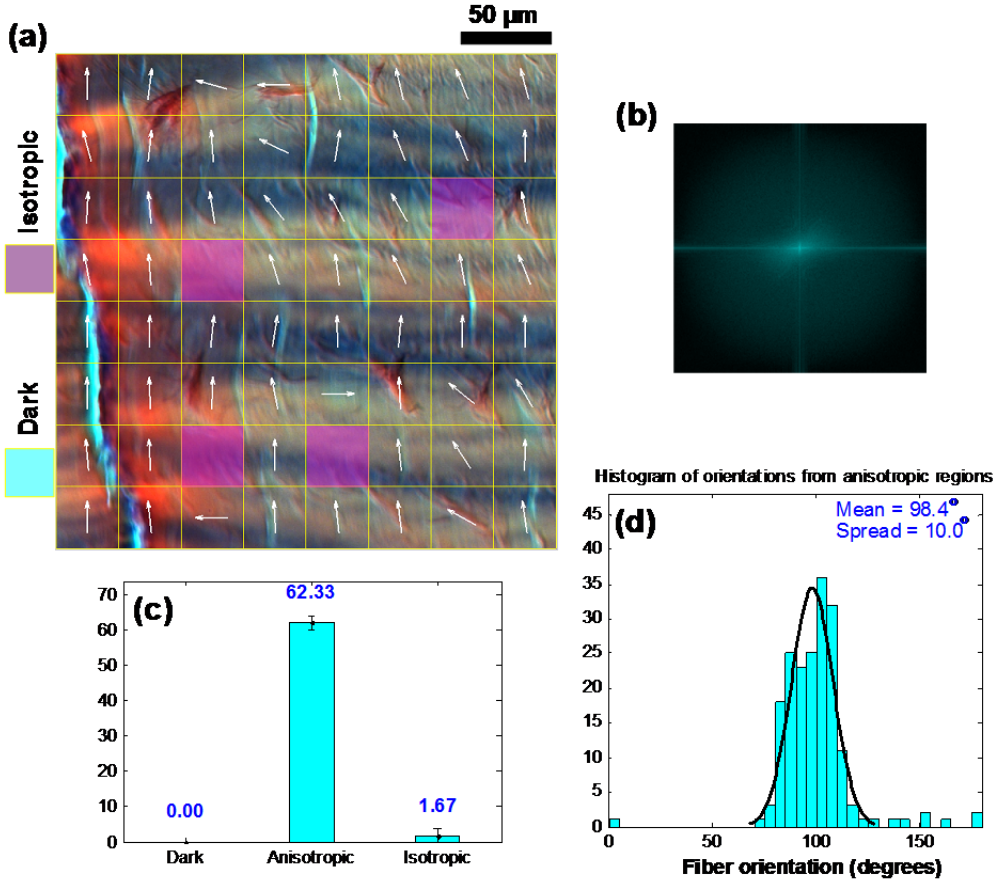


**Figure 35. (a) Polarization image of a normal tendon overlaid with an orientation plot showing the preferred orientation of structures. (b) 2D Fourier transform of the polarization image shown in (a). (c) Bar plot of the number of dark, anisotropic, and isotropic regions averaged between three separate images of normal tendon. (d) Histogram of orientation values obtained from three different regions of normal tendon.**

In Fig. 36 we apply a similar analysis as in Fig. 35 to a collagenase-induced injured tendon, where again images from three adjacent sites of the sample were considered, but only a single representative image is shown (Fig. 36a). Comparing the polarization images in Figs. 36a and 36a, there is a clear difference in the crimp pattern between the normal and injured tendon. While the normal tendon has a well defined crimp pattern and spacing, the injured tendon has an irregular crimp pattern. However, the values of orientation for the injured tendon lie in a range similar to that of the normal tendon. Moreover, the Fourier transform (Fig. 36b) and the bar plot, representing the average number of dark, anisotropic, and isotropic regions (Fig. 36c) between the three images of injured tendon, are similar to that of

the normal tendon (Fig. 36c), thereby making it difficult to distinguish. As evident from Figs. 36d and 36d, the distribution profiles of the histogram orientation for the normal and injured tendons are similar, and the difference in their mean orientations is small (<3.5°) considering their large values in spread (~10°).

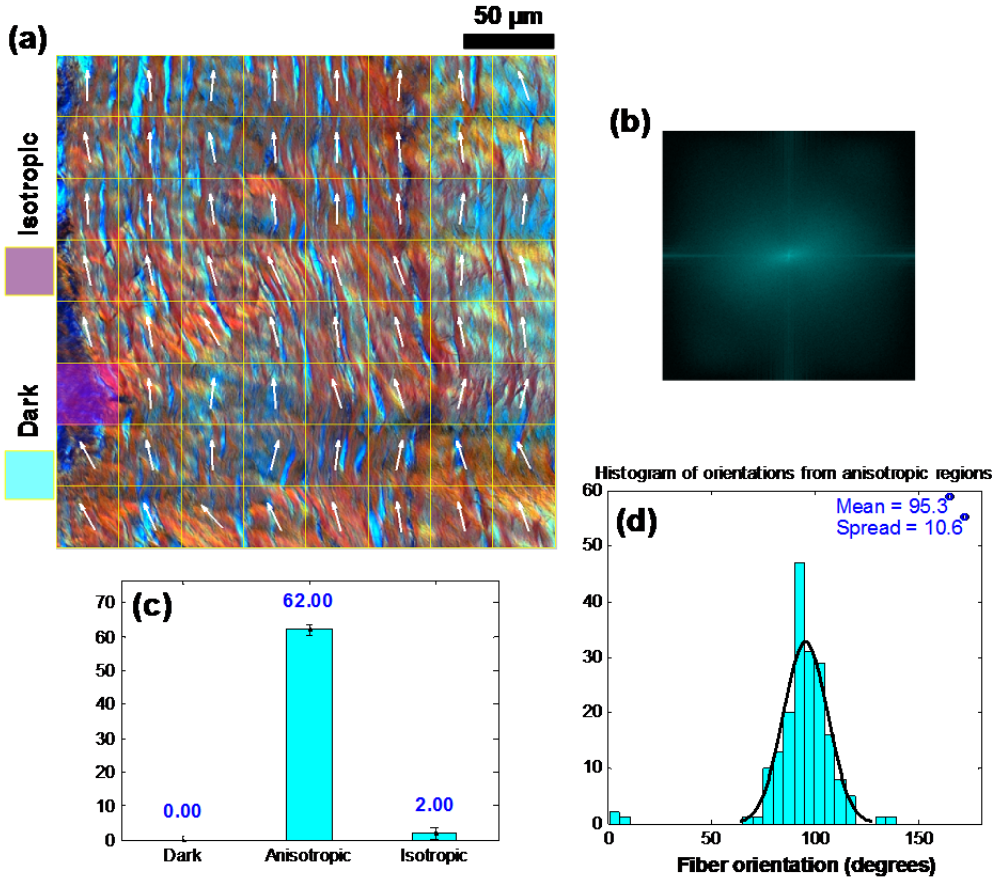


**Figure 36. (a) Polarization image of an injured tendon overlaid with an orientation plot showing the preferred orientation of structures. (b) 2D Fourier transform of the polarization image shown in (a). (c) Bar plot of the number of dark, anisotropic, and isotropic regions averaged between three separate images of injured tendon. (d) Histogram of orientation values obtained from three different regions of injured tendon.**

*Fourier analysis on SHG images of normal and injured tendon*

Figure 37 summarizes the application of FT-SHG for assessing collagen fiber organization in normal tendon. We again obtain images from three adjacent sites of the sample but choose to

present only a representative image (Fig. 37a). The overlaid orientation plot showing the orientation of collagen fibers in the SHG image of normal tendon is shown in Fig. 37a. Unlike the polarization images, the SHG images show predominantly the collagen fibers present in the tissue, as is obvious from Fig. 37a. The fibers are extremely well-oriented at ~90° in normal tendon. Although the crimp patterns are not as prominent in the SHG image as they are in the polarization images, they can still be observed. The crimps are fairly regular in normal tendon. The 2D Fourier transform is displayed in Fig. 37b. We observe two narrow lobes, horizontal and vertical, corresponding to the highly regular fibers and crimps, respectively (see Fig. 37b). Figure 37c shows the bar plot of the average number of dark, anisotropic, and isotropic regions between the three images of normal tendon. Since the fibers are regularly oriented, all regions are anisotropic. A distribution of orientation values between the three images is shown in the histogram plot in Fig. 37d. We observe that the distribution is narrow and centered at ~91° with a spread of ~3°. In Fig. 37e, an image of the forward-to-backward ratio (F/B ratio) is obtained by dividing the intensity value of each pixel in the forward SHG image by its corresponding pixel in the backward SHG image. In order to mitigate the influence of noise due to the dark regions of backward SHG image, we have considered only the pixels (using a threshold) with considerable signal above the noise floor for F/B ratio analysis. Note that the forward and backward images of normal and injured tendons are obtained using the identical optical setup and conditions, and hence a comparison of their ratios is a feasible metric. Regions where the backward intensity is greater than that of the forward are shown in green, while converse regions are shown in red. Regions with similar intensities are shown in black, while those that fall below the threshold are represented in cyan. The histogram of F/B ratios, from three separate images of normal tendon, is also shown in Fig. 37f. As evident from Figs. 37e and 37f, most regions in normal tendon produce comparable forward and backward SHG signal, and very few regions are below the threshold. The values of F/B ratio have a mean of 1.05 and a spread (standard deviation) of 0.50.

A similar procedure to that carried out in Fig. 37, is shown in Fig. 38 for a representative SHG image of injured tendon. The collagen fibers in the injured tendon shown in Fig. 38a are clearly less ordered than those in normal tendon (Fig. 37a). It is also observed that the crimps are highly irregular in the injured tendon as opposed to fairly regular crimps in the normal

tendon; this observation is consistent with the polarization images. Moreover, the Fourier transform of the injured tendon shows a single broad lobe as shown in Fig. 38b, which is an indication of the randomness (isotropy) of fiber orientations. A number of dark (mean=5.67) and isotropic (mean=6.00) regions also exist in the injured tendon, indicating the disruption of collagen fiber organization, a characteristic feature of collagenase-induced tendon injury. These observations are consistent with those previously reported in the literature [91, 92]. The injured tendon has a mean orientation of ~140° and a relatively large spread of ~17°. The F/B ratio image of injured tendon (Fig. 38e) is also different from the normal tendon (Fig. 37e). It contains more regions with intensities below the threshold, which are regions with missing fibers (dislodged fibers) due to disorganization. Figure 38f shows the histogram of F/B ratios from three separate images of injured tendon. We observe an increase in the values of the mean (1.60) and spread (1.11) for injured samples. These differences could be due to several parameters: changes in fiber organization (orientation and spacing between fibers), size, environment, and scattering coefficient of the tissue. Note that although a controlled study is required to determine the cause for the difference, we observe that the F/B ratio is still useful in differentiating normal and injured tendon.

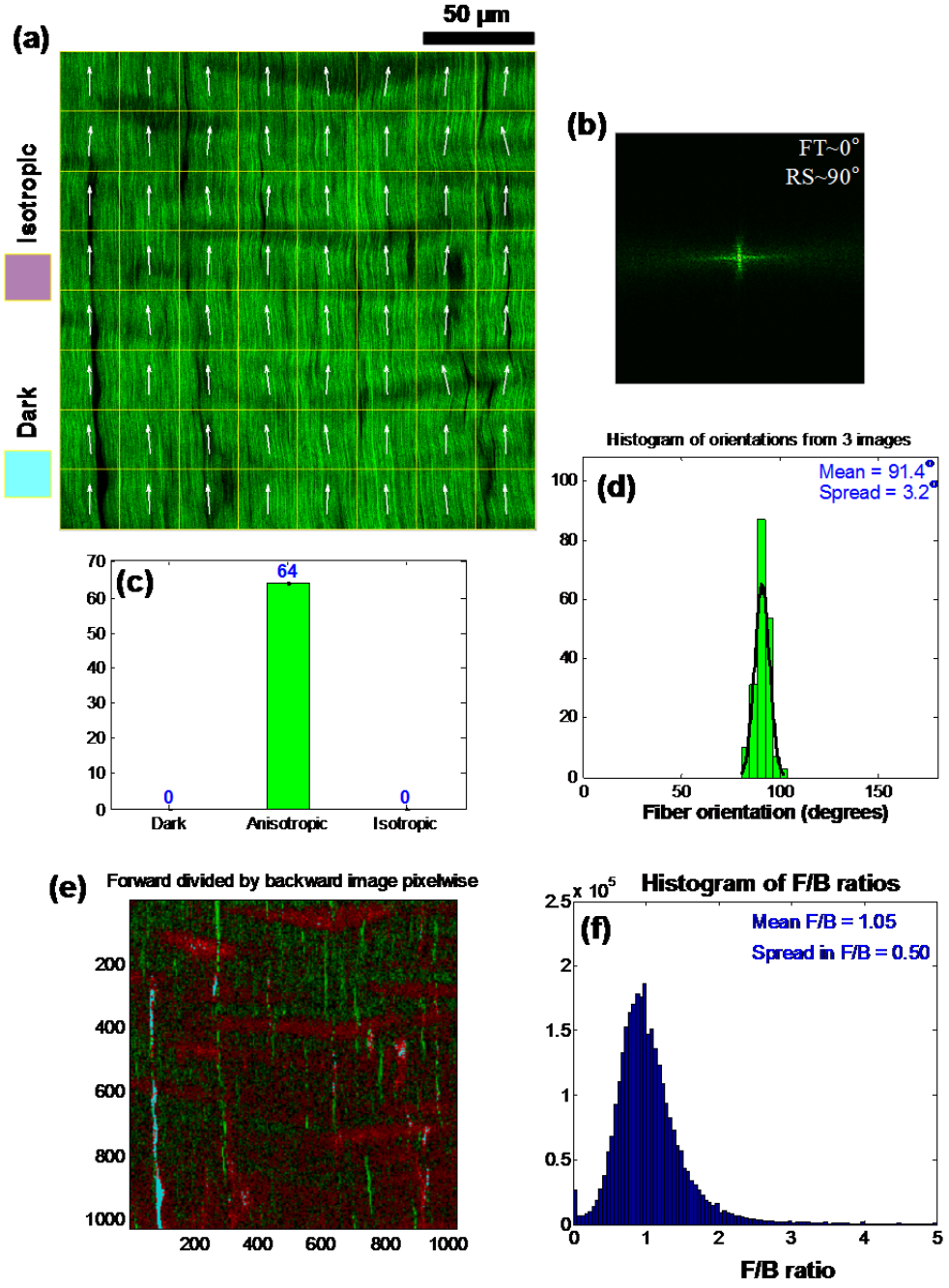


**Figure 37. (a) Preferred orientation of collagen fibers from the SHG image of normal tendon. (b) 2D Fourier transform of (a). The orientation of the Fourier transform (FT) is ~ 0° which corresponds to the orientation in real space (RS) of 90°. (c) Bar plot of number of dark, anisotropic, and isotropic regions obtained from three different regions of normal tendon. (d) Histogram of orientation from the three images of normal tendon. (e) Image of F/B ratio per pixel for normal tendon. (f) Histogram of F/B ratios from three different regions of normal tendon.**

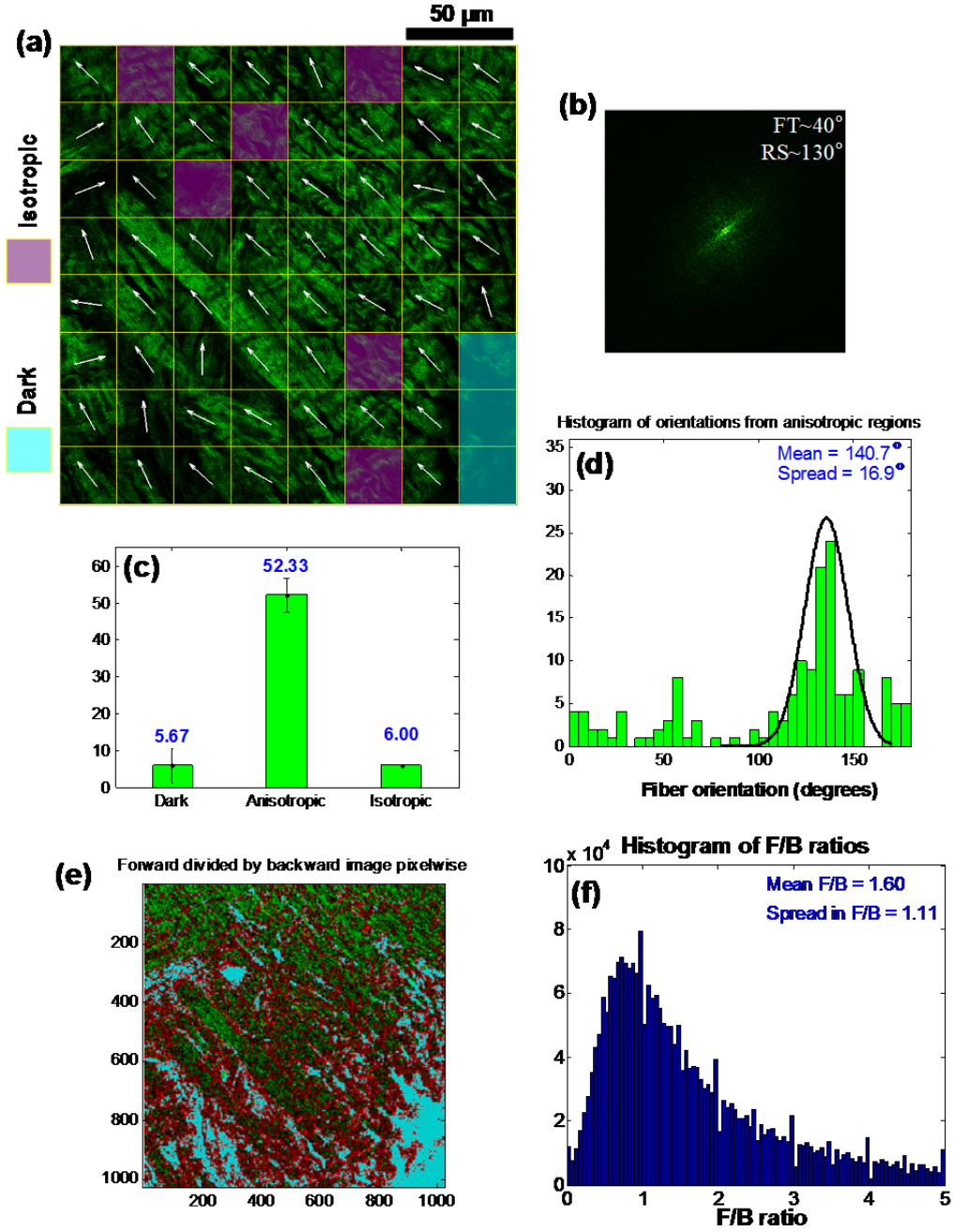


**Figure 38. (a) Preferred orientation of collagen fibers from the SHG image of injured tendon. (b) 2D Fourier transform of (a). The orientation of the Fourier transform (FT) is ~ 40° which corresponds to the orientation in real space (RS) of 130°. (c) Bar plot of number of dark, anisotropic, and isotropic regions obtained from three different regions of injured tendon. (d) Histogram of orientation from the three images of injured tendon. (e) Image of F/B ratio per pixel for injured tendon. (f) Histogram of F/B ratios from three different regions of injured tendon.**

From the above results, it is clear that SHG microscopy is advantageous over the conventional polarization microscopy for the evaluation of tendon injury. As mentioned before, the principal observable difference between normal and injured tendon images obtained from polarization microscopy is the crimp pattern. However, this technique is not well-suited for quantifying the underlying structural differences in collagen fiber organization between the two tissue types, thereby limiting assessment of injury. Yet, direct assessment of collagen fiber organization is critical in tendon injury. We observe from the above results that, FT-SHG microscopy provides us with the following aids for assessment of tendon injury: 1) noninvasive (i.e., unstained) high-contrast 3D images of collagen fiber organization that permit direct differentiation between healthy and injured tendon; 2) manifestation of the aforementioned crimp pattern (although observed with less contrast than images obtained using polarization microscopy) in healthy tendon; and 3) objective quantification of the differences in collagen fiber organization in healthy and injured tendon. The first two points, in particular, are to be expected since it is well-established that SHG microscopy is sensitive to the intrinsic noncentrosymmetric structure of collagen fibers. However, until recently, the last point on quantification of structural organization has only been made clear when the technique is combined with harmonic analysis. Thus, our results suggest that FT-SHG could be a powerful tool for assessment of damage to collagen fiber organization.

It is also important to highlight an understated advantage that SHG microscopy has over polarization microscopy for tendon injury evaluation. That is, polarization microscopy does not possess the optical sectioning capabilities of SHG microscopy, and, therefore, it cannot avoid artifacts in the surface topology of the sample potentially introduced during sample preparation. Figure 39 gives an example of this for mechanical/cutting artifacts resulting from the use of a microtome. In particular, we observe in Fig. 39a cuts or sectioning artifacts (indicated by arrows) in the polarization image of the surface of healthy tendon tissue. Similarly, breaks in the fiber structure can be seen in Fig. 39b at the surface for the corresponding SHG image. Such artifacts (in both image types) would obviously affect accurate quantification of collagen fiber organization. However, unlike polarization microscopy, an image can be obtained well below the surface, away from the deleterious

effects introduced by sample cutting. This is shown in Fig. 39c which is imaged 6 µm below the surface.

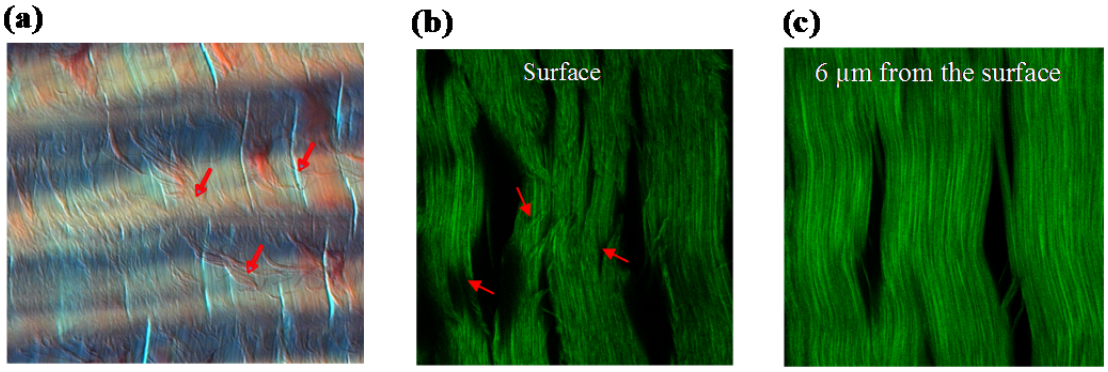


**Figure 39. (a) Polarized light image of normal tendon sample. (b) Backward SHG from the surface (c) and 6 µm into the sample. Arrows show sectioning artifacts.**

*3.4.3.1.4 Conclusion*

Fourier transform-second-harmonic generation imaging has been shown to be capable of evaluating collagenase-induced tendon injury. Clear differences in collagen fiber organization between normal and injured tendon were observed. Injured tendon displayed less ordered collagen fibers in comparison to normal tendon. This observation was further supported by the use of two additional metrics. First, the average number of dark (no/minimal signal) and isotropic (no preferred fiber orientation) regions in the images were increased for injured tendon compared to normal tendon. Second, a histogram of F/B ratios for injured tendons showed a larger spread in its distribution compared to healthy tendon. Observations of collagen fiber disorganization in injured tendons were consistent with what has been reported in the literature. Biomechanically, abnormalities in crimp structure and collagen fiber organization result in a loss of performance of normal functions (e.g., crimps allow longitudinal elongation in response to loads, and collagen fibers provide stiffness) and thus degrade a subject's ability to move. In addition, FT-SHG microscopy was shown to be more sensitive in assessing tendon injury than polarized light microscopy. It was also shown that the former technique avoids sample preparation artifacts.

*3.4.3.2 Quantitative second-harmonic generation microscopy for imaging porcine cortical bone: Comparison to SEM and its potential to investigate age-related changes*

In this section, we propose the use of second-harmonic generation (SHG) microscopy for imaging collagen fibers in porcine femoral cortical bone. The technique is compared with scanning electron microscopy (SEM); and the pros and cons of each are discussed. Due to intrinsic specificity to collagen fibers, we expect SHG microscopy to provide high contrast images of bone compared to SEM. Furthermore, in order to show how Fourier transform-second-harmonic generation (FT-SHG) imaging could be used to study bone, we provide an exploratory study where we quantitatively assess collagen fiber organization of bone structure as a function of age, from very young to mature bone. In particular, four different age groups are studied: 1 month, 3.5 month, 6 month, and 30 month.

*3.4.3.2.1 Introduction*

Bone is a mineralized connective tissue that provides the essential functions of mechanical support and haematopoiesis (production of blood cells), and acts as a reservoir for minerals, growth factors, and fatty acids [97, 98]. It is classified into two types: dense cortical bone that forms outer shell of bones, and porous trabecular bone typically found in the interior and ends of long bones [99]. The cortical bone accounts for 80% of the total bone mass in adult skeleton [100]. It consists of minerals (inorganic phase), proteins (organic phase) and fluids. Approximately 90% of the organic content in cortical bone is collagen type I. The collagen molecules (tropocollagen), mineralized with hydroxyapatite crystals, represent mineralized collagen fibrils, which are the basic structural units of bone. These mineralized fibrils are bundled into fibers of diameters approximately 2-3 μm to form woven or lamellar bone structures [101, 102]. Woven bone, found in the developing embryo and very young bone, is less organized and contains randomly distributed fibers. As the bone develops, woven bone is eventually resorbed and replaced by lamellar bone, which is made up of preferentially oriented collagen fibers, organized in lamellae, approximately 3-7-μm thick. The lamellae of adult cortical bone are arranged into the following three patterns: (1) circumferential lamellae

involving parallel layers forming the outermost shell, 2) concentric (axial) lamellae in the form of circular/elliptical rings around longitudinal vascular canals representing secondary osteons forming the Harvesian systems, and 3) interstitial lamellae, which are fragments of formerly concentric or circumferential lamellae [103]. Such hierarchical organization describes bone's complex structure, primarily responsible for biomechanical functions [2, 101, 104, 105]. Alterations to collagen's chemical composition and structural organization, which could be due to damage (e.g., in fracture callus) or disease (e.g., osteoporosis, osteogenesis imperfecta, and osteosarcoma), have serious implications for bone strength such as an increased rate of fractures [102, 106-110]. Therefore, the ability to carry out both a qualitative and quantitative assessment of the composition and structural organization of collagen fibers in bone is critical for understanding its health, and the pathogenesis and early diagnosis of a disease [111, 112].

A commonly used technique for imaging bone structure from microscale to sub-cellular scales is scanning electron microscopy (SEM) [113, 114]. The standard SEM provides high resolution images on the order of few nm (~ 2-10 nm), but at the expense of coating the surface with a heavy metal or carbon and prohibiting true volumetric imaging; i.e., the technique is limited to surface imaging. It is interesting to note that the relatively recent technology of environmental scanning electron microscopy (ESEM) relaxes the constraints in sample preparation to permit imaging of biological samples closer to their natural state at the expense of field of view, resolution (30-50 nm) and contrast [115, 116]. Fortunately, some of the problems associated with invasive sample preparation with SEM, and lower contrast and field of view with ESEM, could be alleviated through optical imaging, but at a lower resolution. For example, a commonly used optical technique for imaging bone is polarized light microscopy which utilizes the birefringence of collagen fibers in bone to produce contrast [117-119]. Confocal microscopy has also been used to visualize collagen fibers in bone [106, 107]. However, we have observed from the previous section that second-harmonic generation (SHG) microscopy has been shown to have advantages over polarized light microscopy in terms of image quality and information content, and over confocal microscopy in terms of penetration depth and intrinsic optical sectioning capability (without the loss of signal from pinhole) for imaging collagen-based tissues in 3D without the need for staining.

SHG microscopy's ability to image predominantly collagen fibers has also been experimentally validated by numerous studies using techniques such as immunofluorescence-stained light microscopy and polarized light microscopy [12, 120, 121]. However, to our knowledge, its potential has not yet been fully explored in bone imaging and the study of its age-related structural changes [32, 122-124].

In this section, we focus on the development of the quantitative SHG technique for characterization of the structural organization of collagen fibers in developing bone [125]. We also compare the use of standard SEM to that of SHG microscopy. In section 3.4.3.2.2, for both techniques, we first describe their respective sample preparation procedures and experimental setups. This is followed results and discussion (section 3.4.3.2.3), where a qualitative comparison of the bone images obtained from these approaches is performed and show a unique quantitative analysis permitted by SHG microscopy, whereby the specific example is given for quantifying changes in bone structure as a function of age. Finally, section 3.4.3.2.4 provides a summary of the work.

#### *3.4.3.2.2 Experimental*

##### *Tissue preparation*

Porcine femoral bones were obtained from the Animal Science Department at the University of Illinois at Urbana-Champaign. Porcine femurs from four different age groups were studied: 1 month, 3.5 month, 6 month, and 30 month. This age range corresponds to very young bone to mature bone. Three femurs from three different animals were used per age. Upon being collected, the femurs were cleaned of soft tissue, and immediately wrapped in PBS soaked gauze and frozen at -20°C. For sample preparation, bones were thawed in phosphate-buffered saline (PBS) solution for 12 hours. The bone samples were not demineralized in order to investigate bone in its natural state.

Samples were then cut using a band saw from the mid-diaphysis of each femur into 5-mm high, hollow cylinders. These represented whole mid-sections of bone (allowing to image whole transverse sections). A polishing machine was used to polish both ends of the cylinders with P180, P2400, and P4000 grit paper to a height of ~2-4 mm. Progressively finer polishing

cloths were used from coarse to fine, 3 μm, 1 μm and 0.25 μm, respectively. Use of fine polishing avoided artifacts due to roughness. Both ends of the cylindrical samples were polished to be parallel to each other so that either of the cross-sectional surfaces could be imaged at consistent (or same) focus. The samples were refrigerated in PBS for less than 12 hours until being imaged.

*Sample preparation for SHG imaging*

Subsequent to the aforementioned procedures being followed, these samples were then imaged under the SHG microscope without any additional sample preparation. PBS was used on the samples in order to keep them hydrated throughout the process.

*Sample preparation for SEM imaging*

Immediately after the samples were imaged using SHG microscopy, they were prepared for SEM imaging. They were first placed into a 2 % paraformaldehyde and 2.5 % glutaraldehyde solution with a 0.1 M sodium-cacodylate buffer at pH 7.4 for one day to preserve the *in vivo* tissue structure. They were then rinsed in 0.1 M sodium-cacodylate buffer for two hours on a shaker table. Samples were dried so they could be imaged under the SEM. They were soaked in 37 %, 67 %, 95 %, and 100 % ethanol concentrations for 24 hours in each concentration. Samples were then soaked in hexamethyldisilazane and allowed to air dry to avoid creation of microcracks when the ethanol evaporated from the bone. Finally, the samples were sputter coated with a layer of gold palladium. The same exact locations (marked with silver paint) were imaged with both SHG microscopy and SEM in order to compare the two techniques.

*Experimental setup*

*SEM*

A Philips XL30 ESEM-FEG Environmental Scanning Electron Microscope was used to image the bone samples. The high-vacuum (Hi-Vac) mode was used, and both the secondary electron detector and the backscatter detector were used to obtain images of the electrons scattering off the gold-palladium coated bone; ESEM in the Hi-Vac mode operates in the

same manner as the standard SEM, and thus requires drying and coating of the sample. In the user settings, an accelerated voltage of 15 kV, a spot size of 4.0 and a working distance of 10.1 are chosen to image all bone samples. Images were taken at the exact locations on the bone as the SHG images with a magnification of 75x.

*SHG microscopy*

The experimental setup is the same as that discussed in section 3.3.2. For all samples, the average power at the input to the objective was maintained at approximately 10 mW.

*3.4.3.2.3 Results and discussion*

In order to examine SHG microscopy's potential for assessing bone structure, we choose an example study where we quantify the structural changes in the collagen fiber organization of bone due to age using FT-SHG imaging. Here, relative collagen fiber orientation is considered as a parameter for quantification. As mentioned earlier, many previous studies have utilized polarized light microscopy to image bone. Interestingly, polarized light microscopy has often been used to determine the proportion of transverse to longitudinal collagen fibers across the transverse section of cortical bone, i.e., the number of in-plane to out-of-plane fibers [117-119]; also, similar information on ranges of collagen orientations has been estimated using other techniques, e.g., confocal microscopy [106, 107, 126]. However, in our current work, we focus on determining the actual orientation values for transverse (in-plane) collagen fibers relative to each other.

Figure 40 shows the application of FT-SHG to quantify collagen fiber organization in 6-month-old bone. Specifically, Fig. 40a shows an SHG image of a region in 6-month-old bone overlaid with an orientation map, along with dark and isotropic regions. Figures 40b and 40c are histogram of orientations, and bar plot of the dark regions and ratio of the number of anisotropic to isotropic regions (A.I. ratio), respectively. The mean of orientations from the anisotropic regions is ~101° with an associated large spread (standard deviation) of 41°. In addition, there are several isotropic (32) and dark regions (11), indicating that the collagen

fibers in this particular area of bone are less ordered. Along with these parameters, the number of osteons along the thickness from the outer to inner boundaries of the bone (with width of 1 mm, and corresponding areas for 1 month: ~1.6 $mm^2$, 3.5 month: ~3.1 $mm^2$, 6 month: ~3.9 $mm^2$, 30 month: ~4.3 $mm^2$) is also counted and serves as yet another parameter. Note that only whole osteons were taken into account, i.e., osteons with a Haversian canal surrounded by concentric layers of lamellae. All partial osteons commonly observed in interstitial bone were neglected. Table 3 summarizes the considered parameters: percentage of dark regions, anisotropic to isotropic ratio, number of osteons, and spread (standard deviation) in the histogram of orientations.

**Table 3. Calculated quantitative parameters for an area of 6-month-old bone shown in Fig. 40a**

| Parameters | Value |
|---|---|
| % of dark regions | 2 |
| Anisotropic/ Isotropic ratio | 20 |
| No. of osteons | 34 |
| Spread in histogram of orientations | 41 |

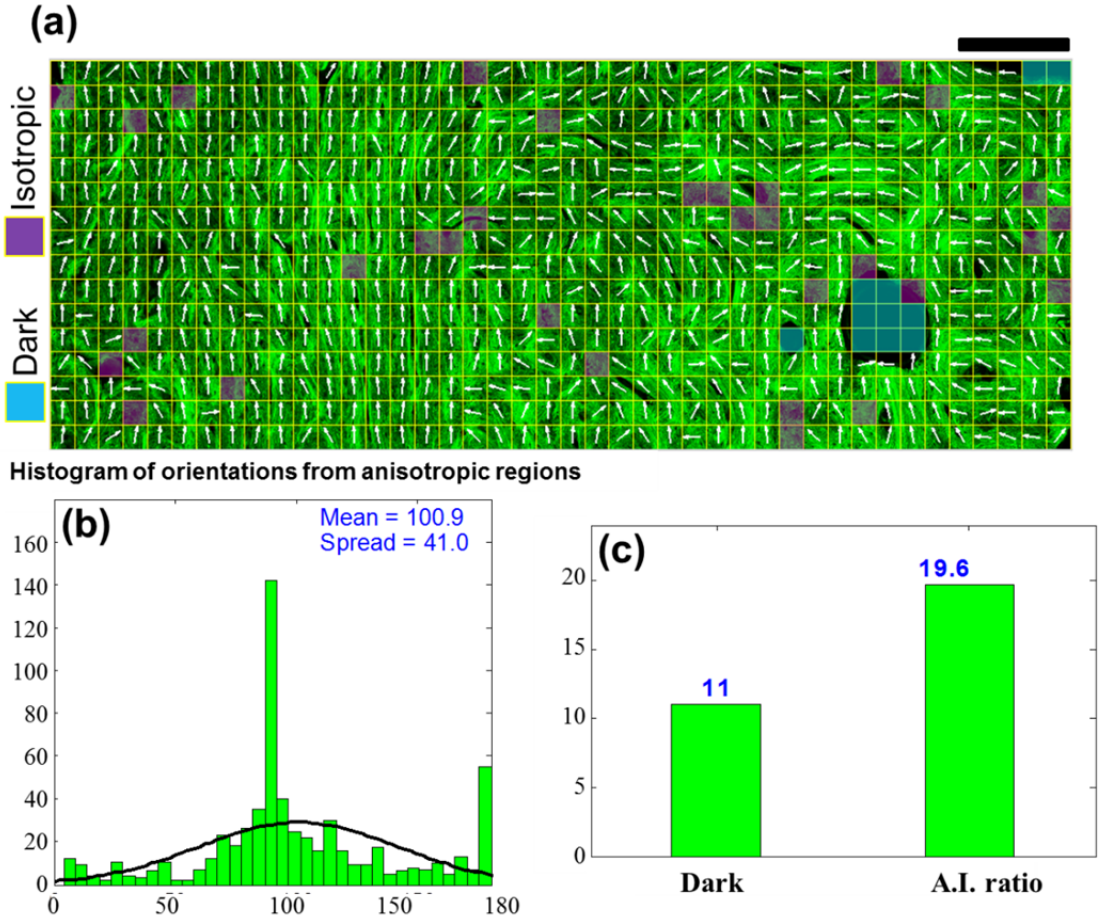


**Figure 40. (a) SHG image of collagen fibers in 6-month-old porcine bone overlaid with orientation grid. (b) Histogram of orientations from anisotropic regions, and (c) bar plots of the number of dark regions and anisotropic to isotropic ratio (A.I. ratio). Scale bar: 300 µm.**

*Regions of interest*

In order to quantify the changes in the bone structure as bone matures, we consider six regions as shown in Fig. 41. The figure shows a schematic of the right femur with anterior, medial, posterior-medial, posterior-lateral, lateral-posterior, and lateral-anterior regions. Based on our own experimental observations and published literature addressing structural changes in bone as a function of position in the transverse plane, we find that these regions represent the diverse areas on the transverse cross-section of the bone [127, 128], and thus are important for evaluation.

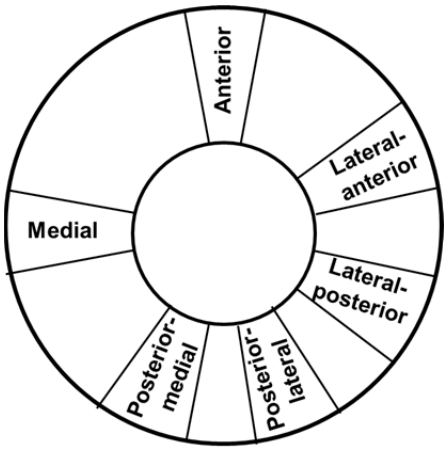


**Figure 41. Regions of interest considered on the transverse section of the right femur.**

*Qualitative comparison of SHG and SEM for imaging bone*

Figure 42a shows an SEM image of the transverse section of 6-month-old cortical bone. A magnified image of a region of interest (rectangular selection) in (a) is shown on the right. The observed SEM image is typical of a young 6-month-old cortical bone containing resorption cavities (Howship's lacunae, shown by asterisks) and forming osteons. The black ellipses in the center of the osteons represent the Harvesian canals and the smaller black elongated ellipses are the lacunae where the bone cells called osteocytes reside. The same region of bone was imaged using SHG microscopy and is shown in Fig. 42b, and the corresponding magnified image is shown to the right. Note that based on the aforementioned sample preparation procedures, SHG imaging had to be carried out on the sample before SEM. The SHG image looks similar to that of the SEM image, but it shows collagen fibers at a higher contrast. This is because of SHG's intrinsic specificity to collagen, which, as mentioned earlier, forms 90% of the organic matter in bone. Due to this high contrast, we can observe clearly the collagen fibers of diameters 2-3 μm forming circumferential, concentric, and interstitial lamellae. However, since the wavelength of photons is much larger than that (de Broglie wavelength) of electrons, the transverse spatial resolution of SHG microscopy is limited to ~ 350 nm while the SEM can provide a resolution as high as ~ 2 nm.

The above observations therefore indicate that standard SEM provides high-resolution 2D images of bone at the cost of reduced contrast of collagen fibers, while SHG microscopy provides high-contrast images of collagen fibers in bone but at the cost of comparatively lower resolution. In addition, the former technique exposes biological specimens to ionizing radiation and requires an elaborate and invasive sample preparation procedure as discussed in section 2.1 in order to obtain an image of a surface, contrary to SHG microscopy. These characteristics would be of importance when studying biological specimens in their natural state. Furthermore, although the focus of this paper is SHG imaging of collagen fiber organization of bone in 2D, the technique could be extended to three dimensions (3D). Fiber orientation and structural information in 3D could add significant more insight in assessing bone structure and hence in understanding its mechanical properties.

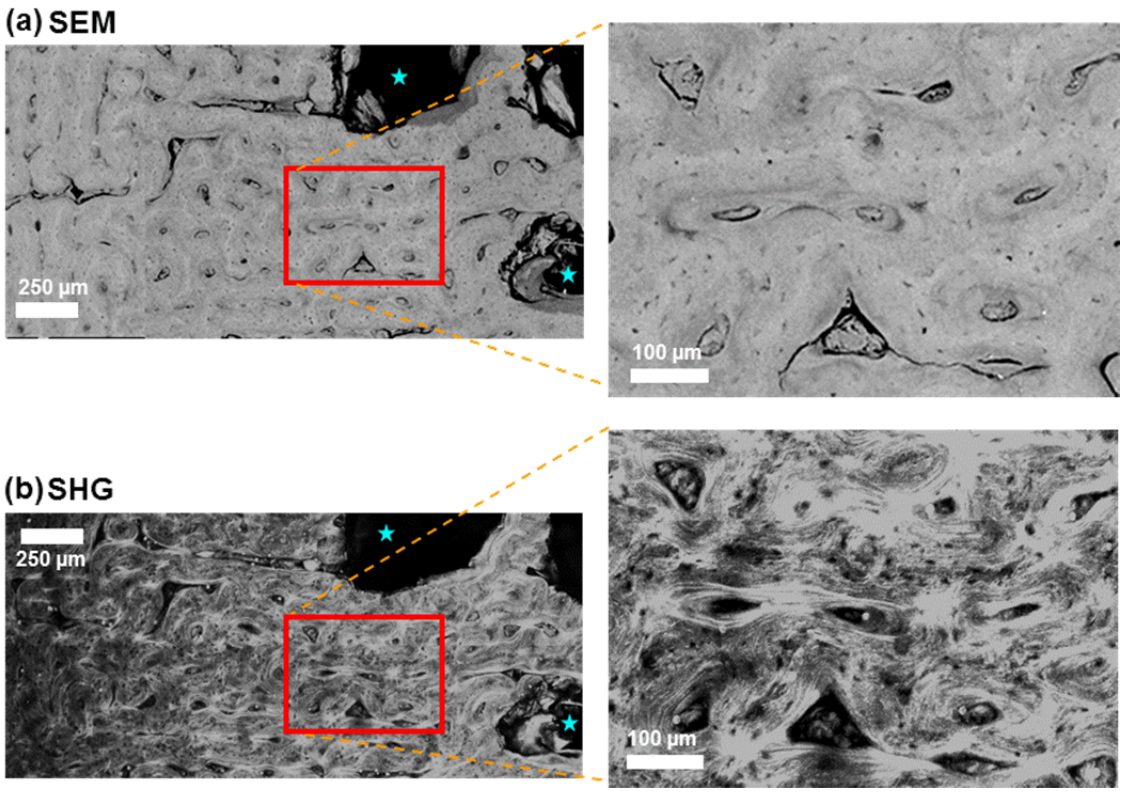


**Figure 42. (a) SEM and (b) SHG images of 6-month-old cortical bone in transverse cross-section (perpendicular to the long bone axis). Images on the right correspond to the respective magnified (~ 4x) images of a region of interest from both (a) and (b). The asterisks indicate the erosion cavities in the bone.**

*Quantitative assessment of structural changes in collagen fiber organization of bone as a function of age using FT-SHG*

FT-SHG is applied to each of the aforementioned six regions of the bone, using specimens from animals aged 1, 3.5, 6, and 30 months, and the above quantitative parameters are calculated. For basic statistics, we consider three femurs per age collected from three different animals, i.e., 6 regions per sample, 3 samples per each of 4 ages, corresponding to a total of 72 regions across all ages (18 regions per age). Shown in Fig. 43 is the bar plot of the percentage of dark regions (Dark), ratio of the anisotropic to isotropic regions (A.I. ratio), number of osteons (Osteons), and spread in the histogram of orientation (Hist. Orient.) for all ages.

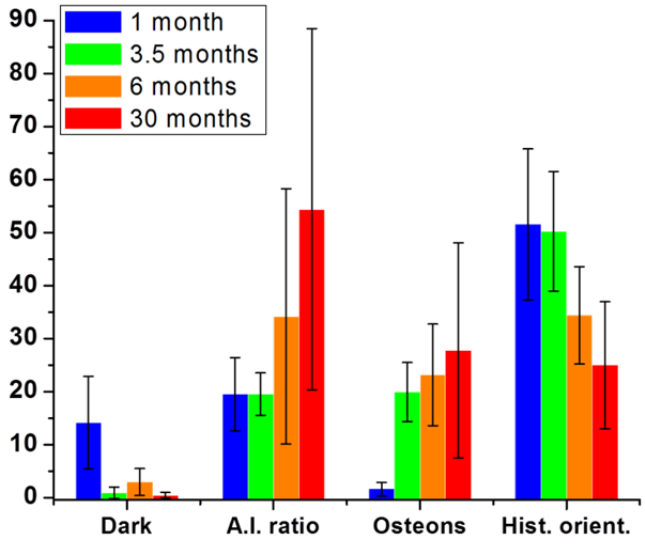


**Figure 43. Bar plot of the number of dark regions, anisotropic to isotropic ratio, number of osteons, and spread in the histogram of orientations for different ages averaged across all regions (defined in Figure 42).**

Note that our goal is to explore the technique's ability to quantitatively assess collagen fiber organization in bone as a function of age; we cannot necessarily generalize our results without carrying out a more in-depth study with a much larger number of femur specimens.

Thus, as a proof-of-concept study, we attempt to show that FT-SHG is potentially useful in quantifying structural changes in bone as a function of age. Overall, it is observed that the number of dark regions, which are erosion cavities and represent primary cavities in young bone and resorption sites in mature bone, reduces as the bone matures. The number of dark regions is much higher in the 1 month bone compared to all other ages. It is also observed that some regions in samples from the 6 month bone such as lateral-posterior and lateral-anterior (not shown) have more dark regions which accounts for its large standard deviation. 30-month-old bone has the fewest dark regions. The ratio of the anisotropic to isotropic regions gives a measure of the number of regions with highly aligned fibers in comparison with those having no preferred orientation. Again, overall, it can be observed that the ratio increases as the bone matures indicating that the collagen fibers tend to align with age. Furthermore, the number of osteons, in general, also increases as the bone matures. 1-month-old bone sample contains the fewest osteons (~2). Interestingly, while some regions of 30-month-old bone (e.g., posterior-medial) contain the most osteons (~ 60), there were regions (e.g., lateral-anterior) which contained extremely well-aligned fibers with very few osteons (~5). In addition, osteons that are fully developed with diameters of ~ 250-300 μm are frequently found in 30-month-old bone compared to younger bones. The spread in the histogram of orientations provides insight on the typical orientations from anisotropic regions in an image. It is observed that the spread decreases as the bone matures, indicating that collagen fibers across the whole cross-section of the bone tend to align to a preferred orientation. For example, regions such as medial, lateral-anterior, and lateral-posterior contain highly aligned fibers throughout the cross-section. These observations of reduced resorption sites, increased number of osteons, and increased regularity in collagen fiber alignment as the bone develops, are similar to those of previously reported studies [122, 129].

Due to the spatial heterogeneity of the bone, we also choose to evaluate the structural dependence on age for each given (or specific) region. Figure 44 shows the bar plots representing the various quantitative parameters as a function of age for anterior, medial, posterior-medial, posterior-lateral, lateral-posterior, and lateral-anterior regions. As mentioned before, the values correspond to the averages of the six regions (marked in Figure 42) obtained by imaging three different samples for each age group. Overall, it is observed that

the anterior, lateral-posterior, and lateral-anterior show more variations in the structure of bone compared to other regions. Again, as the bone matures, the following general trends are observed for most regions: decrease in the number of the dark regions (porosity), increase in the ratio of anisotropic to isotropic regions, increase in the number of osteons, and decrease in the spread in histogram of orientations. However, there are exceptions, such as a significant decrease in the number of osteons for the lateral-anterior region of 30-month-old bone compared to other ages, more dark regions for 6-month-old compared to 3.5-month-old bone in lateral-posterior and lateral-anterior regions, and decrease in A.I. ratio for 30-month-old bone compared to 6-month-old in the medial region.

Yet another interesting observation is that the variation in collagen fiber organization of bone across regions increases as the bone matures. Figure 45 shows the variations in bone structure across different regions for 1 and 30-month-old bone samples. The mean percentage of dark regions varies from 5% (medial) to 19% (lateral-anterior) for 1-month-old while it varies from 0% (lateral-anterior) to 1.2% (anterior) for 30-month-old bone. However, except for dark regions, all other parameters, such as, A.I. ratio, number of osteons, and spread all show large variations for 30-month-old compared to 1-month-old.

Interestingly, for a particular parameter, we can observe the microstructure of bone as a function of the aforementioned six regions and how it changes as bone develops. We observe that there are regions of the bone which contain more osteons and regions with more circumferential lamellae, and these regions of more osteons and circumferential lamellae change as the bone develops. For instance, we observe that a high number of osteons are found in lateral and posterior regions for 6-month-old bone. However, a high number of osteons are only found in the posterior region for 30-month-old bone. Similarly, if we consider the A.I. ratio, we see that the medial region in 6 month contains well-aligned fibers, however, at 30 months of age, these well-aligned fibers are now found in the anterior regions. Thus there exist clear differences in the structure across different regions as well as age. This is due to the fact that the various regions in the cross section of the bone are loaded (both compression and bending) differently and the bone adapts accordingly [127, 130, 131].

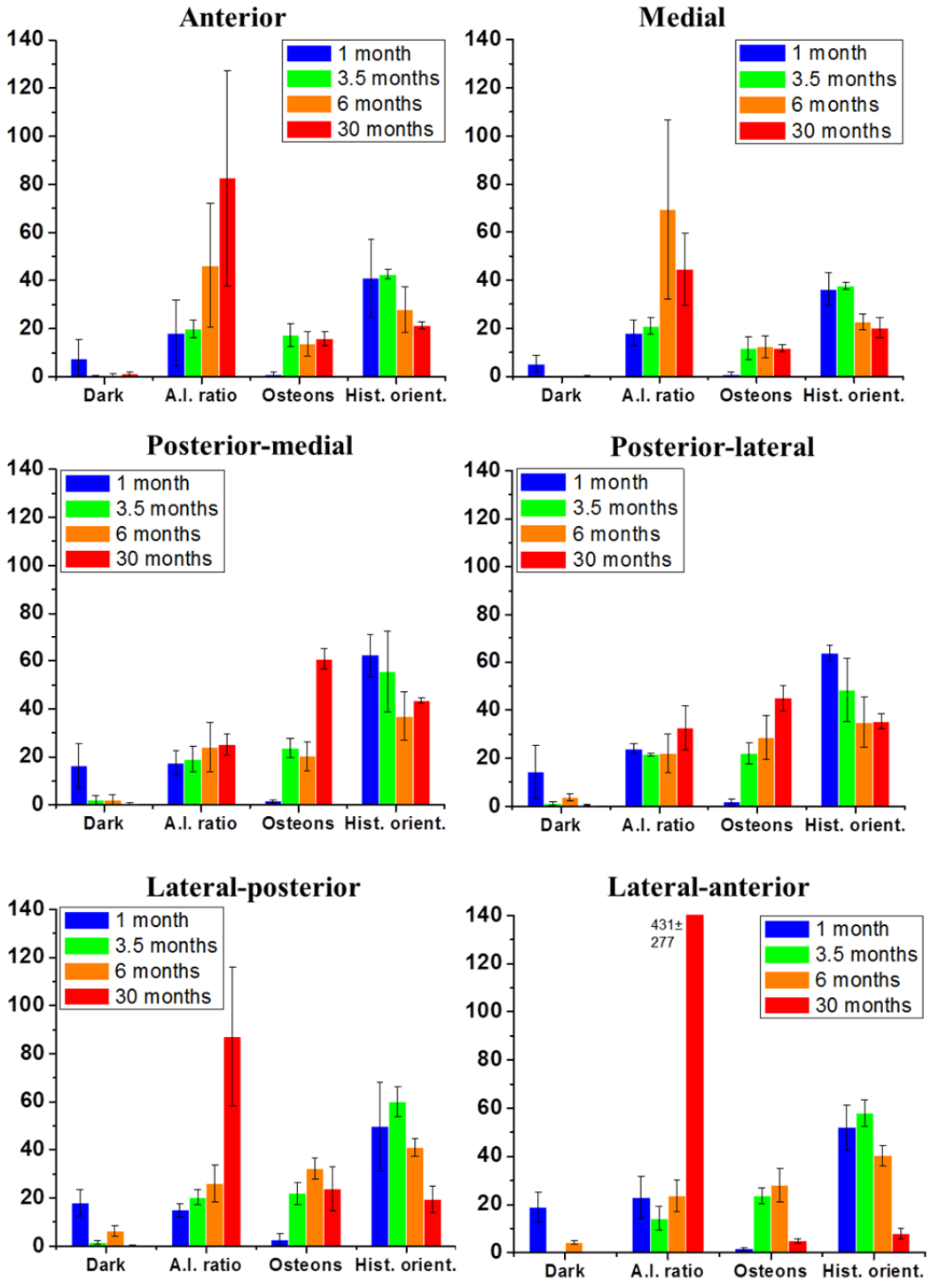


**Figure 44. Bar plots of quantitative parameters (defined in text) extracted from bone as a function of age for anterior, medial, posterior-medial, posterior-lateral, lateral-posterior, and lateral-anterior regions.**

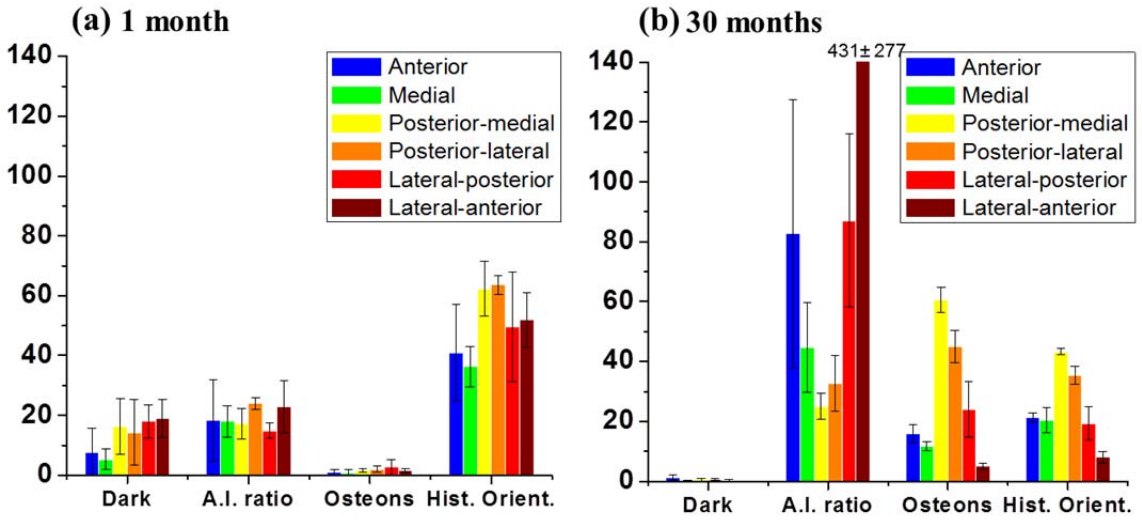


**Figure 45. Variations in bone structure across regions (displayed in Fig. 3) for bone of ages 1 month and 30 month.**

*3.4.3.2.4 Conclusion*

We applied SHG microscopy to image the collagen fibers in porcine femur and compared it with standard SEM. We find that SHG microscopy is preferred for imaging bone in cases requiring high-contrast images of collagen fiber organization without the need for sample staining. Furthermore, we showed that the use of SHG microscopy permits straightforward quantitative analysis of collagen fiber organization. As an example proof-of-concept, we applied this technique to an evaluation of fiber organization in bone as a function of age. We observed that as the bone matures, there is an overall reduction in the number of erosion sites, i.e., it becomes less porous, the number of osteons increase, and the collagen fibers become comparatively more organized. Furthermore, it is also observed that the variations in bone structure across the whole cross-section of the bone increase as the bone matures. We believe that quantitative SHG microscopy holds great promise as a valuable assessment tool for evaluating collagen fiber organization of *ex vivo* bone tissues in 3D. This could lead to better understanding of the health of bone and to early detection of the diseases that affect it, as well as an eventual development of successful strategies for treatment.

*3.4.3.3 Investigation of collagen fiber organization in cornea and sclera*

In this section, Fourier transform-second-harmonic generation (FT-SHG) microscopy is applied to quantify differences in collagen fiber organization between porcine cornea and sclera. In particular, we investigate their properties of transparency and opacity for cornea and sclera, respectively. The lamellar ordered structure of cornea is also investigated.

*3.4.3.3.1 Introduction*

One of the most intriguing questions that researchers in ophthalmology have long been trying to completely understand is: Why is cornea transparent while sclera is opaque? Cornea is the transparent front part of the eye whose main function is to act as a lens providing two-thirds of the total refractive power and form an image on the retina. On the other hand, sclera is the opaque white portion of the eye which acts as a protective layer for the inner structures. Both cornea and sclera contain predominantly collagen fibers, yet they have completely opposite optical properties. Here, we aim to investigate the differences in collagen fiber organization for cornea and sclera using FT-SHG imaging.

*3.4.3.3.2 Results and discussion*

Cryostat sectioning is used to obtain unstained samples of porcine cornea and sclera of thickness ~35 μm. Images of these samples are obtained from an SHG microscope. We apply FT-SHG to quantitatively compare the collagen fiber organization in cornea and sclera. Like before, each image is divided into square grids (Fig. 46a), and the desired quantitative parameters, such as preferred fiber orientation, the number of dark, anisotropic, and isotropic regions, are extracted. Figure 46a and 46b show the SHG images of sclera and cornea overlaid with orientation plots, and their corresponding bar plots of dark, anisotropic, and isotropic regions are also shown in Figs. 46c (sclera) and 46d (cornea). We observe that the fibers are densely organized in sclera compared to cornea as indicated by the fewer dark regions in sclera. Furthermore, on average, the fibers in sclera are thicker (~800nm) compared to cornea (~350nm). We also observe “patches” of uniform diameter and ordered collagen fibers in

cornea as opposed to relatively inhomogeneously organized and inconsistent fiber diameters (0.25-1.2μm) observed in sclera. Figure 47 shows the SHG images of two planes for cornea separated by 2 μm. It is observed that the cornea is organized into several lamellae of thickness ~ 2 μm and the orientation of collagen fibers alternate (approximately orthogonal) between successive lamella as indicated by regions 1 and 2. This has only been previously observed with electron microscopy.

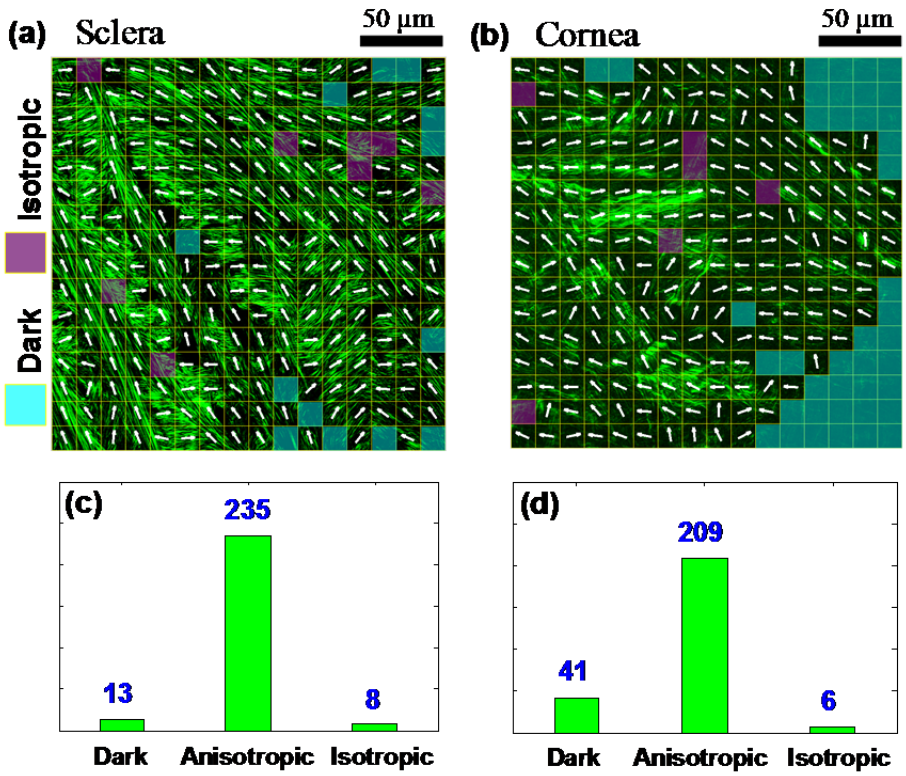


**Figure 46. Fiber orientation plots for (a) sclera and (b) cornea. Bar plots of dark, anisotropic, and isotropic regions for (c) sclera and (d) cornea.**

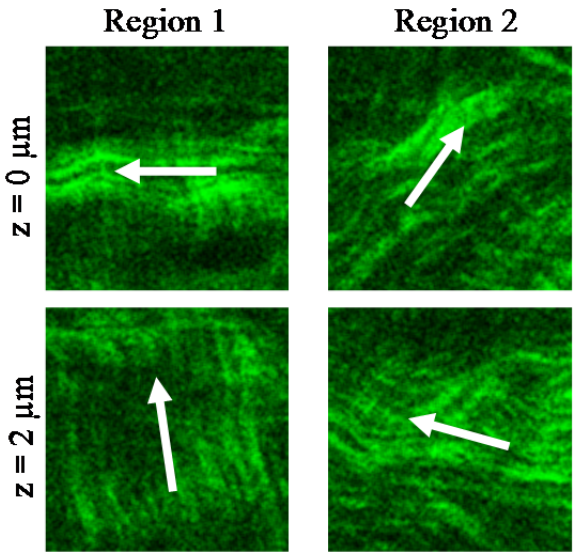


**Figure 47. SHG images of adjacent lamellae in cornea showing regions of orthogonal fiber orientations.**

*3.4.3.4 Breast cancer study: Quantifying stromal collagen structure in breast cancer biopsies*

In this section, FT-SHG imaging is employed to assess stromal collagen in several breast tissue conditions: normal, hyperplastic, dysplastic, and malignant. Since the SHG images are diffraction-limited and the resolution is ~ 500 nm, the quantifiable information is on the order of cellular scales (500nm - 100µm). Specifically, we apply a parameter that computes the regularity in collagen fiber orientation (A. I. ratio) and use it to compare across the tissue conditions.

*3.4.3.4.1 Introduction*

Breast cancer is both a leading cause of cancer deaths and among the most frequently diagnosed cancers in women worldwide [132]. In 2012, it is estimated that ~227,000 patients will be newly diagnosed and ~40,000 will die from breast cancer in the US alone [133]. In humans, almost all breast cancers arise from an uncontrolled growth of aberrant epithelial cells that originate either in the milk ducts or lobules and are categorized as ductal or lobular carcinoma, respectively. Excessive growth within human tissues can result in dense cellular

masses ranging from hyperplasia to malignant tumors [134, 135]. Though there are more cells in hyperplastic tissue, cellular structure and tissue morphology is similar to normal tissue. In dysplasia, both the cells and their organization are abnormal while neoplasia can be benign, potentially malignant (pre-cancer), or malignant (cancer). Most diagnostic and mechanistic studies in breast cancers focus on epithelial cells and significantly less work has been reported on the role of surrounding stroma and its extracellular matrix (ECM). Stromal involvement and its use as a diagnostic tool, however, is a rapidly emerging concept and is of keen contemporary interest [60, 136-139]. A number of molecular and imaging techniques have been used to characterize the stroma [52, 140-142]. In particular, the ECM predominantly contains type I fibrillar collagen [143], which has been recognized as being important for the initiation and progression of breast cancer [12, 50, 144]. Despite these promising results, the lack of analytical techniques to image the ECM is a major barrier to quantifying stromal role in breast cancer progression and, potentially, to a diagnostic protocol.

There has been much recent effort in developing useful metrics for quantifying collagen fiber organization utilizing SHG microscopy. Quantification facilitates extraction of sensitive changes in collagen fiber organization due to damage or disease, and, thus, may help in early diagnosis. Studies are needed, however, that establish this approach as a clinically compatible technique with a specific protocol for diagnostic use. Hence, the potential of SHG to understand and provide diagnostic information as well as technology development for this use are needed. As a first step towards that goal, here we first investigate the relative effectiveness of the technique, Fourier transform-second-harmonic generation imaging (FT-SHG). As we now know, FT-SHG involves utilizing 2D spatial Fourier transforms of SHG images to quantify collagen fiber organization at cellular scales (300 nm - 100 μm) [13, 78, 87, 125, 145]. Metrics such as preferred fiber orientation have been used in previous chapters/sections to successfully assess tendon injury as well as to explore age-related structural changes in cortical bone.

*3.4.3.4.2 Experiment*

*3.4.3.4.2.1 Sample preparation*

To develop any imaging modality relevant to cancer, a large sampling diversity and number must be incorporated to avoid statistical pitfalls [146]. Tissue microarrays (TMAs) consist of representative tissue materials from a large number of patients that are arranged in a grid format and represent a convenient platform for developing imaging modalities for diagnostic purposes [147, 148]. A breast tissue microarray (US Biomax BR1003) was obtained from formalin-fixed, paraffin-embedded tissue and contained 1-mm diameter circular cores of tissues for different histologic classes — normal, hyperplastic, dysplastic, and malignant (both ductal and lobular carcinoma). These samples were H&E stained and mounted in xylene based mounting medium. The sample thickness is ~ 5 μm, which is thin enough to produce high-resolution forward SHG images. It is notable that, unlike vibrational spectroscopic imaging techniques that need the sample to be unstained, the sample preparation protocol is entirely compatible with clinical processing.

*3.4.3.4.2.2 Experimental setup*

The experimental setup is the same as that discussed in section 3.3.2. An average power of < 10 mW is used for all samples. Tiled backward SHG images are collected to image the whole area (~1-mm diameter) of the tissue core. For FT-SHG analysis, the number of cores considered for normal, hyperplastic, dysplastic, and malignant tissue are 19, 16, 18, and 29, respectively.

*3.4.3.4.3 Results and discussion*

A diversity of tissue samples, with different pathologic conditions and from different patients, is available using the TMA. Figure 48 shows a selection of tissues in which the brightfield (H&E stained) and SHG images of three representative cores from the four major histologic classes can be compared. The H&E stained images are the gold standard for clinical examination of biopsies. Typically, a manual examination of the H&E images by a pathologist allows for the visualization and identification of the major cell types and locations

for imaging. While the H&E stained images provide a comprehensive view of tissue structure, the dye provides a visualization that is fairly non-specific in terms of histologic structures or underlying molecular content. The images shown in Figure 48 are selected to cover the diversity of the samples and are, thus, generally representative of the histology in breast tissue. The corresponding SHG images are shown alongside the H&E images in which the green color provides a measurable signal and black areas indicate regions without measurable signal. The SHG intensity images provide a complementary, molecularly sensitive visualization of breast tissue. As is expected, the SHG images are not sensitive to epithelial cells and these are clearly seen as missing from the images. Signal from the stromal regions, however, is large and images are of good quality. The correspondence of tissue histology and complementary information between the H&E and SHG images is enabled by the clinically compatible protocol developed here. While the combined information can be examined for synergistic effects, we focused here on the information content of SHG images first.

In SHG images, both gross areas of ECM abundance as well as finer structural detail can be observed. As a first level of stromal involvement in tumors, one expects to observe less ECM in larger tumors as the tissue volume is occupied by epithelial cells. That is, of course, a trivial outcome of the histology of solid tumors and not likely to be a very specific diagnostic parameter – hence, we do not focus on that aspect here. We have deliberately chosen TMA sections that contain some ECM for all histologic subtypes in order to analyze the stromal content with SHG. The selection of tissue regions for a valid comparison is not easy as the spatial distribution of cells within the field of view and cellularity within the ECM are obviously different for different pathologic states. Hence, we first wanted to ensure that the samples used in analysis here actually provide a measure of collagen structure and are not influenced by other microstructural entities in the tissues. We examined cellularity in the ECM in terms of the numbers of “dark” regions within the sample. A region is considered dark if the measured SHG intensity is low or negligible, which in the case of breast tissue represents an absence of collagen fibers. Figure 49 shows the bar plot of the number of dark regions within each tissue condition. The calculated values of number of dark regions are 43.6 ± 37.4, 46.6 ± 27.0, 83.2 ± 51.7, and 75.9 ± 61.4 for normal, hyperplastic, dysplastic, and malignant tissue, respectively. Applying a Kolmogorov-Smirnov comparison test, we find that

this parameter does not provide any statistically significant differences at the 0.05 level. Hence, our regions used for comparison are truly similar and the underlying morphology will not present a confounding variable.

Qualitative differences were observed in the stroma between different pathologies, but a more quantitative metric is needed for an objective test. Hence, we considered using A.I. ratio as a metric for the four pathologic conditions as shown in Fig. 50. We find the calculated values of the A.I. ratio to be 2.8 ± 1.5, 3.5 ± 2.3, 4.5 ± 3.2, and 11.6 ± 6.7 for normal, hyperplastic, dysplastic, and malignant tissue, respectively. It is also observed that the A.I. ratio is the highest for malignant tissue. Indeed, Kolmogorov-Smirnov comparison tests showed statistically significant differences in this parameter between the malignant tissue and other conditions at the 0.05 level (note that the actual corresponding p-values are very close to zero which is indicative of the strength of correlation of this parameter).

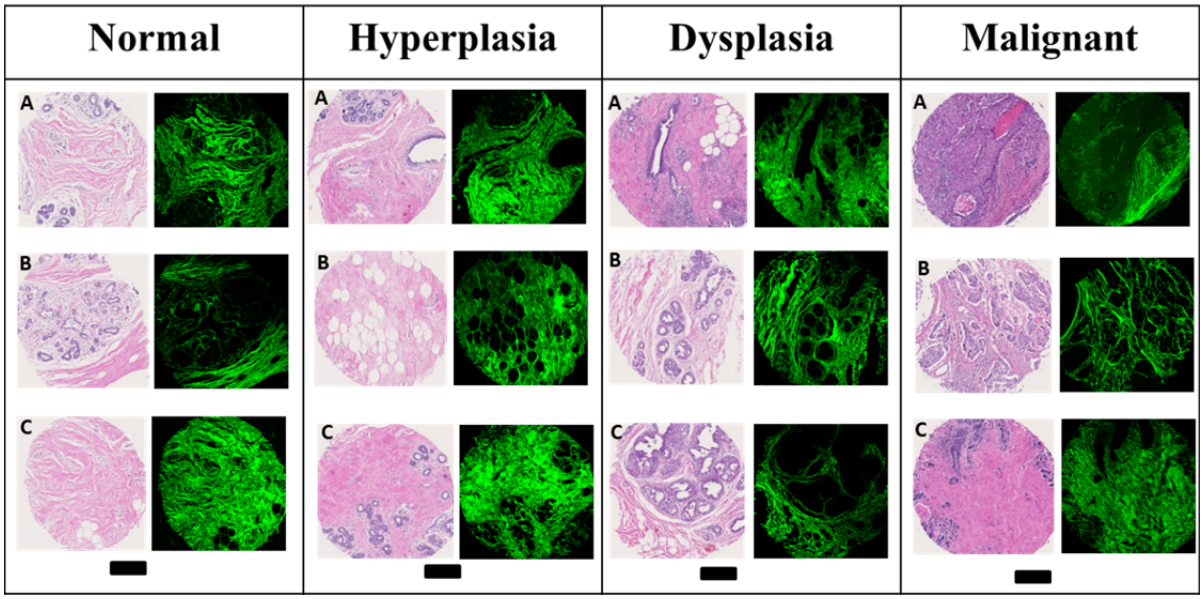


**Figure 48. H&E stained and SHG images of three cores for normal, hyperplastic, dysplastic, and malignant breast tissues. Scale bar: 250 µm.**

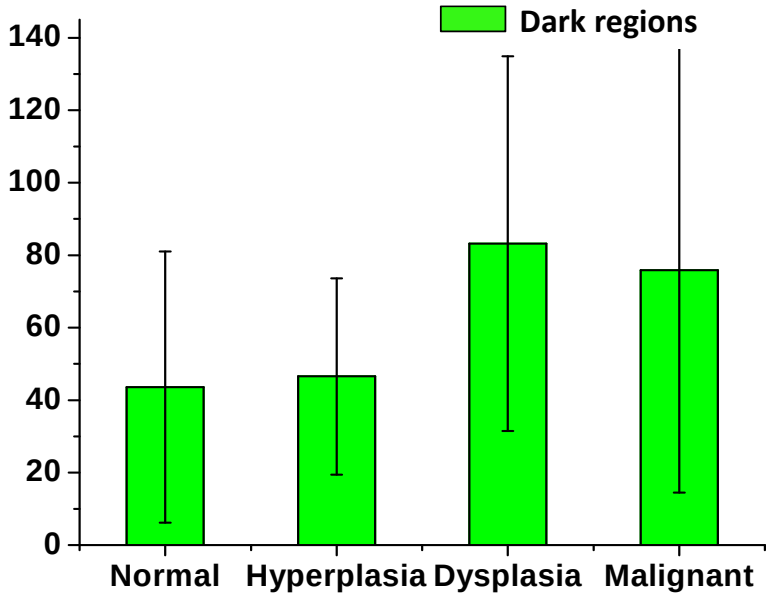


**Fig. 49. Bar plot of the number of dark regions for the four tissue conditions.**

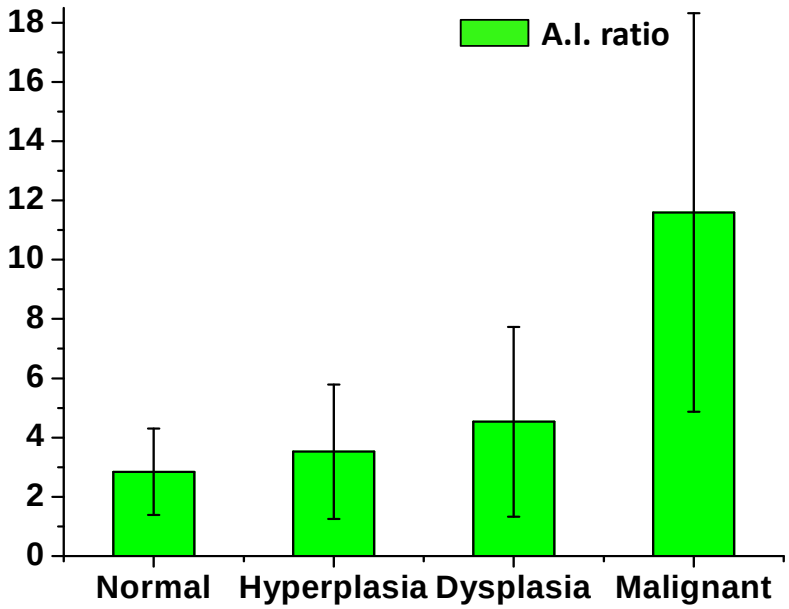


**Fig. 50. Bar plot of the parameter, A.I. ratio for the four pathologic conditions.**

### 3.5 Generalizing FT-SHG to 3D

So far, we have discussed FT-SHG for quantifying collagen fiber organization in two dimensions since the images obtained from the SHG microscope were inherently in 2D. Moreover, the tissues of interest were cut in such a way that the collagen fibers lie in a plane (the y-z plane) transverse to the propagation of the incident light (x-axis). However, in general, the tissues may contain fibers that lie at an angle with the y-z plane. For example, tissues such as bone, hyaline cartilage, and skin have collagen fibers organized in 3D. We now generalize this work by proposing three-dimensional Fourier transform-second-harmonic generation imaging (3DFT-SHG) to fully utilize the 3D imaging capability of SHG imaging and extend the scope of analysis resulting in full 3D quantification of collagen fiber organization. Here, specifically, 3D preferred orientation is used as the metric for quantification. Its accuracy is determined using known 3D test images/objects.

Although 3D FT-SHG can extract full 3D information about the fiber organization, it incurs high computational cost. Hence, the research community would greatly benefit from a simple and computationally inexpensive 3D analysis (e.g., Matlab) that can be performed relatively quickly.

#### 3.5.1 Method

We begin by acquiring a z-stack of images of the collagen-based tissue from the SHG microscope. Even though the axial resolution is usually worse compared to transverse resolution, the step-size for z-stack is chosen such that sampling is the same in all three dimensions. This basically means that we need to oversample in the z axis so that we make full use of the resolution of the microscope and also avoid problems associated with 3D interpolation. Using Matlab, the z-stack of images is read in and converted into a 3D matrix, and a 3D FT of the matrix is calculated. From the 3D FT, 3D preferred orientation can be calculated by detecting end points of the structure. Each z-plane is considered one at a time and centroid of the points above a certain intensity threshold is “tracked”. The coordinate of the endpoints, (x1,y1,z1) and (x2,y2,z2) should now give us the 3D preferred orientation in terms of theta and phi through the relations

$$\theta = \tan^{-1}\left(\frac{\sqrt{(x_2 - x_1)^2 + (y_2 - y_1)^2}}{(z_2 - z_1)}\right) \text{ and}$$

$$\phi = \tan^{-1}\left(\frac{y_2 - y_1}{x_2 - x_1}\right).$$

### 3.5.2 Preliminary results

In order to determine the accuracy of the calculated 3D preferred orientation, we generated a set of known test objects. Figures 51a and 51b show cylinders (green) oriented in 3D space at theta = 9.50°, phi = 88.50°, and theta = 5.00°, phi = 40.00°, respectively. The calculated preferred orientations for the two objects (yellow arrows) are theta = 9.00°, phi = 89.00° and theta = 5.00°, phi = 40.00°. This indicates an error of ≤ 0.5°. The method calculates the orientation accurately for all angles except when there is a degeneracy of one angle, which occurs when phi is close to 90°. This is commonly referred to as "gimbal lock" which originates from the convention of angles (theta and phi) defined in the spherical coordinate system. The whole analysis is performed using Matlab R2012a and it takes ~5 seconds for a 128 x 128 x 128 image on a basic computer with Intel dual-core processor with 3GB RAM. This method could potentially be applied to 3D images of real biological samples and is the subject of future work.


**Figure 51. Cylindrical test objects (green) oriented in 3D space and their calculated preferred orientation (yellow arrows) oriented at (a) theta = 9.50°, phi = 88.50°, and (b) theta = 5.00°, phi = 40.00°.**

Yet another method for calculating 3D preferred orientation is through the use of filter bank of lines in 3D space [149]. The 3D Fourier transform of the test object is then compared with the 3D Fourier transform of the filter banks and the one that corresponds to the maximum correlation is the best estimate of orientation for the test object. In order to decrease the computational time, we first calculate the coarse orientation with limited number of lines, and then iteratively add filter banks around the coarse orientation to calculate the precise orientation using the gradient-ascent method. The method has already been applied to calculate 3D preferred orientation for complicated test objects and biological samples such as sclera. This analysis is more accurate (<0.1°) than the former, but it takes ~ 2 minutes to complete the analysis. The method is currently being further improved and made robust so that it is applicable to several other biological samples.

# CHAPTER 4: $\chi^2$-SECOND-HARMONIC GENERATION IMAGING ($\chi^2$-SHG IMAGING)

In this chapter, we will discuss in detail the second technique, $\chi^2$-SHG imaging for quantifying collagen fiber organization in biological tissues. $\chi^2$-SHG imaging utilizes the coherent nature of SHG to extract the second-order susceptibility which provides information on molecular organization. We first introduce the theory of $\chi^2$-SHG imaging and also its experimental setup. Then, we discuss the theory where we generalize $\chi^2$-SHG from *C6* to *3m* class symmetry which is necessary when collagen fibers undergo damage or become affected by a disease.

We then utilize $\chi^2$-SHG imaging to investigate a couple of biological problems. First, we quantify differences in collagen fiber organization between cornea and sclera of the eye in order to investigate their properties of transparency and opacity, respectively. Next, $\chi^2$-SHG imaging is applied to investigate differences in stromal collagen fibers for human breast tissues from different pathologic conditions, namely normal, hyperplasia, dysplasia, and malignant. We prove that the metrics developed from the technique could be used to differentiate the tissue conditions. We also show why trigonal symmetry (*3m*) is a more appropriate model to describe collagen fibers in malignant tissues as opposed to the conventionally used hexagonal symmetry (*C6*). We then investigate whether $\chi^2$-SHG imaging is sensitive to fiber diameter. Finally, we introduce on extension of $\chi^2$-SHG to curved fibers, which is useful for generating $\chi^2$-image maps.

## 4.1 Brief Introduction

Measuring linear optical properties of biological tissues has yielded a wealth of information regarding tissue structure or composition, and tissue health, and has even been used as a diagnostic method [150-153]. By also measuring the nonlinear optical properties, we may be able to extract additional information, leading to a more thorough analysis of the tissue of interest. Just as linear refractive index (and therefore, $\chi^{(1)}$ through the relation, $\chi^{(1)} = n^2 - 1$) has been a useful measure for biological tissues, we aim to measure its second-order optical

equivalent, i.e., $\chi^{(2)}$. Moreover, due to the nature of SHG emission through coherent addition of HRS from ordered molecules as mentioned in section 2.2.8, $\chi^{(2)}$ is sensitive to molecular scale organization. In addition, SHG is a scattering process wherein the phase information is preserved (i.e., coherent), and we can utilize its extra degree of freedom — polarization. In fact, $\chi^2$-SHG imaging is a technique that utilizes its coherent nature and by modulating the incident light polarization, it is possible to obtain $\chi^{(2)}$ for collagen fibers [25, 28, 154, 155]. Assuming that type I collagen fibers possess cylindrical symmetry (*C6*) crystal class, it has previously been shown that $\chi^2$ can be used to differentiate between type I and type II collagen, muscle and type I collagen, and also to determine the orientation of molecules in collagen-based tissues [25, 28, 155]. Therefore, $\chi^2$ seems to be sensitive for detecting structural changes at the molecular scale.

### 4.2 Theory for $\chi^2$-SHG

In general, the induced polarization density ($P$) in a material is given by

$$P = \chi^{(1)}E + \chi^{(2)}E^2 + \chi^{(3)}E^3 + \ldots\ , \tag{44}$$

where $E$ is the incident electric field and $\chi^{(n)}$ is the $n^{\text{th}}$-order nonlinear susceptibility. Since SHG is a second-order process, we consider only the second term. Thus, for an incident field with an angular frequency $\omega$ interacting with a non-centrosymmetric material, the induced second-order polarization density $P$ at frequency $2\omega$ can be written as [62, 63]

$$P_i(2\omega) = 2\sum_{jk} d_{ijk}E_j(\omega)E_k(\omega)\ , \quad i,j,k = 1,2,3 \tag{45}$$

where $d_{ijk}$ is a 2$^{\text{nd}}$-rank tensor corresponding to the 2$^{\text{nd}}$-order nonlinear susceptibility, and $E_j(\omega)$, $E_k(\omega)$, and $P_i(2\omega)$ correspond to the components of the electric field and polarization density along the three principal axes of the material, respectively. Fortunately, assuming symmetry conditions such as intrinsic permutation and Kleinman symmetry (off-resonance excitation), and the fact that $P$ is Hermitian, the $d$ tensor can be represented as a 3x6 matrix, and therefore Eq. (45) can now be written as [62]

$$\begin{bmatrix} P_x(2\omega) \\ P_y(2\omega) \\ P_z(2\omega) \end{bmatrix} = 2 \begin{bmatrix} d_{11} & d_{12} & d_{13} & d_{14} & d_{15} & d_{16} \\ d_{21} & d_{22} & d_{23} & d_{24} & d_{25} & d_{26} \\ d_{31} & d_{32} & d_{33} & d_{34} & d_{35} & d_{36} \end{bmatrix} \begin{bmatrix} E_x(\omega)^2 \\ E_y(\omega)^2 \\ E_z(\omega)^2 \\ 2E_z(\omega)E_y(\omega) \\ 2E_x(\omega)E_z(\omega) \\ 2E_y(\omega)E_x(\omega) \end{bmatrix}. \quad (46)$$

Conventionally, collagen fiber is known to possess cylindrical symmetry (class *C6*), and its corresponding *d* matrix is given by [62]

$$\begin{bmatrix} 0 & 0 & 0 & 0 & d_{15} & 0 \\ 0 & 0 & 0 & d_{15} & 0 & 0 \\ d_{31} & d_{31} & d_{33} & 0 & 0 & 0 \end{bmatrix}, \quad (47)$$

where $d_{15}$, $d_{31}$, and $d_{33}$ are the only non-zero elements. Therefore, the components of the polarization density are given as

$$\begin{aligned} P_x(2\omega) &= 4d_{15}E_x(\omega)E_z(\omega) \\ P_y(2\omega) &= 4d_{15}E_z(\omega)E_y(\omega) \\ P_z(2\omega) &= 2d_{31}\left(E_x{}^2(\omega) + E_y{}^2(\omega) + E_z{}^2(\omega)\right). \end{aligned} \quad (48)$$

Figure 52 depicts the geometry that we consider of a single collagen fiber relative to an applied optical field. A collagen fiber is oriented along the *z*-axis while electric field *E* is incident normal to the *y*-*z* plane (along the *x*-axis), and $\alpha$ is the angle between the incident polarization and the *z*-axis such that $E_y(\omega) = E \sin\alpha$, and $E_z(\omega) = E \cos\alpha$. Under relatively weak focusing conditions the contribution of the longitudinal field component is much less than that of the transverse components and $E_x(\omega)$ is ~ 0. The emitted SHG intensity is the sum of induced polarization along the principal axis, i.e.,

$$I(2\omega) \sim P_x{}^2(2\omega) + P_y{}^2(2\omega) + P_z{}^2(2\omega). \quad (49)$$

Plugging Eqn. 46 into Eqn. 47, and normalizing with a particular *d* element (in this case, $d_{15}$), we obtain the emitted SHG intensity as

$$I(2\omega) \sim \left[ (\sin 2\alpha)^2 + \left( \frac{d_{31}}{d_{15}} \sin^2 \alpha + \frac{d_{33}}{d_{15}} \cos^2 \alpha \right)^2 \right]. \quad (50)$$

From this equation we observe that the values of the tensor coefficients in terms of the $d$ ratios, $d_{31}/d_{15}$ and $d_{33}/d_{15}$, can be determined by fitting the experimental plot of SHG intensity as a function of input polarization (polarization spectrum).

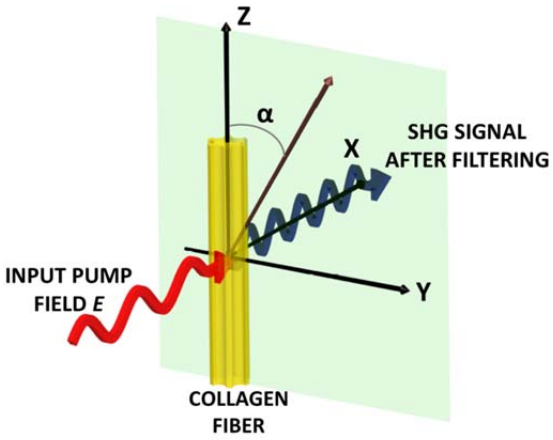


**Figure 52. Illustration of the geometric arrangement of a single collagen fiber relative to an applied electric field. The emitted SHG signal after spectral filtering is shown in blue.**

### 4.3 Experimental Setup

The schematic of the experimental setup for $\chi^2$-SHG imaging is shown in Fig. 53. It is similar to that of FT-SHG imaging; however, there are a few key changes. First, the dichroic mirror is replaced by a metal mirror in order to preserve the polarization state of the incident beam. Dichroic mirrors are known to change the polarization state and hence are avoided. This forces the microscope to only forward collection geometry. Second, high NA illumination objective is replaced by a low NA (0.6 NA) illumination objective (Olympus LUCPLFLN40X) also to preserve the polarization. Finally, a combination of half-wave plate (HWP) and polarizer is used to change the linear polarization incident on the sample from 0° to 180°. The half-wave plate is fit within an automated rotation stage for faster data

collection. The rest of the setup remains the same; i.e., Ti:sapphire laser, wavelength, galvo mirrors, and relay lenses are unchanged. Most of the time, we aim to keep the average power less than 10 mW and increase the integration time on EMCCD camera. All images are acquired from the surface of the sample to avoid birefringence and diattenuation (at large depths) [156, 157], which may further complicate the $\chi^2$-SHG analysis.

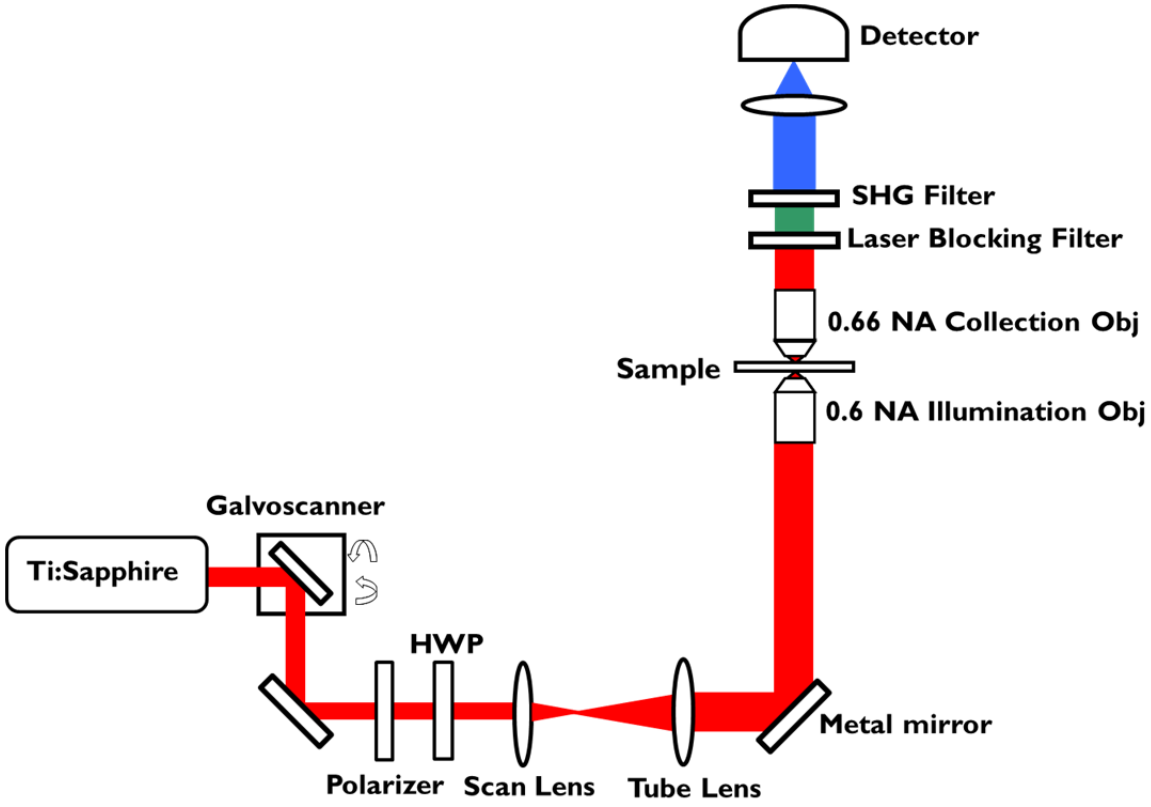


**Figure 53. Experimental setup of the $\chi^2$-SHG imaging. Details of the setup are provided in the text.**

***Calibration***

In our lab, we routinely use type I collagen scaffold or H&E stained sclera for calibration the $\chi^2$-SHG imaging. These scaffolds serve as an optical SHG tissue phantom similar to tissue phantoms used in ultrasound. Type I collagen scaffold can be prepared easily in the lab and its preparation method is provided in the Appendix A. The fiber diameters are ~ 0.5 µm as shown in the Fig. 54a. Seven collagen fibers were randomly selected and their SHG

intensities are collected while changing the polarization angle, and the polarization spectra are shown in the Fig. 54b. After fitting these experimental plots with Eqn. 48, the values of *d* ratios, $d_{31}/d_{15}$ and $d_{33}/d_{15}$, were found to be 1.17 ± 0.08 and 1.9 ± 0.13 units, respectively. These values are consistent with what has been reported previously [28].

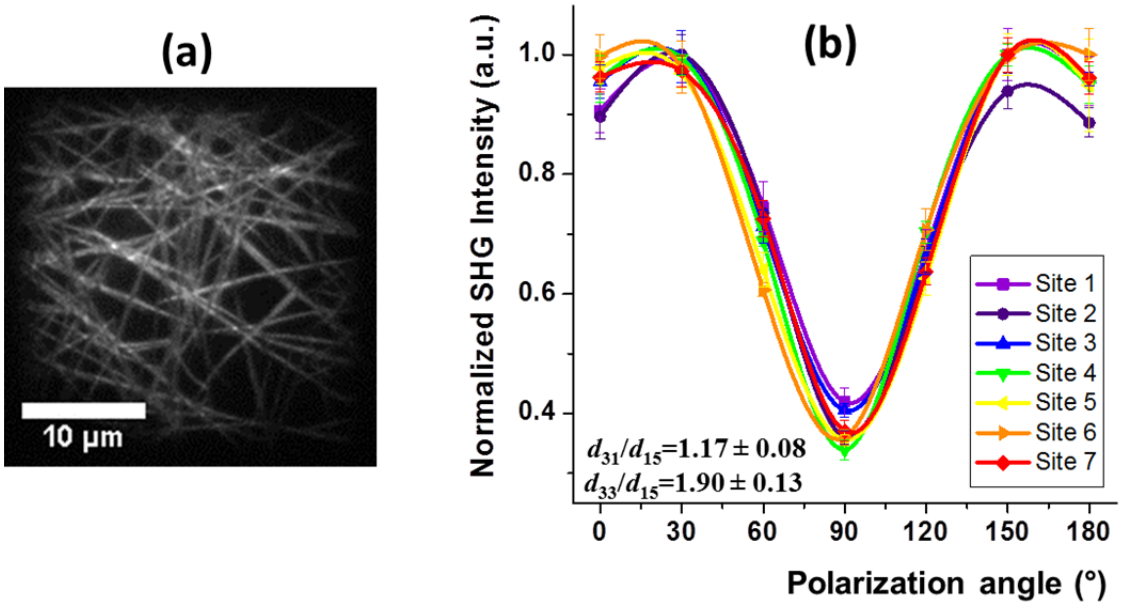


**Figure 54. (a) SHG image of type I collagen scaffold. (b) Normalized plots of SHG intensity as a function of polarization angle for 7 random fibers from (a).**

### 4.4 Generalizing $\chi^2$-SHG From Hexagonal C6 to Trigonal 3m Class Symmetry

When the collagen fibers undergo damage or change due to disease, it is more appropriate to model collagen fibers as possessing trigonal symmetry (*3m*) instead of the conventionally used hexagonal symmetry (*C6*) [158]. This hypothesis will be proved later in the section 4.5.1.2, and we also prove that it leads to a more sensitive analysis. Therefore, for a class *3m* material, the *d* matrix is given by [62]

$$\begin{bmatrix} 0 & 0 & 0 & 0 & d_{15} & -d_{22} \\ -d_{22} & d_{22} & 0 & d_{15} & 0 & 0 \\ d_{31} & d_{31} & d_{33} & 0 & 0 & 0 \end{bmatrix}, \tag{51}$$

where $d_{15}$, $d_{22}$, $d_{31}$, and $d_{33}$ are the non-zero elements. Here, the components of the polarization density are given as

$$\begin{aligned} P_x(2\omega) &= 2d_{15}E_x(\omega)E_z(\omega) - 2d_{22}E_y(\omega)E_x(\omega) \\ P_y(2\omega) &= d_{22}\left(-E_x{}^2(\omega) + E_y{}^2(\omega)\right) + 2d_{15}E_z(\omega)E_y(\omega) \\ P_z(2\omega) &= d_{31}\left(E_x{}^2(\omega) + E_y{}^2(\omega)\right) + d_{33}E_z{}^2(\omega)\ . \end{aligned} \tag{52}$$

We assume the same geometry of collagen fiber with respect to the applied field as shown in Fig. 52, for which $E_x(\omega)$ is ~ 0, $E_y(\omega) = E \sin\alpha$, and $E_z(\omega) = E \cos\alpha$.. We now obtain the emitted SHG intensity to be

$$I(2\omega) \sim \left[\left(d_{22}\sin^2\alpha + d_{15}\sin 2\alpha\right)^2 + \left(d_{31}\sin^2\alpha + d_{33}\cos^2\alpha\right)^2\right]. \tag{53}$$

This is now the final expression assuming trigonal symmetry, and here we calculate the values of the tensor coefficients $d_{15}$, $d_{22}$, $d_{31}$, and $d_{33}$, to within a constant when fit with the experimental plot of the polarization spectrum.

Figure 55a shows three typical normalized plots of the polarization spectrum that can be obtained from Eq. 53 assuming appropriate values of tensor elements. Panels (i) and (ii) in Fig. 55 (a) show polarization spectra for nonzero values of $d_{22}$, which exhibit noticeable asymmetry about 90°. Larger positive values of $d_{22}$ produces the pattern in (i), while larger negative values produces that shown in (ii); values of $d_{22}$ close to zero yield the typical spectral shape shown in (iii). Note that if collagen fiber is assumed to possess cylindrical crystal class (*C6*) symmetry, which is typically assumed, we obtain the spectrum shown in Fig. 55b, which is the same as that of panel (iii) in 55a. It is clear then that class *3m* is a more general symmetry class of which cylindrical symmetry is a special case.

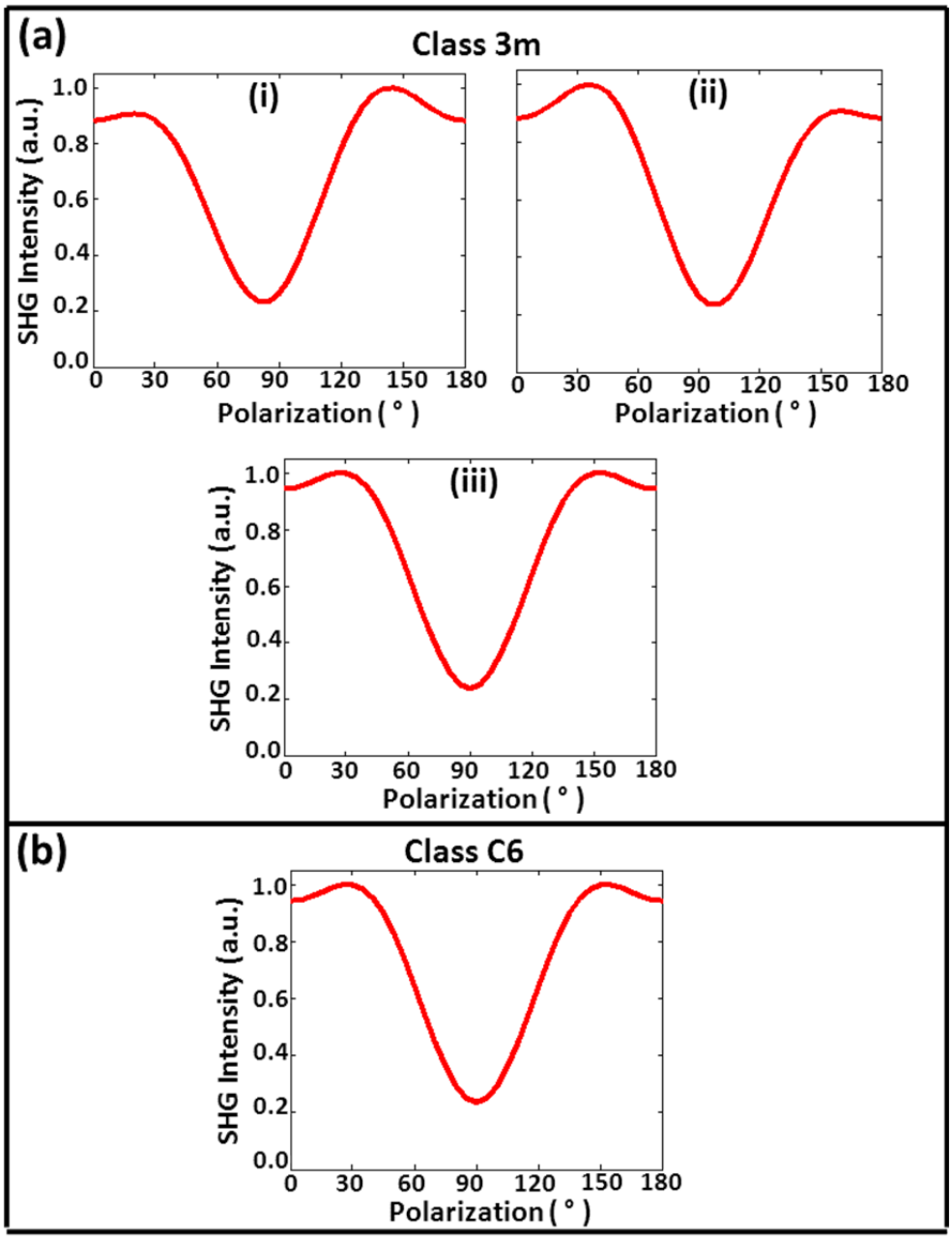


**Figure 55. Simulated plots of normalized SHG intensity as a function of polarization angle (polarization spectrum) for collagen fibers possessing a) trigonal *3m* and b) cylindrical *C6* crystal class symmetry.**

## 4.5 Results and Discussion

### 4.5.1 Applications to biological problems

In this section, we utilize $\chi^2$-SHG imaging to prove its potential as a valuable diagnostic tool for real-world biological problems either for understanding the structure of collagen fibers in different tissues or to monitor changes in collagen fibers due to damage from disease or injury.

#### *4.5.1.1 Investigation of collagen fiber organization in cornea and sclera using $\chi^2$-SHG imaging*

In this section, $\chi^2$-SHG imaging is applied to quantify differences in collagen fiber organization between porcine cornea and sclera. This section reports only the results obtained from $\chi^2$-SHG for cornea and sclera. In the discussion chapter (Chapter 5), we discuss the overall results from the two techniques, and investigate the properties of transparency and opacity for cornea and sclera, respectively.

##### *4.5.1.1.1 Results and discussion*

$\chi^2$-SHG takes advantage of the coherent nature of SHG and utilizes polarization to extract the second-order susceptibility which provides information on molecular organization. Figure 56a and 56b show the plots of normalized SHG intensity as a function of polarization angle for sclera and cornea, respectively. These plots are fitted with an equation that describes SHG intensity in terms of the elements of the second-order susceptibility matrix, and in particular, the ratios, $d_{31}/d_{15}$ and $d_{33}/d_{15}$ are determined for sclera and cornea. The calculated values of $d_{31}/d_{15}$, and $d_{33}/d_{15}$, for sclera are 1.32±0.23 and 1.84±0.32, respectively. In addition, for cornea, these values are found to be 1.29±0.14 and 1.97±0.23, respectively. These values are statistically insignificant (at a p-value of 0.05) between the two.

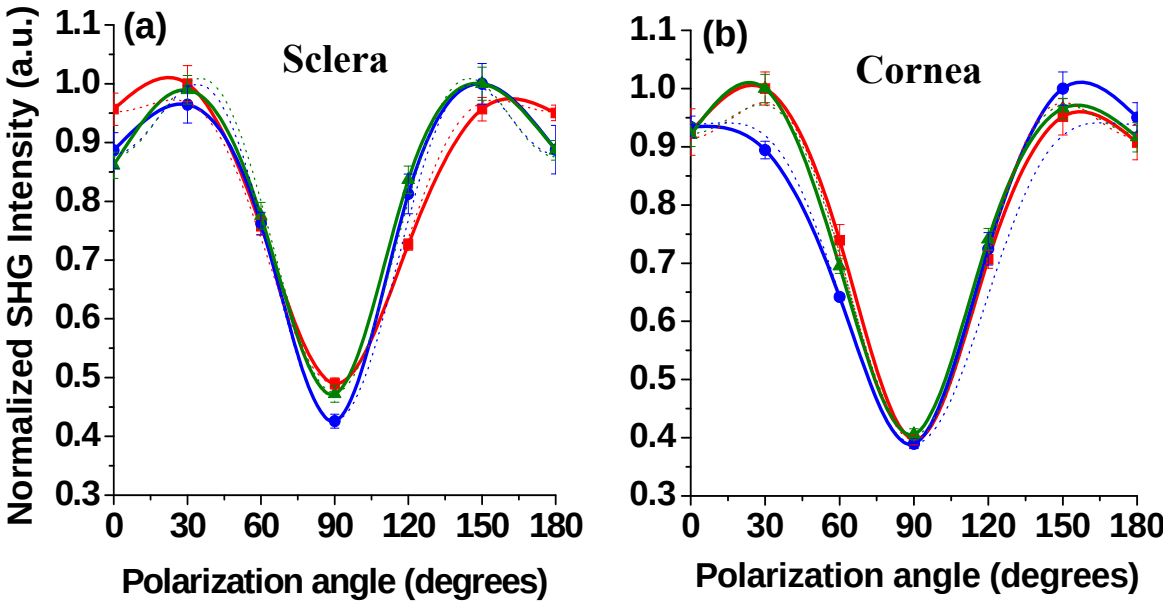


**Figure 56. Normalized SHG intensity as a function of polarization angle for (a) sclera and (b) cornea.**

*4.5.1.2 Breast cancer study: Quantifying stromal collagen structure in breast cancer biopsies using $\chi^2$-SHG*

In this section, $\chi^2$-SHG imaging is used to assess collagen fiber organization in several breast tissue conditions — normal, hyperplastic, dysplastic, and malignant.

*4.5.1.2.1 Introduction*

$\chi^2$-SHG has been used previously in two reports for breast cancer detection, but with mixed results [159, 160]. In one study, the researchers used $\chi^2$ to estimate the orientation of collagen molecules in normal and cancerous tissues. Unfortunately, to their surprise, they did not observe any statistical differences between the two [159]. In the same year, another group reported the value of a particular matrix element in $\chi^2$, i.e., $d_{22}$ for normal and breast cancer tissues. $d_{22}$ was normalized with respect to a nonlinear crystal (lithium niobate) and they found significant differences between the two [160]. Here, we sought to examine the

potential of SHG imaging for analysis of breast tissue by building on these studies in several significant ways. As a prelude to eventual biomedical research and clinical translation, an overarching consideration in our study is the compatibility with current tissue examination protocols. While the developed methods are sought to be generally applicable to cancer research, we considered the aforementioned four breast tissue conditions as a relevant test case. Furthermore, as mentioned before, we also assume a more general crystal class symmetry for collagen, i.e., trigonal symmetry (*3m*), and calculate all the (normalized) tensor elements for the various conditions. Finally, we also determine the unique combination of normalized tensor elements that are most sensitive for characterizing the four tissue conditions.

*4.5.1.2.2 Experiment*

The same breast tissue microarray mentioned in section 3.4.3.4.2.1 is used for the $\chi^2$-SHG imaging, and the experimental set up is already detailed in section 3.3.2. The average power is < 10 mW. The forward-scattered SHG intensity is recorded as the incident polarization is varied between 0° and 180°. We find it sufficient to choose a step size of 30° to produce accurate measures of the *d* ratios. We chose to analyze 11 cores of normal, 10 cores of hyperplastic, 10 cores of dysplastic, and 11 cores of malignant tissue. From each core, regions (~ 5 μm x 5 μm) containing a collagen fiber were randomly selected for analysis from one of five sectors (top, left, bottom, right, and center). In total, the respective sample size for normal, hyperplastic, dysplastic, and malignant tissue are 48, 48, 42, and 46. As mentioned before, all images are acquired from the surface of the sample to avoid birefringence and diattenuation.

*4.5.1.2.3 Results and discussion*

While the FT-SHG analysis provided an understanding of multiple collagen fibers' organization at the microscopic level, here we also sought to investigate average changes in individual collagen fibers that influence their microscopic organization through $\chi^2$-SHG. We apply $\chi^2$-SHG to calculate the normalized tensor elements of the second-order susceptibility

matrix corresponding to collagen fibers. Figure 57 shows example polarization spectra for various conditions. On average, it is observed that collagen fibers in normal tissue (Fig. 57a) show prominent shoulders at ~ 30° and 150° and are relatively symmetric about 90°. In contrast, many fibers in malignant tissue exhibit a polarization spectrum with little or no shoulders and an asymmetry about 90° (Fig. 57d). Collagen fibers in hyperplastic and dysplastic tissues show trends that lie between normal and malignant tissues. These trends are likely a consequence of both the remodeling of collagen as well as physical forces in tissue.

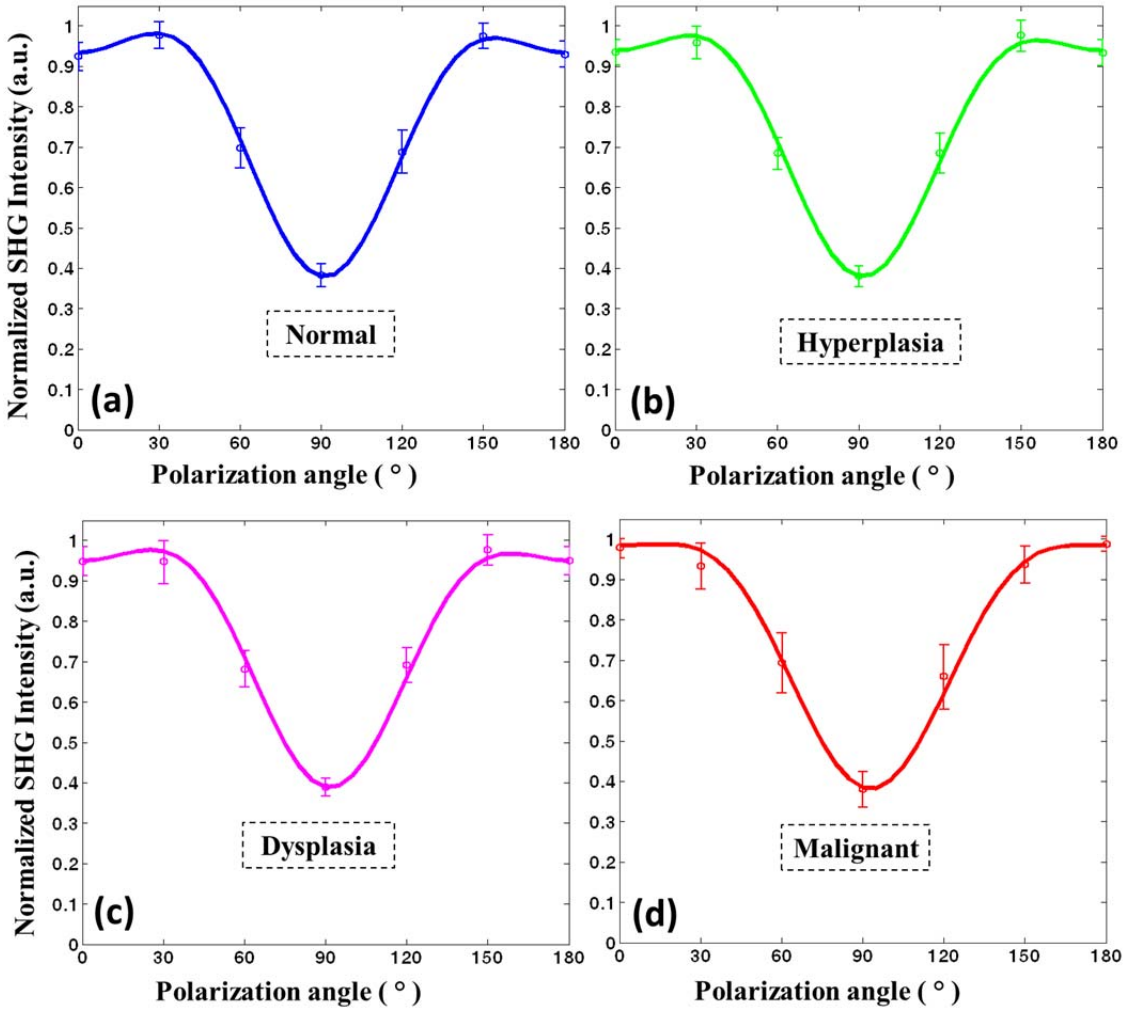


**Figure 57. Normalized SHG intensity as a function of polarization angle (or polarization spectrum) for a) normal, b) hyperplastic, c) dysplastic, and d) malignant breast tissue.**

Note that Eq. (53) is a proportional equation and as such we can only obtain normalized values of the tensor coefficients. For example, when normalized by $d_{15}$, we can obtain $d_{22}/d_{15}$, $d_{31}/d_{15}$ and $d_{33}/d_{15}$. Note that, however, the choice of normalization is not arbitrary. We want to find the appropriate combination of ratios of tensor elements that contain the least amount of redundancy. For example, if $d_{15}$ is changing with each tissue condition, then other elements normalized by it ($d_{22}/d_{15}$, $d_{31}/d_{15}$ and $d_{33}/d_{15}$) will all show the same change, thereby leading to redundancy. To minimize this, we consider all combinations of normalization (i.e., $d_{15}$, $d_{31}$, $d_{33}$, and $d_{22}$), and the resulting equations are fit to the experimental plot of polarization spectrum for all tissue conditions. We find that in the case of breast cancer, both $d_{31}$ and $d_{33}$ provide the least redundancy; therefore, we choose to normalize the tensor elements by $d_{31}$. The final expression for the SHG intensity as a function of polarization angle is

$$I(2\omega) \sim \left[ \left( \frac{d_{22}}{d_{31}} \sin^2\alpha + \frac{d_{15}}{d_{31}} \sin 2\alpha \right)^2 + \left( \sin^2\alpha + \frac{d_{33}}{d_{31}} \cos^2\alpha \right)^2 \right], \tag{54}$$

where the ratios $d_{22}/d_{31}$, $d_{15}/d_{31}$ and $d_{33}/d_{31}$ are calculated and used as metrics to differentiate between breast tissue conditions.

After fitting the experimental plots of the polarization spectrum using Eq. 54, the $d$ ratios, $d_{15}/d_{31}$, $d_{33}/d_{31}$ and $d_{22}/d_{31}$ (absolute value) are calculated and plots are shown in Fig. 58. The average value of the ratio $d_{15}/d_{31}$ ranges from 0.843 for normal to 0.728 for malignant tissue. Moreover, the standard deviation increases from a value of 0.064 for normal to 0.122 for malignant tissue. Similarly, differences are observed for $d_{22}/d_{31}$ with a mean value of 0.052 for normal and 0.116 for malignant tissue. Again, the standard deviation is observed to be higher for abnormal conditions, likely indicating greater heterogeneity. Interestingly, the ratio $d_{33}/d_{31}$ remains relatively constant across all conditions. These ratios can potentially function as metrics of pathology. There is, however, significant variance indicating the response and heterogeneity of stromal remodeling.

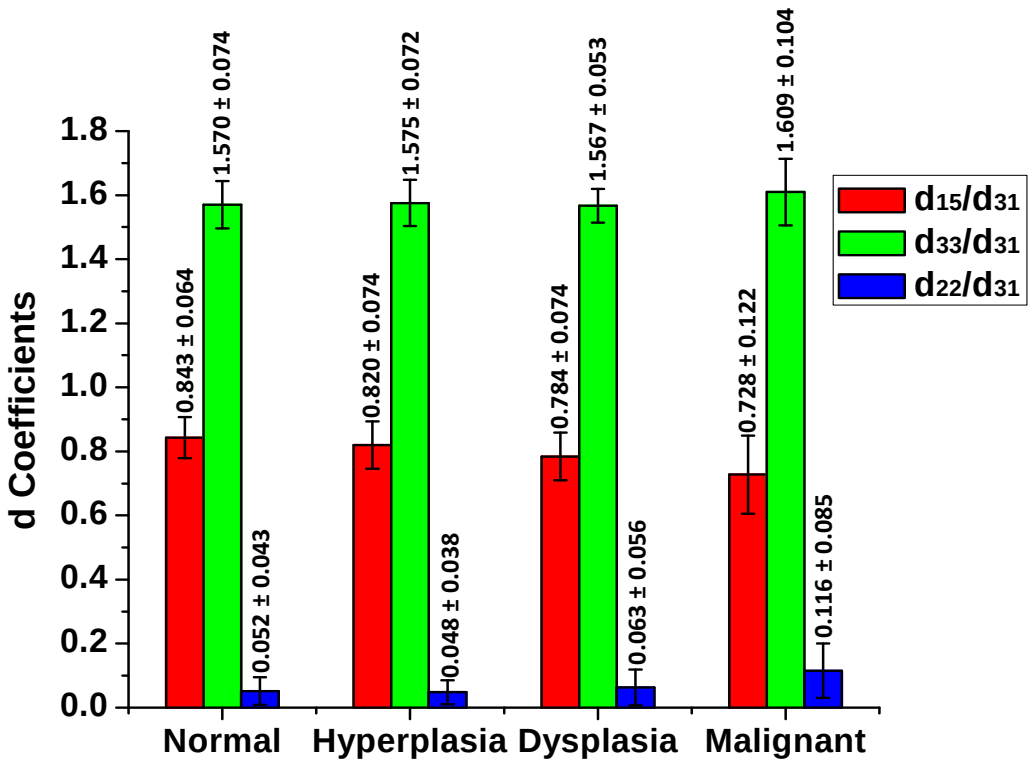


**Figure 58. Bar plot of the tensor elements ($d_{15}/d_{31}$, $d_{33}/d_{31}$, $d_{22}/d_{31}$) for normal, hyperplastic, dysplastic, and malignant tissues.**

In order to test if the *d* ratios can be used as a metric for differentiating various breast pathologies, we performed statistical comparison tests assuming the values within the core to be dependent and the values across the cores to be independent. Repeated measures of ANOVA with between-subject factors were performed using OriginPro 8 and SAS. A condition for this analysis is that the distribution of values of *d* ratios must be normal. This is satisfied for the ratios $d_{15}/d_{31}$ and $d_{22}/d_{31}$, but not with $d_{33}/d_{31}$. However, for this case, we find that the log of $d_{33}/d_{31}$ also shows a normal distribution, thereby permitting us to apply the above analysis. The results of the comparison are shown in Table 4. Using $d_{15}/d_{31}$ and a p-value of 0.05, we find that there seems to be the potential to differentiate between normal and dysplasia, normal and malignant, hyperplasia and malignant, and dysplasia and malignant. However, differentiation of hyperplasia from either normal or dysplasia could not be established. Interestingly, we did not observe any statistical differences between ductal and lobular carcinoma-associated stroma.

**Table 4. Comparison tests between breast tissue conditions performed at a p-value of 0.05, which corresponds to 95% confidence level. M.D. is the mean difference between the different tissue conditions.**

| | $d_{15}/d_{31}$ (ANOVA) | | | $d_{33}/d_{31}$ (ANOVA) | | | $d_{22}/d_{31}$ (K.S. Test) | | |
|---|---|---|---|---|---|---|---|---|---|
| **Groups** | **M.D.** | **p-value** | **Significant?** | **M.D.** | **p-value** | **Significant?** | **M.D.** | **p-value** | **Significant?** |
| **Normal vs. Hyperplasia** | 0.023 | 0.3259 | No | -0.005 | 0.8085 | No | -0.011 | 0.9845 | No |
| **Normal vs. Dysplasia** | 0.059 | 0.0170 | Yes | 0.003 | 0.9122 | No | -0.012 | 0.1688 | No |
| **Normal vs. Malignant** | 0.115 | <0.0001 | Yes | -0.040 | 0.0438 | Yes | -0.064 | 0.0002 | Yes |
| **Hyperplasia vs. Dysplasia** | 0.036 | 0.1410 | No | 0.008 | 0.7304 | No | -0.001 | 0.1641 | No |
| **Hyperplasia vs. Malignant** | 0.092 | 0.0003 | Yes | -0.034 | 0.0762 | No | -0.053 | 0.0002 | Yes |
| **Dysplasia vs. Malignant** | 0.056 | 0.0218 | Yes | -0.043 | 0.0395 | Yes | -0.052 | 0.0135 | Yes |

Given the variance and the range in values, at this stage, it does not appear that there is a simple feature in SHG data that characterizes breast pathology. To more accurately estimate the use of SHG imaging data for breast pathology, we sought to devise a test based on similarity to normal tissue. We defined a filter that contains the range of values of $d_{15}/d_{31}$ for normal tissue and we label the collagen fibers whose tensor values fall outside this normal range as "abnormal" collagen fibers. We then tabulated the number of abnormal collagen fibers in each tissue condition. The fractions of abnormal fibers defined in this manner are plotted for each condition in Fig. 59 and were observed to be 0.0% (by definition), 10.4%, 19.1%, and 47.8% for normal, hyperplastic, dysplastic, and malignant tissue, respectively. It is evident that the numbers of abnormal fibers are different for different pathologies. It is also interesting to observe that about 52.2% of the collagen fibers in malignant tissue are normal fibers with this definition.

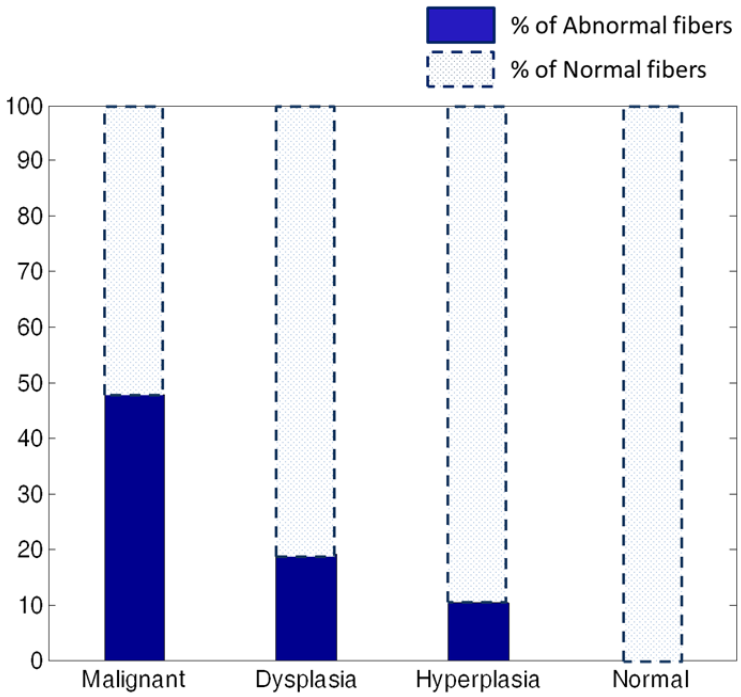


**Figure 59. Percentage of abnormal collagen fibers as a function of breast pathology.**

As observed from the measurements above, normal breast tissue contains collagen fibers whose $d_{15}/d_{31}$ value lies in the range of 0.843 ± 0.064, and $d_{33}/d_{31}$ within the range 1.570 ± 0.074. These values are close to reported values for type I collagen [28]. The values of $d_{22}/d_{31}$ for normal tissue lie close to zero (0.052 ± 0.043) indicating that the assumption of cylindrical symmetry is valid for normal tissue. This symmetry condition, however, does not seem to hold for malignant tissues that contain abnormal fibers. Since malignant tissues also contain normal tissue-like fibers (~ 50% of the total fibers), the average differentiation appears to be smaller. This is also a likely reason for the large standard deviation associated with malignant tissues. Hence, we removed the contribution of normal fibers from malignant tissue and considered only abnormal fibers, which provided values of $d_{15}/d_{31}$ = 0.646 ± 0.122, $d_{33}/d_{31}$ = 1.603 ± 0.123, and $d_{22}/d_{31}$ = 0.117 ± 0.087. Malignant tissue contains fibers that have comparatively smaller $d_{15}/d_{31}$ and larger $d_{22}/d_{31}$ values. Larger values of $d_{22}/d_{31}$ manifest as asymmetry about 90º, and are an indication that trigonal symmetry is a more appropriate description for abnormal fibers.

### 4.5.2 Sensitivity to $\chi^2$-SHG to structure

We know that the $\chi^2$-SHG is sensitive to molecular changes in the collagen fibers, which could be either changes in composition or molecular conformation, especially the helical angle of the amino acids [28, 161]. Here, we investigate whether $\chi^2$-SHG is also sensitive to changes in fiber diameter. For this, we fabricated type I collagen scaffolds in our lab. The sample preparation for collagen scaffolds is provided in Appendix A. By carefully controlling the concentration of collagen molecules, pH, and temperature of curing, collagen fiber scaffolds can be prepared with varying fiber diameters in the range ~100 nm - 800 nm. We were able to fabricate collagen fibers up to 720 nm. The smallest fiber diameter we could resolve is ~ 320 nm for a 0.6 NA illumination air objective and an oil-immersion collection objective. Thus, our range for $\chi^2$-SHG measurements is from 320 nm to 720 nm. Note that here we can consider the *C6* symmetry since the collagen fibers in the scaffolds are neither damaged nor diseased. This reduces the redundancy from $d_{22}/d_{31}$, which is close to zero in this case.

Figure 60 shows the measured values of the *d* elements, $d_{15}/d_{31}$ and $d_{33}/d_{31}$, as a function of fiber diameter from 320 nm to 720 nm. Three measurements from different fibers were taken. It is observed that $d_{15}/d_{31}$ stays in the range ~0.85 to 0.91, and $d_{15}/d_{31}$ in the range ~1.51 to 1.55 throughout the fiber diameter range. The values across the different fiber diameters are also statistically insignificant at a p-value of 0.05.

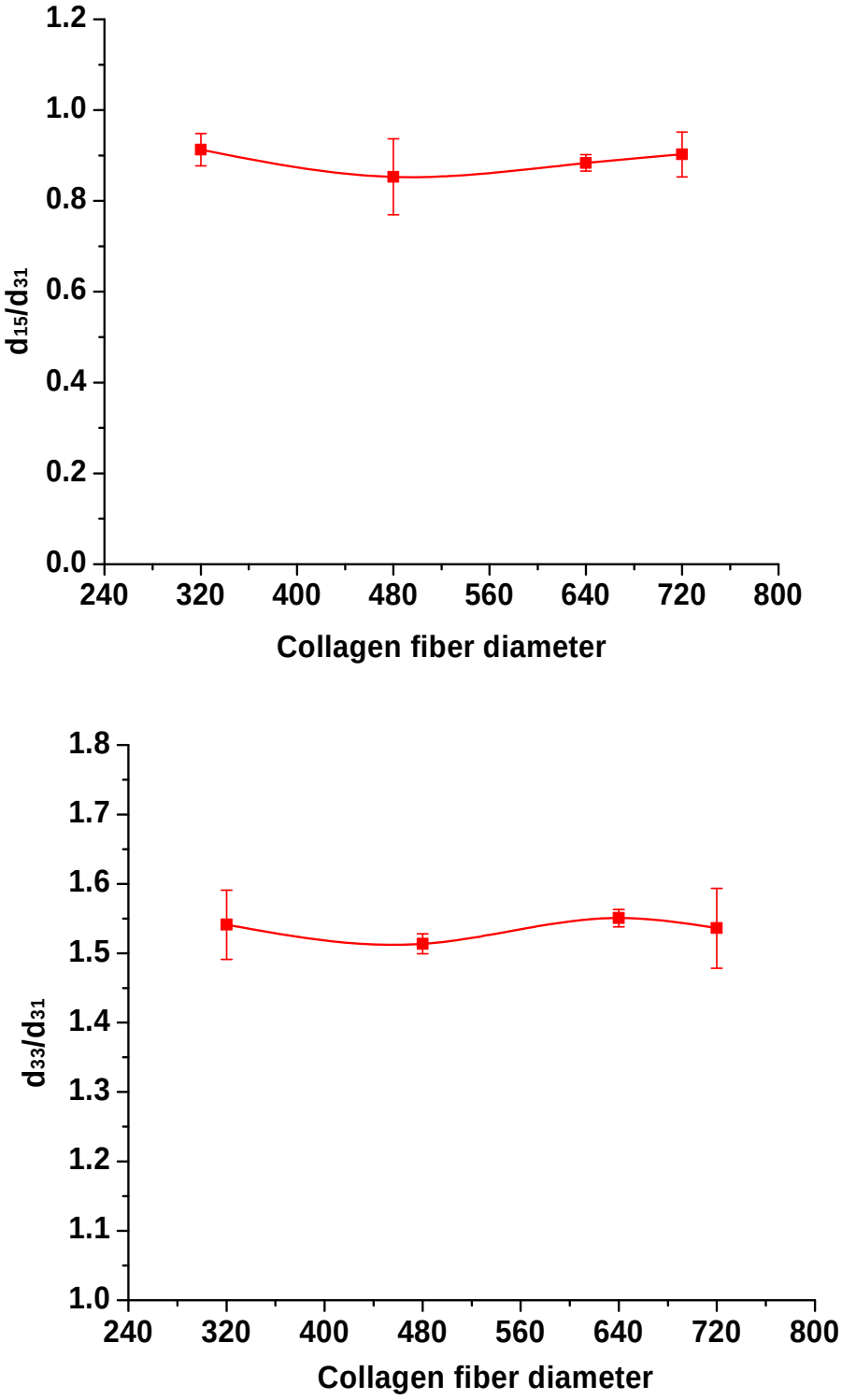


**Figure 60. Measured values of *d* elements, $d_{15}/d_{31}$ and $d_{33}/d_{31}$, as a function of fiber diameter.**

### 4.5.3 Extension of $\chi^2$-SHG to fibers with curvature to generate $\chi^2$-image maps

In this section, we discuss a method of extending $\chi^2$-SHG to fibers with curvature. In order to calculate the second-order susceptibility matrix, there is an experimental constraint that the collagen fiber under interest should be straight (as opposed to being curved) as shown in Fig. 61 so that the polarization of applied field relative to the fiber can be accurately calculated. However, most biological tissues contain collagen fibers that are not necessarily straight; they may have small radii of curvature (i.e., largely curved). In order to calculate the *d* elements for such tissues, it is essential to extend $\chi^2$-SHG to fibers with curvature. Its main advantage is that one can generate image maps in terms of $\chi^2$ instead of raw SHG intensity as shown schematically in Fig. 61. The spatial variations in *d* elements would provide additional information regarding the sample. For example, in breast cancer tissues, it will be useful to see how the fibers convert locally from normal to malignant as we move towards the region containing cancerous cells.

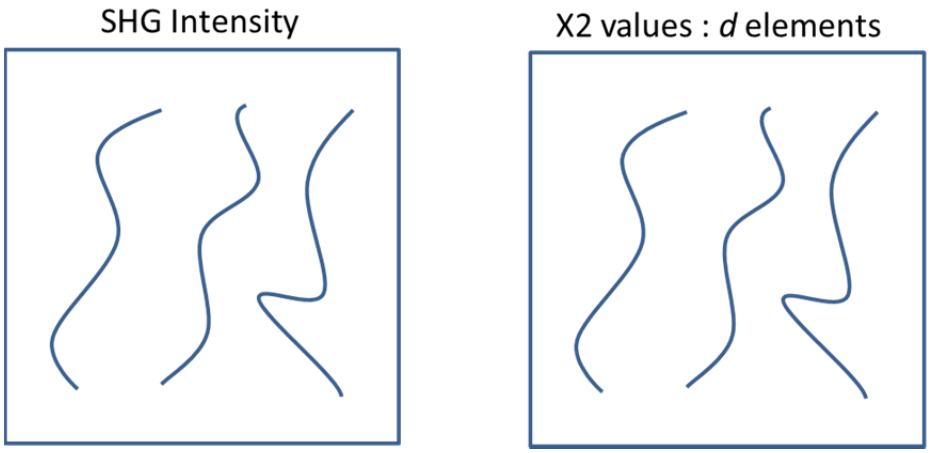


**Figure 61. A simple schematic showing a (a) conventional SHG image and (b) $\chi^2$-image map in terms of *d* elements.**

#### *4.5.3.1 Challenges*

There are a few challenges associated with this and they are listed below.

1. Most tissues are heterogeneous, which means that the neighboring fibers can falsify the estimate of *d* elements for a particular collagen fiber.

2. The accuracy of calculated *d* elements depends on the signal-to-ratio (SNR) of the SHG intensity within the region of interest. However, for any real biological sample, there always exist regions with low SNR. These noisy regions give inaccurate values.
3. Saturation of SHG intensity within a region of interest could also lead to inaccurate values since the plot of polarization spectrum can no longer look like that shown in Fig. 57a but instead looks like a horizontal line of magnitude 1 for all polarization angles.
4. Drift in the image during image acquisition due to the relative movement between the sample and objectives can also be a problem. Even a drift of 1-2 pixels can lead to erroneous values. The drift could be due to the heavy weight of the upper microscope which leads to lowering the objective slowly over time due to gravity, air currents, or thermal expansion of the components in the microscope or optical train.

#### *4.5.3.2 Method*

First, a series of SHG images are obtained at polarization angles 0º to 180º (step size of 5º-10º). We first approximate a curved fiber as several short straight fibers of different orientations. This can be done by reducing the sub-image size down to a side-length of just 8 or 16 pixels. This size can also account for the drift and as long as it stays within 3-4 pixels of drift, we can estimate the *d* elements fairly accurately. It also allows for accurate estimation of the preferred orientation as mentioned in section 3.2.1. Smaller size of sub-image up to a certain degree also avoids the influence of neighboring fibers so that the polarization spectrum is from an individual fiber. Then, the preferred orientation is calculated for each sub-image using the radial integration or image gradient method. The angle between the fiber segment and incident polarization angle (polarization offset) is calculated. Finer polarization angles are needed; i.e., a step size of at least 5º-10º ensures that the error in polarization offset stays < 5-10º.

We also define a few thresholds to increase accuracy of the estimate for *d* elements. A dark threshold is set to neglect the regions that contain no collagen fiber or fibers with low SNR, which are usually the extremely noisy regions in the image. We also define thresholds, *thr_max* and *thr_mean* which act as secondary filters that can be tuned to further neglect the

regions based on maximum SHG intensity and mean SHG intensity within the sub-image, respectively. Another threshold called *thr_std* makes sure that there is adequate image contrast. This especially neglects blurry regions caused by high scattering or erosion from sample cutting artifacts. A simple algorithm also searches for sub-images containing saturated pixels, and they are discarded from the analysis.

The classification of isotropic vs. anisotropic regions is performed through the spread in the histogram of calculated orientation. If the spread is larger than 40º, the sub-image is considered an isotropic region. Finally, in order to account for variations in the calculation of orientation for noisy regions, the calculated orientation is set as the initial guess for fitting with 15º bounds. Now the corrected polarization spectra for the non-neglected sub-images are used to calculate the *d* elements and thus generate $\chi^2$-image maps.

*4.5.3.3 Results*

A series of SHG images of porcine sclera are obtained at polarization angles 0º to 180º at a step size of 10º. Moreover, 5 images per polarization angle are collected and averaged. Shown in Fig. 62a is an SHG image of a region of interest in sclera overlaid with the orientation sub-grid obtained at 0º polarization angle. Each sub-image is of the size 8x8 pixels. The isotropic and saturated regions are labeled in pink and blue, respectively. The regions labeled in green are those that are either extremely noisy or that were neglected from the analysis based on the filter established from the thresholds. Here, *thr_max*, *thr_mean*, and *thr_std* are chosen to be 0.35, 0.35, and 0.1, respectively. The 17 anisotropic regions that were not neglected are shown with their corresponding preferred orientation, *k*, *a1* and *a2* values, where $a1 = d_{31}/d_{15}$ and $a2 = d_{33}/d_{15}$. Note that again, here, we can consider the *C6* symmetry since the collagen fibers in sclera are neither damaged nor diseased. Figures 62b, 62c, and 62d show the corresponding maps of *k*, *a1*, and *a2*, which provide useful information on the spatial variations of these metrics. It is even possible to calculate the *d* elements on a particular region of an individual collagen fiber. The histograms of the values of *k*, *a1*, and *a2*, are also shown in Fig. 63a, 63b and 63c. For *k*, we observe the mean and standard deviation to be 0.27 and 0.04, for a1, it is 1.23 and 0.15, and for a2, it is 1.88 and 0.20 units.

We observe that the stronger the filter requirements, the less the variations in the estimated values. In other words, there is always a tradeoff between accuracy and number of non-neglected sub-images for which the *d* elements need to be calculated. Shown in Fig. 64 is the same analysis as in Fig. 62; however, the parameters are chosen such that there are now more regions (54). Here, *thr_max*, *thr_mean*, and *thr_std* are chosen to be 0.15, 0.15, and 0.05, respectively. As you can see, the variations are larger for all the calculated parameters, as evident from Fig. 64a, 64b, 64c, and 64d, and moreover, the image contains some outliers. The standard deviations for *k*, *a1*, and *a2*, are now 0.06, 0.24, and 0.31, respectively as shown in the histograms plot in Fig. 65. Due to the presence of outliers mostly larger than the usual range, the mean values also tend to be higher with mean values of 0.24, 1.37, and 2.00 for *k*, *a1*, *a2*, respectively. Thus, the thresholds need to be optimized for adequate accuracy.

The whole data collection has been automated using a motorized rotation stage and *autohotkey* program. The analysis has been also completely automated. For example, a simple mouse click collects 180 images at polarization angles 0º to 180º and 5 images per polarization angle. The settings can be changed according to the need. The data collection takes ~ 5 minutes, which is limited by the SNR of the image and galvo's scanning speed. A Matlab program then runs on the specified folder containing the images and produces the $\chi^2$-image maps and histogram plots. The run time for the analysis is < 5 seconds. It is written to facilitate subsequent users and even biologists so they can calculate $\chi^2$-image maps for their biological samples, without the need to know the physics of SHG or the method of analysis.

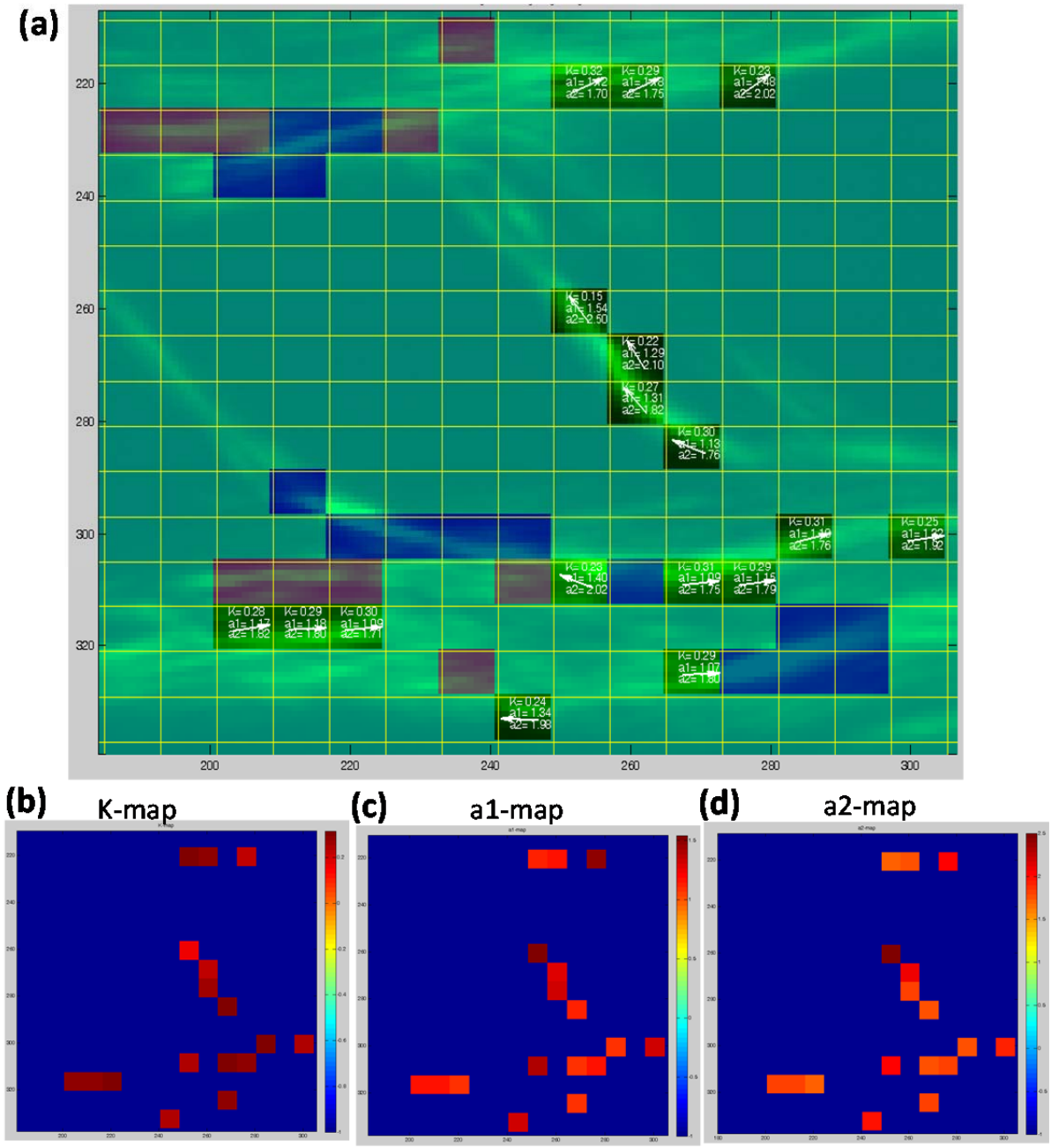


**Figure 62. (a) SHG image of region of interest from sclera overlaid with orientation sub-grid, and corresponding values of k, a1, and a2, where a1 = $d_{31}/d_{15}$ and a2 = $d_{33}/d_{15}$. Corresponding (b) K-map, (c) a1 and (d) a2 maps of the sample shown in (a). Thresholds: thr_max= 0.35, thr_mean= 0.35, and thr_std = 0.1.**

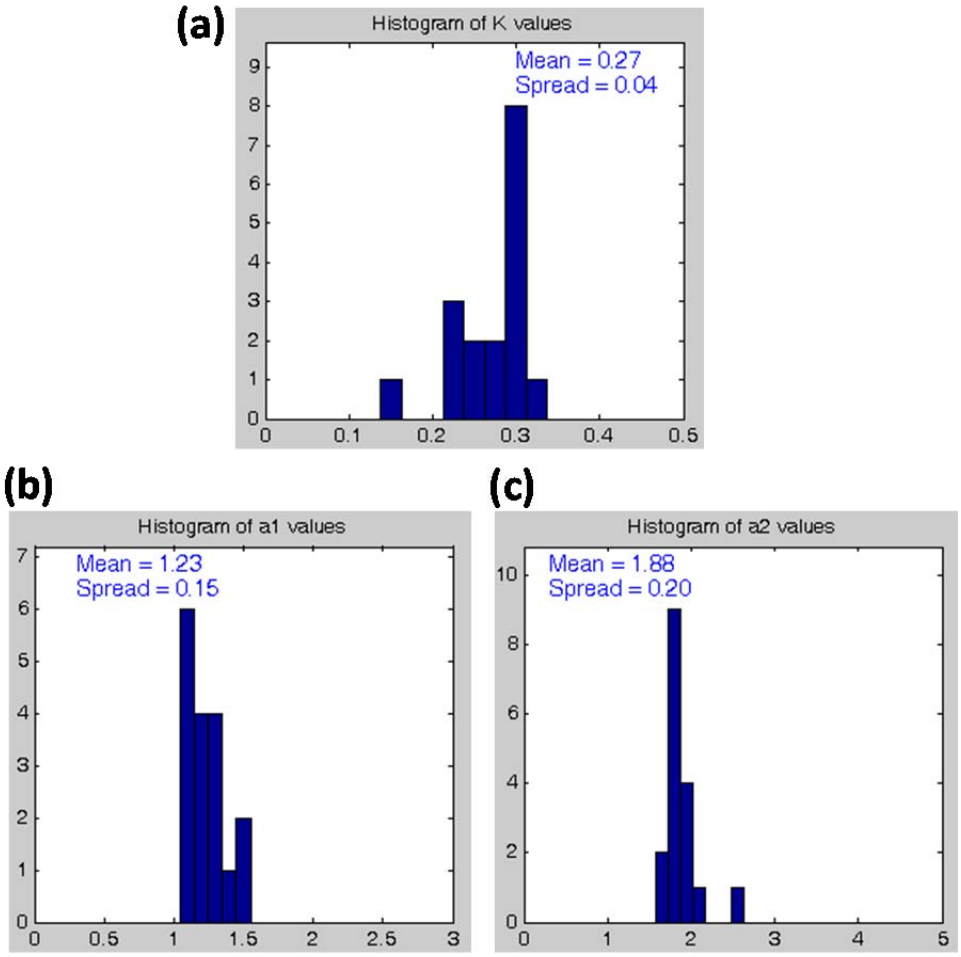


**Figure 63. Histograms of the values of (a) k, (b) a1 and (c) a2 for the sample shown in Fig. 62a.**

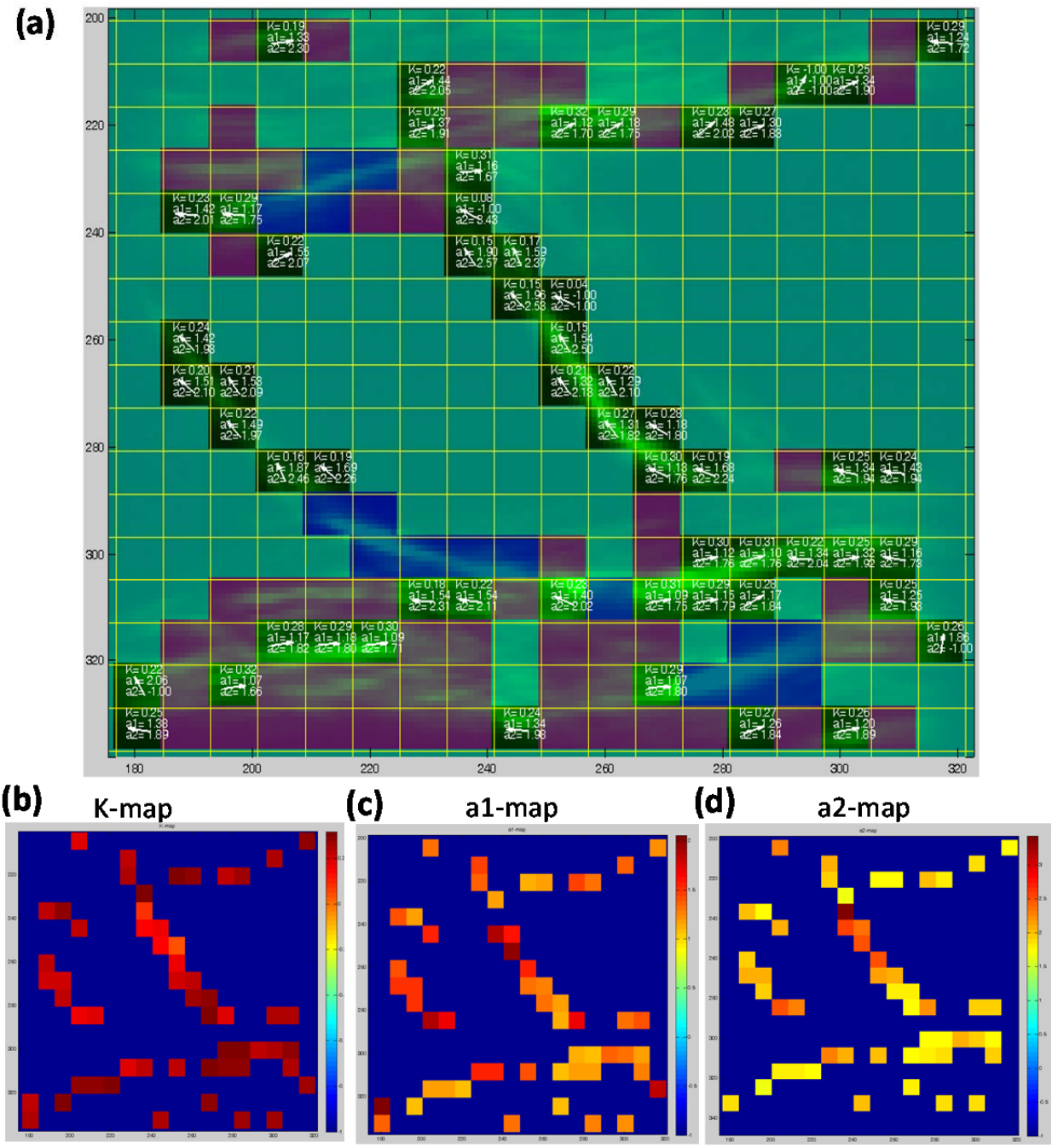


**Figure 64. (a) SHG image of region of interest from sclera overlaid with orientation sub-grid, and corresponding values of k, a1, and a2, where a1 = $d_{31}/d_{15}$ and a2 = $d_{33}/d_{15}$. Corresponding (b) K-map, (c) a1 and (d) a2 maps of the sample shown in (a). Thresholds: thr_max= 0.15, thr_mean= 0.15, and thr_std = 0.05.**

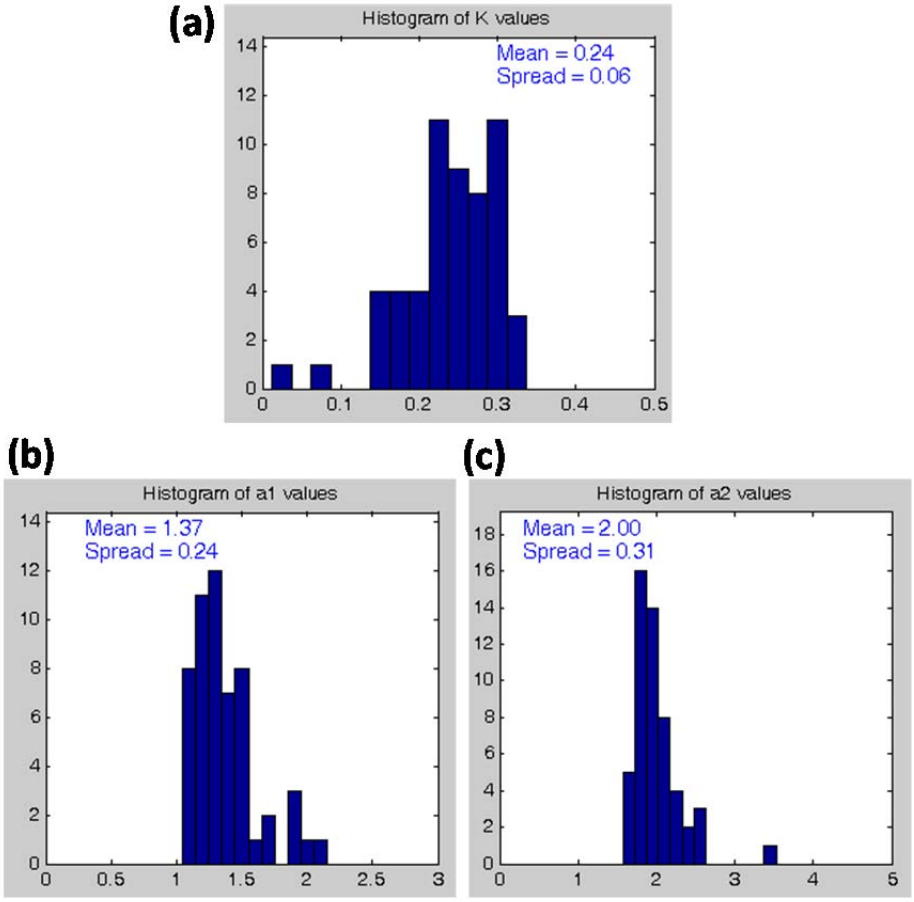


**Figure 65. Histograms of the values of (a) k, (b) a1 and (c) a2 for the sample shown in Fig. 64a.**

# CHAPTER 5: DISCUSSION, CONCLUSION AND FUTURE WORK

In the previous chapters on FT-SHG and $\chi^2$-SHG, we discussed the methodology and results obtained from each technique individually. In this chapter, we discuss the results from the two techniques as a whole as it pertains to solving the biological problem and what we understand holistically through the combined technique. Therefore, we discuss the two problems that were studied using the combined technique approach: (1) quantifying collagen fiber organization in cornea and sclera, and (2) assessment of collagen fiber structure for breast tissue biopsies.

We also discuss the conclusions that we have gathered from the application of the two techniques to several biological problems. Finally, the future work for the two techniques is discussed.

## 5.1 Discussion for Cornea and Sclera

As mentioned before, we are interested in quantifying the collagen fiber organization in cornea and sclera through the use of combined quantitative technique. Briefly, from the analysis obtained using FT-SHG imaging, we have found that the collagen fiber organization in sclera is denser (fewer dark regions), inhomogeneously oriented, and lacks axial order, contrary to that of cornea. However, $\chi^2$-SHG analysis has shown no statistically significant (p-value of 0.05) differences in the values of $d$ elements, $d_{31}/d_{15}$ and $d_{33}/d_{15}$, between cornea and sclera.

The similar values of $d$ elements between cornea and sclera are an indication that the underlying collagen structure generating SHG from both cornea and sclera are at least similar at the level of detection of SHG microscopy. Furthermore, these values are close to the previously reported values for type I collagen—lending credence to the supposition that the content of collagen is similar in both tissues. However, the difference lies in the (spatial) organization of these collagen fibers as observed from FT-SHG imaging. Cornea contains lamellae with patches of ordered and uniform diameter collagen fibers which are regularly

arranged in the axial direction (with orthogonal orientations) between successive lamella indicating axial order. These conditions should permit coherent addition of the linearly scattered light in the forward direction, which could be a major contribution to its transparency. Conversely, there are no lamellae in sclera (i.e., no axial order), and fibers are thicker, denser, have inconsistent diameters, and possess relatively inhomogeneous orientations. These factors lead to the opaque nature of the sclera (helps block stray light) and provide stiffness necessary for maintaining the shape of the eye.

### 5.2 Discussion for Breast Cancer

In previous chapters, we utilized two quantitative second-harmonic generation imaging techniques, FT-SHG and $\chi^2$-SHG, to investigate differences in stromal collagen fibers for human breast tissues from different pathologic conditions, namely normal, hyperplasia, dysplasia, and malignant. Using FT-SHG, we quantified collagen fiber organization at cellular scales. We found that the metric, A.I. ratio, was the highest for the malignant tissue and its value was, statistically, significantly different from other tissue conditions at a p-value of 0.05. Thus A.I. ratio could potentially be useful for differentiating malignant from other tissue conditions. We also observed significant variance in the value of A.I. ratio. This natural variation probably partially accounts for the ambiguous conclusions reported in the literature on using SHG to characterize tumors. We should also caution that the tumor associated stroma is likely associated only closely with the tumor itself. The proximity of the stroma to the tumor in a small TMA sample and our careful attention to ensuring that a fair comparison is made by using well characterized spots likely explain the observed trend in our study. Significant care must be taken in transferring this result to large areas of unknown tissue. We believe that the observed characteristics of malignant tissue arise from a local stiffening of fibroblasts and the attendant stromal remodeling. The spatial extent of this remodeling and its evolution with tumor progression should be studied in detail. Here, our goal was simply to develop a tool that can potentially examine these effects. Hence, we did not pursue a detailed study of stromal remodeling indicative of tumor progression.

Alternatively, $\chi^2$-SHG was used to infer structural changes in collagen at the molecular scale through the calculation of the normalized tensor elements of the second-order susceptibility, i.e., $d_{15}/d_{31}$, $d_{33}/d_{31}$ and $d_{22}/d_{31}$. In particular, $d_{15}/d_{31}$ showed statistical differences across breast tissue pathologies, except between hyperplasia and normal/dysplasia. We also found that trigonal symmetry (*3m*) is a more appropriate model to describe collagen fibers in malignant tissues as opposed to the conventionally used hexagonal symmetry (*C6*). Furthermore, the percentage of abnormal collagen fibers was distinctly different across the tissue conditions. In particular, about 52% of the collagen fibers in malignant tissue were normal. This means that that there are few "global" changes in tissue stroma but different regions must be carefully probed. Secondly, imaging in terms of the *d* elements is needed and averaging measurements will likely yield to confusing results. Thus, studies designed to measure changes due to cancer progression will have to carefully segment the spatial variations and understand these in the context of the tumor. While our goal here was to determine whether there is any potential of using SHG imaging to understand stromal changes in breast cancer, for future clinical translation, this issue of within sample and other variance must be examined through a larger study and location of fibers relative to the tumor.

Our observed changes in the values of the *d* ratios and symmetry are interesting, likely indicating ECM remodeling that is observed during tumor progressions [162]. Molecular changes in collagen fibers were also reported in recent biochemical studies [163, 164]: collagen present in the normal tissue is a heterotrimer consisting of two $\alpha$1(I) chains and one $\alpha$2(I) chain, while collagen found in malignant tissues are homotrimeric consisting of three $\alpha$1(I) chains. Unfortunately, resolving these changes is well below the diffraction-limit of conventional optical microscopes, but $\chi^2$-SHG allows us to detect potentially molecular-level changes optically. Matrix metalloproteinases (MMPs) are also upregulated in cancer [165] and are known to degrade type I collagen fibers. Furthermore, MMP upregulation also leads to a changed isoform of type I collagen, which does not degrade and helps impart a more aggressive phenotype to cancer cells. Hence, the tools reported in this study can lead to several other basic studies on the mechanism of cancer progression.

This unique method of targeting collagen fibers using a combination of two quantitative SHG techniques, FT-SHG and $\chi^2$-SHG imaging, seems promising for further study, especially

as a complementary technique with gold-standard histopathological diagnosis. To that end, our SHG measurements were conducted on clinically compatible slides and can be easily incorporated within present clinical work.

### 5.3 General Conclusion

This thesis reports the development of two quantitative second-harmonic generation techniques — Fourier transform-second-harmonic generation (FT-SHG) and generalized $\chi^2$-second-harmonic generation ($\chi^2$-SHG) imaging for quantifying collagen fiber organization/structure in biological tissues at the cellular and molecular scales, respectively.

FT-SHG imaging involves extracting quantitative metrics through the application of spatial Fourier analysis on the images of collagen-based tissues obtained from a SHG microscope. We defined simple metrics such as preferred orientation, maximum spatial frequency, and fiber spacing and showed how they could be used for quantification. We first quantified differences in collagen fiber organization in terms of preferred orientation and maximum spatial frequency among several porcine tissues: ear cartilage, trachea, and cornea. The ear cartilage showed consistent maximum spatial frequency and orientation. However, there are observable changes in the orientation and minimum feature size of fibers in the trachea indicating a more random organization. The analysis was also applied to investigate structural changes through a 3D image stack of the cornea.

FT-SHG imaging was also applied to quantitatively compare the information content between SHG images obtained from the forward and backward direction for three tissue types: porcine tendon, sclera, and ear cartilage. Both signal types yielded consistent information on the preferred orientation of collagen fibers. The Fourier transform of the forward and backward SHG images produces several overlapping peaks in the magnitude spectrum at various depths into the tissues. This indicates that some information present in the forward SHG images can be extracted from the backward SHG images, highlighting the potential of backward SHG microscopy for medical diagnostics.

We then show that FT-SHG imaging can be used as a valuable diagnostic tool for real-world biological problems where the structure of collagen fibers changes due to damage from disease or physical injury. In particular, we investigate the potential of FT-SHG imaging in evaluating collagenase-induced injury in horse tendons. The differences in collagen fiber organization between normal and injured tendon were quantified. Results indicate that the organization of collagen fibers is regularly oriented in normal tendons and randomly organized in injured tendons. This is further supported through the use of additional metrics, in particular, the number of dark (no/minimal signal) and isotropic (no preferred fiber orientation) regions in the images, and the ratio of forward-to-backward second-harmonic intensity. FT-SHG microscopy is also compared with the conventional polarized light microscopy and is shown to be more sensitive in assessing injured tendons than the latter.

Later, we utilized FT-SHG imaging for quantifying collagen fibers in porcine femoral cortical bone. The technique was compared with scanning electron microscopy (SEM); and the pros and cons of each were discussed. Furthermore, we quantitatively assess collagen fiber organization through an exploratory examination of bone structure as a function of age, from very young to mature bone — 1 month to 30 months. We observed that as the bone develops, there is an overall reduction in porosity, the number of osteons increases, and the collagen fibers become comparatively more organized. It is also observed that the variations in structure across the whole cross-section of the bone increase with age. Finally the extension of FT-SHG to 3d is proposed. Some initial work and future directions are provided.

The second technique, $\chi^2$-SHG imaging, takes advantage of the coherent nature of SHG and utilizes polarization to extract the second-order susceptibility which provides information on molecular organization. We used $\chi^2$-SHG in combination with FT-SHG imaging to investigate a couple of biological problems. First, we quantified differences in collagen fiber organization between cornea and sclera of the eye in order to investigate their properties of transparency and opacity, respectively. From $\chi^2$-SHG imaging, we found no statistically significant (p-value of 0.05) differences in the values of *d* elements between cornea and sclera, indicating that the underlying collagen structure generating SHG from the two are similar at the level of detection of SHG microscopy. However, the difference lies in the spatial organization of these collagen fibers as observed from FT-SHG imaging. We found

that cornea contains lamellae with patches of ordered and uniform diameter collagen fibers with axial order, which could be reason for its transparent behavior. Conversely, there are no lamellae in sclera (i.e., no axial order), and fibers are thicker, denser, have inconsistent diameters, and possess relatively inhomogeneous orientations, leading to its opaque nature.

We also utilized the two techniques to investigate differences in stromal collagen fibers for human breast tissues from different pathologic conditions, namely normal, hyperplasia, dysplasia, and malignant. Using FT-SHG, we quantified collagen fiber organization at cellular scales, and noted differences between malignant and other pathological conditions through the metric A.I. ratio. On the other hand, $\chi^2$-SHG was used to infer structural changes in collagen at the molecular scale through the $d$ elements, and in particular, $d_{15}/d_{31}$ showed statistical differences across breast tissue pathologies, except between hyperplasia and normal/dysplasia. We also found that trigonal symmetry (*3m*) is a more appropriate model to describe collagen fibers in malignant tissues as opposed to the conventionally used hexagonal symmetry (*C6*). Furthermore, the percentage of abnormal collagen fibers could potentially be used as a metric for differentiating breast tissue conditions. We have shown that this unique method of targeting collagen fibers using two quantitative SHG techniques seems promising for future breast cancer diagnosis, especially as a complementary technique with gold-standard histopathological method.

## 5.4 Future Work

Immediate future work includes improving upon the initial work on 3D FT-SHG and to make it robust so that it is applicable to real biological samples. It will be particularly useful for quantifying structures such as bone, cornea, and cartilage. In particular, there has been a great deal of interest in knowing the 3D orientation of collagen fibers in bone in order to create artificial bone tissues, and the technique should be able to provide essential information.

Work is already underway to add additional functionalities to the FT-SHG analysis. Initial work has been done to extract more quantitative parameters such as fiber diameters, densities, and location of spacing between the fibers. This should lead to a more thorough analysis of the collagen-based tissues.

We would also like to generate $\chi^2$-image maps in order to obtain useful information from various biological tissues. For example, breast cancer tissue is a great candidate for such an investigation, since we will now be able to see how the fibers change from normal to malignant around the region containing cancerous cells. This will also provide useful information regarding the interaction of cells and the surrounding stroma that is undergoing changes due to disease or cancer progression. We also plan to apply quantitative SHG imaging for extension to clinical *in vitro* breast cancer studies as well as to other types of cancers such as lung and prostate cancer.

We would also like to extend the existing SHG microscope to perform live imaging which we call 4DFT-SHG imaging. By carefully controlling the environment through incubation chambers and appropriate objective lenses, it should be straightforward to set up a live SHG imaging in our lab. Furthermore, for potential *in vivo* studies, we plan to build an SHG endoscope that combines fiber-based femtosecond lasers, fiber-optic catheter, and MEMS-based scanning head systems, and that integrates with both FT-SHG and $\chi^2$-SHG techniques.

Another future work includes the use of longer wavelengths such as 1250 nm from Cr: Forsterite laser. There are two advantages: it can significantly improve the penetration depth leading to a deeper assessment of the tissue, and it also allows acquisition of third-harmonic generation (THG). This generalized (second and third-harmonic imaging) technique would probably be called Fourier transform-harmonic-generation imaging.

## REFERENCES


[1] B. Alberts, A. Johnson, J. Lewis, M. Raff, K. Roberts, and P. Walter, *Molecular Biology of the Cell*. Garland Science, 2008.

[2] P. Fratzl, *Collagen: Structure and Mechanics*, 1 ed. Springer, 2008.

[3] R. C. Billinghurst, L. Dahlberg, M. Ionescu, A. Reiner, R. Bourne, C. Rorabeck, P. Mitchell, J. Hambor, O. Diekmann, H. Tschesche, J. Chen, H. VanWart, and A. R. Poole, "Enhanced cleavage of type II collagen by collagenases in osteoarthritic articular cartilage," *Journal of Clinical Investigation,* vol. 99, pp. 1534-1545, Apr 1997.

[4] D. R. Keene, L. Y. Sakai, and R. E. Burgeson, "Human bone contains type-III collagen, type-VI collagen, and fibrillin - type-III collagen is present on specific fibers that may mediate attachment of tendons, ligaments, and periosteum to calcified bone cortex," *Journal of Histochemistry & Cytochemistry,* vol. 39, pp. 59-69, Jan 1991.

[5] L. Klein and J. Chandrarajan, "Collagen degradation in rat skin but not in intestine during rapid growth - effect on collagen type-1 and type-3 from skin," *Proceedings of the National Academy of Sciences of the United States of America,* vol. 74, pp. 1436-1439, 1977.

[6] Y. Komai and T. Ushiki, "The 3-dimensional organization of collagen fibrils in the human cornea and sclera," *Investigative Ophthalmology & Visual Science,* vol. 32, pp. 2244-2258, Jul 1991.

[7] Y. S. Rabinowitz, "Keratoconus," *Survey of Ophthalmology,* vol. 42, pp. 297-319, Jan-Feb 1998.

[8] P. Ekblom, "Formation of basement-membranes in the embryonic kidney – an immunohistological study," *Journal of Cell Biology,* vol. 91, pp. 1-10, 1981.

[9] M. E. Nimni, "Collagen - structure, function, and metabolism in normal and fibrotic tissues," *Seminars in Arthritis and Rheumatism,* vol. 13, pp. 1-86, 1983.

[10] M. Vanderrest and R. Garrone, "Collagen family of proteins," *Faseb Journal,* vol. 5, pp. 2814-2823, Oct 1991.

[11] S. M. Weis, J. L. Emery, K. D. Becker, D. J. McBride, J. H. Omens, and A. D. McCulloch, "Myocardial mechanics and collagen structure in the osteogenesis imperfecta murine (oim)," *Circulation Research,* vol. 87, pp. 663-669, Oct 2000.

[12] P. P. Provenzano, K. W. Eliceiri, J. M. Campbell, D. R. Inman, J. G. White, and P. J. Keely, "Collagen reorganization at the tumor-stromal interface facilitates local invasion," *Bmc Medicine,* vol. 4, p. 15, Dec 2006.

[13] R. Ambekar, K. C. Toussaint, and A. W. Johnson, "The effect of keratoconus on the structural, mechanical, and optical properties of the cornea," *Journal of the Mechanical Behavior of Biomedical Materials,* vol. 4, pp. 223-236, Apr 2011.

[14] J. R. Mao and J. Bristow, "The Ehlers-Danlos syndrome: on beyond collagens," *Journal of Clinical Investigation,* vol. 107, pp. 1063-1069, May 2001.

[15] P. Caravan, B. Das, S. Dumas, F. H. Epstein, P. A. Helm, V. Jacques, S. Koerner, A. Kolodziej, L. Shen, W. C. Sun, and Z. Zhang, "Collagen-targeted MRI contrast agent for molecular Imaging of fibrosis," *Angewandte Chemie-International Edition,* vol. 46, pp. 8171-8173, 2007.

[16] X. Y. He, E. Spoerl, J. H. Tang, and J. Liu, "Measurement of corneal changes after collagen crosslinking using a noninvasive ultrasound system," *Journal of Cataract and Refractive Surgery,* vol. 36, pp. 1207-1212, Jul 2010.

[17] P. Fratzl, N. Fratzl-Zelman, and K. Klaushofer, "Collagen packing and mineralization - An x-ray scattering investigation of turkey leg tendon," *Biophysical Journal,* vol. 64, pp. 260-266, Jan 1993.

[18] D. J. S. Hulmes, J. C. Jesior, A. Miller, C. Berthet-Colominas, and C. Wolff, "Electron-microscopy shows periodic structure in collagen fibril cross-sections," *Proceedings of the National Academy of Sciences of the United States of America-Biological Sciences,* vol. 78, pp. 3567-3571, 1981.

[19] P. J. Campagnola and L. M. Loew, "Second-harmonic imaging microscopy for visualizing biomolecular arrays in cells, tissues and organisms," *Nature Biotechnology,* vol. 21, pp. 1356-1360, Nov 2003.

[20] G. Cox, E. Kable, A. Jones, I. K. Fraser, F. Manconi, and M. D. Gorrell, "3-dimensional imaging of collagen using second harmonic generation," *Journal of Structural Biology,* vol. 141, pp. 53-62, Jan 2003.

[21] M. Han, G. Giese, and J. F. Bille, "Second harmonic generation imaging of collagen fibrils in cornea and sclera," *Optics Express,* vol. 13, pp. 5791-5797, Jul 2005.

[22] B. R. Masters and P. So, *Handbook of Biomedical Nonlinear Optical Microscopy*. Oxford University, 2008.

[23] G. Popescu, *Nanobiophotonics*. McGraw-Hill, 2010.

[24] H. T. Chen, H. F. Wang, M. N. Slipchenko, Y. K. Jung, Y. Z. Shi, J. B. Zhu, K. K. Buhman, and J. X. Cheng, "A multimodal platform for nonlinear optical microscopy and microspectroscopy," *Optics Express,* vol. 17, pp. 1282-1290, Feb 2009.

[25] W. L. Chen, T. H. Li, P. J. Su, C. K. Chou, P. T. Fwu, S. J. Lin, D. Kim, P. T. C. So, and C. Y. Dong, "Second harmonic generation chi tensor microscopy for tissue imaging," *Applied Physics Letters,* vol. 94, p. 3, May 2009.

[26] S. V. Plotnikov, A. M. Kenny, S. J. Walsh, B. Zubrowski, C. Joseph, V. L. Scranton, G. A. Kuchel, D. Dauser, M. S. Xu, C. C. Pilbeam, D. J. Adams, R. P. Dougherty, P. J. Campagnola, and W. A. Mohler, "Measurement of muscle disease by quantitative second-harmonic generation imaging," *Journal of Biomedical Optics,* vol. 13, p. 11, Jul-Aug 2008.

[27] S. W. Teng, H. Y. Tan, J. L. Peng, H. H. Lin, K. H. Kim, W. Lo, Y. Sun, W. C. Lin, S. J. Lin, S. H. Jee, P. T. C. So, and C. Y. Dong, "Multiphoton autofluorescence and

second-harmonic generation imaging of the ex vivo porcine eye," *Investigative Ophthalmology & Visual Science,* vol. 47, pp. 1216-1224, Mar 2006.

[28] F. Tiaho, G. Recher, and D. Rouede, "Estimation of helical angles of myosin and collagen by second harmonic generation imaging microscopy," *Optics Express,* vol. 15, pp. 12286-12295, Sep 2007.

[29] R. M. Williams, W. R. Zipfel, and W. W. Webb, "Interpreting second-harmonic generation images of collagen I fibrils," *Biophysical Journal,* vol. 88, pp. 1377-1386, Feb 2005.

[30] C. H. Yu, S. P. Tai, C. T. Kung, I. J. Wang, H. C. Yu, H. J. Huang, W. J. Lee, Y. F. Chan, and C. K. Sun, "In vivo and ex vivo imaging of intra-tissue elastic fibers using third-harmonic-generation microscopy," *Optics Express,* vol. 15, pp. 11167-11177, Sep 2007.

[31] N. Morishige, A. J. Wahlert, M. C. Kenney, D. J. Brown, K. Kawamoto, T. Chikama, T. Nishida, and J. V. Jester, "Second-harmonic imaging microscopy of normal human and keratoconus cornea," *Investigative Ophthalmology & Visual Science,* vol. 48, pp. 1087-1094, Mar 2007.

[32] R. LaComb, O. Nadiarnykh, and P. J. Campagnola, "Quantitative second harmonic generation imaging of the diseased state osteogenesis imperfecta: Experiment and simulation," *Biophysical Journal,* vol. 94, pp. 4504-4514, Jun 2008.

[33] P. Matteini, F. Ratto, F. Rossi, R. Cicchi, C. Stringari, D. Kapsokalyvas, F. S. Pavone, and R. Pini, "Photothermally-induced disordered patterns of corneal collagen revealed by SHG imaging," *Optics Express,* vol. 17, pp. 4868-4878, Mar 2009.

[34] A. V. Persikov, J. A. M. Ramshaw, A. Kirkpatrick, and B. Brodsky, "Amino acid propensities for the collagen triple-helix," *Biochemistry,* vol. 39, pp. 14960-14967, Dec 2000.

[35] G. Ramachandran, "Molecular structure of collagen," *International Rev. Connective Tissue Res.,* vol. 1, pp. 127-182, 1963

[36] G. Ramachandran and G. Kartha, "Structure of collagen," *Nature,* vol. 176 pp. 593-595, 1955

[37] A. Rich and F. Crick, "Molecular structure of collagen," *J. Molecular Biol.,* vol. 3, pp. 483-506, 1961

[38] E. J. Miller and S. Gay, "The collagens - an overview and update," *Methods in Enzymology,* vol. 144, pp. 3-41, 1987.

[39] S. Ricard-Blum and F. Ruggiero, "The collagen superfamily: from the extracellular matrix to the cell membrane," *Pathologie Biologie,* vol. 53, pp. 430-442, Sep 2005.

[40] D. R. Eyre, M. A. Paz, and P. M. Gallop, "Cross-linking in collagen and elastin," *Annual Review of Biochemistry,* vol. 53, pp. 717-748, 1984.

[41] M. E. Than, S. Henrich, R. Huber, A. Ries, K. Mann, K. Kuhn, R. Timpl, G. P. Bourenkov, H. D. Bartunik, and W. Bode, "The 1.9-angstrom crystal structure of the noncollagenous (NC1) domain of human placenta collagen IV shows stabilization via

a novel type of covalent Met-Lys cross-link," *Proceedings of the National Academy of Sciences of the United States of America,* vol. 99, pp. 6607-6612, May 2002.

[42] H. Kuivaniemi, G. Tromp, and D. J. Prockop, "Mutations in fibrillar collagens (types I, II, III, and XI), fibril-associated collagen (type IX), and network-forming collagen (type X) cause a spectrum of diseases of bone, cartilage, and blood vessels," *Human Mutation,* vol. 9, pp. 300-315, 1997.

[43] M. Paulsson, "Basement-membrane proteins - structure, assembly, and cellular interactions," *Critical Reviews in Biochemistry and Molecular Biology,* vol. 27, pp. 93-127, 1992.

[44] H. Koga, S. Naito, S. Koto, N. Sakamoto, M. Nakashima, T. Yamasaki, H. Noma, and J. Kumazawa, "Use of bone turnover marker, pyridinoline cross-linked carboxyterminal telopeptide of type I collagen (ICTP), in the assessment and monitoring of bone metastasis in prostate cancer," *Prostate,* vol. 39, pp. 1-7, Apr 1999.

[45] R. R. Bruns, "Beaded filaments and long-spacing fibrils - relation to type-vi collagen," *Journal of Ultrastructure Research,* vol. 89, pp. 136-145, 1984.

[46] D. J. S. Hulmes, "Building collagen molecules, fibrils, and suprafibrillar structures," *Journal of Structural Biology,* vol. 137, pp. 2-10, Jan-Feb 2002.

[47] D. Silver, J. Miller, R. Harrison, and D. J. Prockop, "Helical model of nucleation and propagation to account for the growth of type-i collagen fibrils from symmetrical pointed tips - a special example of self-assembly of rod-like monomers," *Proceedings of the National Academy of Sciences of the United States of America,* vol. 89, pp. 9860-9864, Oct 1992.

[48] D. J. Prockop and K. I. Kivirikko, "Collagens – molecular biology, diseases, and potentials for therapy," *Annual Review of Biochemistry,* vol. 64, pp. 403-434, 1995.

[49] A. Yalovac and N. Ulusu, "Collagen and Collagen Disorders," *J. Pharm. Sci.,* vol. 32, pp. 139-144, 2007.

[50] P. P. Provenzano, D. R. Inman, K. W. Eliceiri, J. G. Knittel, L. Yan, C. T. Rueden, J. G. White, and P. J. Keely, "Collagen density promotes mammary tumor initiation and progression," *BMC Medicine,* vol. 6, p. 15, Apr 2008.

[51] A. F. Chambers and L. M. Matrisian, "Changing views of the role of matrix metalloproteinases in metastasis," *Journal of the National Cancer Institute,* vol. 89, pp. 1260-1270, Sep 1997.

[52] J. T. Erler and V. M. Weaver, "Three-dimensional context regulation of metastasis," *Clinical & Experimental Metastasis,* vol. 26, pp. 35-49, Jan 2009.

[53] M. J. C. Hendrix, E. A. Seftor, D. A. Kirschmann, V. Quaranta, and R. E. B. Seftor, "Remodeling of the microenvironment by aggressive melanoma tumor cells," in *Tissue Remodeling*. vol. 995, M. NilsenHamilton, Z. Werb, and E. Keshet, Eds. New York: New York Acad Sciences, 2003, pp. 151-161.

[54] S. Kauppila, F. Stenback, J. Risteli, A. Jukkola, and L. Risteli, "Aberrant type I and type III collagen gene expression in human breast cancer in vivo," *Journal of Pathology,* vol. 186, pp. 262-268, Nov 1998.

[55] G. Poste and I. J. Fidler, "Pathogenesis of cancer metastasis," *Nature,* vol. 283, pp. 139-146, 1980.

[56] S. Ramaswamy, K. N. Ross, E. S. Lander, and T. R. Golub, "A molecular signature of metastasis in primary solid tumors," *Nature Genetics,* vol. 33, pp. 49-54, Jan 2003.

[57] G. P. Gupta and J. Massague, "Cancer metastasis: Building a framework," *Cell,* vol. 127, pp. 679-695, Nov 2006.

[58] C. E. Brinckerhoff, J. L. Rutter, and U. Benbow, "Interstitial collagenases as markers of tumor progression," *Clinical Cancer Research,* vol. 6, pp. 4823-4830, Dec 2000.

[59] B. Fingleton, "Matrix metalloproteinases: roles in cancer and metastasis," *Frontiers in Bioscience,* vol. 11, pp. 479-491, Jan 2006.

[60] I. Stamenkovic, "Extracellular matrix remodelling: the role of matrix metalloproteinases," *Journal of Pathology,* vol. 200, pp. 448-464, Jul 2003.

[61] D. Kobat, N. G. Horton, and C. Xu, "In vivo two-photon microscopy to 1.6-mm depth in mouse cortex," *Journal of Biomedical Optics,* vol. 16, p. 4, Oct 2011.

[62] R. W. Boyd, *Nonlinear Optics*, 2nd ed.: Academic Press, 2003.

[63] B. A. Saleh and M. C. Teich, *Fundamentals of Photonics*. John Wiley and Sons, 2007.

[64] R. LaComb, O. Nadiarnykh, S. S. Townsend, and P. J. Campagnola, "Phase matching considerations in second harmonic generation from tissues: Effects on emission directionality, conversion efficiency and observed morphology," *Optics Communications,* vol. 281, pp. 1823-1832, Apr 2008.

[65] A. Diaspro, *Confocal and Two-Photon Microscopy: Foundations, Applications and Advances*, 1 ed. Wiley-Liss, 2001.

[66] D. A. Dombeck, K. A. Kasischke, H. D. Vishwasrao, M. Ingelsson, B. T. Hyman, and W. W. Webb, "Uniform polarity microtubule assemblies imaged in native brain tissue by second-harmonic generation microscopy," *Proceedings of the National Academy of Sciences of the United States of America,* vol. 100, pp. 7081-7086, Jun 2003.

[67] W. Drexler and J. G. Fujimoto, *Optical coherence tomography: Technology and Applications*, 1 ed. Springer, 2008.

[68] S. Haykin and B. V. Veen, *Signals and Systems*. Wiley, 2005.

[69] H. G. Adelmann, "Butterworth equations for homomorphic filtering of images," *Computers in Biology and Medicine,* vol. 28, pp. 169-181, Mar 1998.

[70] H. Schomberg and J. Timmer, "The gridding method for image-reconstruction by Fourier transformation," *IEEE Transactions on Medical Imaging,* vol. 14, pp. 596-607, Sep 1995.

[71] H. M. Shieh, C. H. Chung, and C. L. Byrne, "Resolution enhancement in computerized tomographic imaging," *Applied Optics,* vol. 47, pp. 4116-4120, Aug 2008.

[72] J. W. Goodman, *Introduction to Fourier Optics*. McGraw-Hill, 1996.
[73] J. C. Russ, *The Image Processing Handbook*. CRC Press, 2007.
[74] B. Josso, D. R. Burton, and M. J. Lalor, "Texture orientation and anisotropy calculation by Fourier transform and principal component analysis," *Mechanical Systems and Signal Processing,* vol. 19, pp. 1152-1161, Sep 2005.
[75] B. M. Palmer and R. Bizios, "Quantitative characterization of vascular endothelial cell morphology and orientation using Fourier transform analysis," *Journal of Biomechanical Engineering-Transactions of the ASME,* vol. 119, pp. 159-165, May 1997.
[76] P. Stoller, K. M. Reiser, P. M. Celliers, and A. M. Rubenchik, "Polarization-modulated second harmonic generation in collagen," *Biophysical Journal,* vol. 82, pp. 3330-3342, Jun 2002.
[77] J. B. Pawley, *Handbook of Biological Confocal Microscopy*. Springer, 2006.
[78] R. Ambekar Ramachandra Rao, M. R. Mehta, and K. C. Toussaint, "Fourier transform-second-harmonic generation imaging of biological tissues," *Optics Express,* vol. 17, pp. 14534-14542, Aug 2009.
[79] K. Schenke-Layland, "Non-invasive multiphoton imaging of extracellular matrix structures," *Journal of Biophotonics,* vol. 1, pp. 451-462, Dec 2008.
[80] A. H. Reshak, "High second harmonic generation signal from muscles and fascia pig's muscles using the two-photon laser scanning microscope," *Journal of Microscopy-Oxford,* vol. 234, pp. 280-286, Jun 2009.
[81] A. H. Reshak, V. Sarafis, and R. Heintzmann, "Second harmonic imaging of chloroplasts using the two-photon laser scanning microscope," *Micron,* vol. 40, pp. 378-385, Apr 2009.
[82] P. Bianchini and A. Diaspro, "Three-dimensional (3D) backward and forward second harmonic generation (SHG) microscopy of biological tissues," *Journal of Biophotonics,* vol. 1, pp. 443-450, Dec 2008.
[83] F. Legare, C. Pfeffer, and B. R. Olsen, "The role of backscattering in SHG tissue imaging," *Biophysical Journal,* vol. 93, pp. 1312-1320, Aug 2007.
[84] K. Konig, "Clinical multiphoton tomography," *Journal of Biophotonics,* vol. 1, pp. 13-23, Feb 2008.
[85] S. Chu, "Quantitative Analysis of Backward Generation and Backscattering for Epi-collected Second Harmonic Generation in Biological Tissues," *Journal of Medical and Biological Engineering,* vol. 27, pp. 177-182, 2007.
[86] W. Lo, M. Lin, C. Hsueh, W. Chen, S. Lin, and S. Jee, "Forward and backward second harmonic generation imaging of corneal and scleral collagen," in *Proceedings of SPIE, Multiphoton Microscopy in the Biomedical Sciences VIII*, 2008.
[87] R. Ambekar Ramachandra Rao, M. R. Mehta, S. Leithem, and K. C. Toussaint, "Quantitative analysis of forward and backward second-harmonic images of collagen

fibers using Fourier transform second-harmonic-generation microscopy," *Optics Letters,* vol. 34, pp. 3779-3781, Dec 2009.

[88] L. C. Almekinders and J. D. Temple, "Etiology, diagnosis, and treatment of tendonitis: an analysis of the literature," *Medicine and Science in Sports and Exercise,* vol. 30, pp. 1183-1190, Aug 1998.

[89] D. B. Clement, J. E. Taunton, and G. W. Smart, "Achilles tendinitis and peritendinitis - Etiology and treatment," *American Journal of Sports Medicine,* vol. 12, pp. 179-184, 1984.

[90] B. A. Dowling, A. J. Dart, D. R. Hodgson, and R. K. W. Smith, "Superficial digital flexor tendonitis in the horse," *Equine Veterinary Journal,* vol. 32, pp. 369-378, Sep 2000.

[91] T. A. H. Jarvinen, T. L. N. Jarvinen, B. B. Kannus, L. Jozsa, and M. Jarvinen, "Collagen fibres of the spontaneously ruptured human tendons display decreased thickness and crimp angle," *Journal of Orthopaedic Research,* vol. 22, pp. 1303-1309, Nov 2004.

[92] K. M. Khan and J. L. Cook, "Overuse tendon injuries: Where does the pain come from?" *Sports Medicine and Arthroscopy Review,* vol. 8, pp. 17-31, Jan-Mar 2000.

[93] K. M. Khan, J. L. Cook, F. Bonar, P. Harcourt, and M. Astrom, "Histopathology of common tendinopathies - Update and implications for clinical management," *Sports Medicine,* vol. 27, pp. 393-408, Jun 1999.

[94] G. P. Riley, M. J. Goddard, and B. L. Hazleman, "Histopathological assessment and pathological significance of matrix degeneration in supraspinatus tendons," *Rheumatology,* vol. 40, pp. 229-230, Feb 2001.

[95] O. Nadiarnykh, S. Plotnikov, W. A. Mohler, I. Kalajzic, D. Redford-Badwal, and P. J. Campagnola, "Second harmonic generation imaging microscopy studies of osteogenesis imperfecta," *Journal of Biomedical Optics,* vol. 12, p. 9, Sep-Oct 2007.

[96] T. L. Sun, Y. A. Liu, M. C. Sung, H. C. Chen, C. H. Yang, V. Hovhannisyan, W. C. Lin, Y. M. Jeng, W. L. Chen, L. L. Chiou, G. T. Huang, K. H. Kim, P. T. C. So, Y. F. Chen, H. S. Lee, and C. Y. Dong, "Ex vivo imaging and quantification of liver fibrosis using second-harmonic generation microscopy," *Journal of Biomedical Optics,* vol. 15, p. 6, May-Jun 2010.

[97] J. P. Bilezikian, L. G. Raisz, and G. A. Rodan, *Principles of Bone Biology* vol. 1. Academic Press, 2002.

[98] J. A. Buckwalter, M. J. Glimcher, R. R. Cooper, and R. Recker, "Bone biology .II: Formation, form, modeling, remodeling, and regulation of cell-function," *Journal of Bone and Joint Surgery-American Volume,* vol. 77A, pp. 1276-1289, Aug 1995.

[99] M. H. Ross and W. Pawlina, *Histology: A Text and Atlas*, 5th ed. Lippincott Williams & Wilkins, 2010.

[100] X. Wang, J. S. Nyman, X. Dong, H. Leng, and M. Reyes. *Fundamental Biomechanics in Bone Tissue Engineering*. Morgan & Claypool, 2010.

[101] I. Jager and P. Fratzl, "Mineralized collagen fibrils: A mechanical model with a staggered arrangement of mineral particles," *Biophysical Journal,* vol. 79, pp. 1737-1746, Oct 2000.

[102] J. Y. Rho, L. Kuhn-Spearing, and P. Zioupos, "Mechanical properties and the hierarchical structure of bone," *Medical Engineering & Physics,* vol. 20, pp. 92-102, Mar 1998.

[103] S. C. Cowin, *Bone Mechanics Handbook*, 2 ed. Informa Healthcare, 2001.

[104] E. Seeman and P. D. Delmas, "Mechanisms of disease - Bone quality - The material and structural basis of bone strength and fragility," *New England Journal of Medicine,* vol. 354, pp. 2250-2261, May 2006.

[105] P. Zioupos, "Ageing human bone: Factors affecting its biomechanical properties and the role of collagen," *Journal of Biomaterials Applications,* vol. 15, pp. 187-229, Jan 2001.

[106] M. G. Ascenzi, J. Gill, and A. Lomovtsev, "Orientation of collagen at the osteocyte lacunae in human secondary osteons," *Journal of Biomechanics,* vol. 41, pp. 3426-3435, Dec 2008.

[107] M. G. Ascenzi and A. Lomovtsev, "Collagen orientation patterns in human secondary osteons, quantified in the radial direction by confocal microscopy," *Journal of Structural Biology,* vol. 153, pp. 14-30, Jan 2006.

[108] J. Y. Rho, T. Y. Tsui, and G. M. Pharr, "Elastic properties of human cortical and trabecular lamellar bone measured by nanoindentation," *Biomaterials,* vol. 18, pp. 1325-1330, Oct 1997.

[109] B. A. Uthgenannt, M. H. Kramer, J. A. Hwu, B. Wopenka, and M. J. Silva, "Skeletal self-repair: Stress fracture healing by rapid formation and Densification of woven bone," *Journal of Bone and Mineral Research,* vol. 22, pp. 1548-1556, Oct 2007.

[110] H. B. Wang, J. K. Lee, A. M. Moursi, D. Anderson, P. Winnard, H. Powell, and J. Lannutti, "Microstructural disassembly of calcium phosphates," *Journal of Biomedical Materials Research Part A,* vol. 68A, pp. 61-70, Jan 2004.

[111] M. Tzaphlidou, "The role of collagen in bone structure: An image processing approach," *Micron,* vol. 36, pp. 593-601, 2005.

[112] M. Tzaphlidou and P. Berillis, "Collagen fibril diameter at different cortical bone sites," *Bone,* vol. 36, pp. S198-S198, Jun 2005.

[113] P. Braidotti, F. P. Branca, and L. Stagni, "Scanning electron microscopy of human cortical bone failure surfaces," *Journal of Biomechanics,* vol. 30, pp. 155-162, Feb 1997.

[114] D. N. Menton, D. J. Simmons, S. L. Chang, and B. Y. Orr, "From bone lining cell to osteocyte—an SEM study," *Anatomical Record,* vol. 209, pp. 29-39, 1984.

[115] L. Bergmans, P. Moisiadis, B. Van Meerbeek, M. Quirynen, and P. Lambrechts, "Microscopic observation of bacteria: review highlighting the use of environmental SEM," *International Endodontic Journal,* vol. 38, pp. 775-788, Nov 2005.

[116] F. J. Doucet, J. R. Lead, L. Maguire, E. P. Achterberg, and G. E. Millward, "Visualisation of natural aquatic colloids and particles - a comparison of conventional high vacuum and environmental scanning electron microscopy," *Journal of Environmental Monitoring,* vol. 7, pp. 115-121, Feb 2005.

[117] A. Boyde and C. M. Riggs, "The quantitative study of the orientation of collagen in compact-bone slices," *Bone,* vol. 11, pp. 35-39, 1990.

[118] M. Portigliatti Barbos, P. Bianco, A. Ascenzi, and A. Boyde, "Collagen orientation in compact bone: II. Distribution of lamellae in the whole of the human femoral shaft with reference to its mechanical properties," *Metabolic bone disease & related research,* vol. 5, pp. 309-15, 1984 1984.

[119] C. M. Riggs, L. C. Vaughan, G. P. Evans, L. E. Lanyon, and A. Boyde, "Mechanical implications of collagen fiber orientation in cortical bone of the equine radius," *Anatomy and Embryology,* vol. 187, pp. 239-248, Mar 1993.

[120] M. Strupler, A. M. Pena, M. Hernest, P. L. Tharaux, J. L. Martin, E. Beaurepaire, and M. C. Schanne-Klein, "Second harmonic imaging and scoring of collagen in fibrotic tissues," *Optics Express,* vol. 15, pp. 4054-4065, Apr 2007.

[121] A. Zoumi, A. Yeh, and B. J. Tromberg, "Imaging cells and extracellular matrix in vivo by using second-harmonic generation and two-photon excited fluorescence," *Proceedings of the National Academy of Sciences of the United States of America,* vol. 99, pp. 11014-11019, Aug 2002.

[122] J. Burket, S. Gourion-Arsiquaud, L. M. Havill, S. P. Baker, A. L. Boskey, and M. C. H. van der Meulen, "Microstructure and nanomechanical properties in osteons relate to tissue and animal age," *Journal of Biomechanics,* vol. 44, pp. 277-284, Jan 2011.

[123] J. Caetano-Lopes, A. M. Nery, H. Canhao, J. Duarte, R. Cascao, A. Rodrigues, I. P. Perpetuo, S. Abdulghani, P. M. Amaral, S. Sakaguchi, Y. T. Konttinen, L. Graca, M. F. Vaz, and J. E. Fonseca, "Chronic arthritis leads to disturbances in the bone collagen network," *Arthritis Research & Therapy,* vol. 12, p. 7, 2010.

[124] W. Mohler, A. C. Millard, and P. J. Campagnola, "Second harmonic generation imaging of endogenous structural proteins," *Methods,* vol. 29, pp. 97-109, Jan 2003.

[125] R. Ambekar, M. Chittenden, I. Jasiuk, and K. C. Toussaint, Jr., "Quantitative second-harmonic generation microscopy for imaging porcine cortical bone: Comparison to SEM and its potential to investigate age-related changes," *Bone,* vol. 50, pp. 643-50, 2012 Mar (Epub 2011 Dec 2012.

[126] M. G. Ascenzi, A. Ascenzi, A. Benvenuti, M. Burghammer, S. Panzavolta, and A. Bigi, "Structural differences between "dark" and "bright" isolated human osteonic lamellae," *Journal of Structural Biology,* vol. 141, pp. 22-33, Jan 2003.

[127] J. G. Skedros, K. J. Hunt, P. E. Hughes, and H. Winet, "Ontogenetic and regional morphologic variations in the turkey ulna diaphysis: Implications for functional adaptation of cortical bone," *Anatomical Record Part a-Discoveries in Molecular Cellular and Evolutionary Biology,* vol. 273A, pp. 609-629, Jul 2003.

[128] S. C. Su, J. G. Skedros, K. N. Bachus, and R. D. Bloebaum, "Loading conditions and cortical bone construction of an artiodactyl calcaneus," *Journal of Experimental Biology,* vol. 202, pp. 3239-3254, Nov 1999.

[129] L. A. Feng and I. Jasiuk, "Multi-scale characterization of swine femoral cortical bone," *Journal of Biomechanics,* vol. 44, pp. 313-320, Jan 2011.

[130] T. Matsumoto, N. Ando, T. Tomii, and K. Uesugi, "Three-Dimensional Cortical Bone Microstructure in a Rat Model of Hypoxia-Induced Growth Retardation," *Calcified Tissue International,* vol. 88, pp. 54-62, Jan 2011.

[131] J. G. Skedros and K. J. Hunt, "Does the degree of laminarity correlate with site-specific differences in collagen fibre orientation in primary bone? An evaluation in the turkey ulna diaphysis," *Journal of Anatomy,* vol. 205, pp. 121-134, Aug 2004.

[132] A. Jemal, F. Bray, M. M. Center, J. Ferlay, E. Ward, and D. Forman, "Global Cancer Statistics," *Ca-a Cancer Journal for Clinicians,* vol. 61, pp. 69-90, Mar-Apr 2011.

[133] "Cancer Facts & Figures - 2012," Atlanta, GA: American Cancer Society, 2012.

[134] B. N. Datta, *Textbook of Pathology*, 2nd ed. Jaypee Brothers Medical Publishers, 2008.

[135] S. Srivastava, *Molecular Pathology of Early Cancer*. Ios Press Inc, 1998.

[136] J. E. Ferguson, A. M. Schor, A. Howell, and M. W. J. Ferguson, "Changes in the extracellular-matrix of the normal human breast during the menstrual cycle," *Cell and Tissue Research,* vol. 268, pp. 167-177, Apr 1992.

[137] L. A. Liotta, C. N. Rao, and S. H. Barsky, "Tumor invasion and the extracellular matrix," *Laboratory Investigation,* vol. 49, pp. 636-649, 1983.

[138] O. W. Petersen, H. L. Nielsen, T. Gudjonsson, R. Villadsen, F. Rank, E. Niebuhr, M. J. Bissell, and L. Ronnov-Jessen, "Epithelial to mesenchymal transition in human breast cancer can provide a nonmalignant stroma," *American Journal of Pathology,* vol. 162, pp. 391-402, Feb 2003.

[139] D. Radisky, J. Muschler, and M. J. Bissell, "Order and disorder: The role of extracellular matrix in epithelial cancer," *Cancer Investigation,* vol. 20, pp. 139-153, 2002.

[140] J. Helleman, M. Jansen, K. Ruigrok-Ritstier, I. L. van Staveren, M. P. Look, M. E. M. Gelder, A. M. Sieuwerts, J. G. M. Klijn, S. Sleijfer, J. A. Foekens, and E. Berns, "Association of an extracellular matrix gene cluster with breast cancer prognosis and endocrine therapy response," *Clinical Cancer Research,* vol. 14, pp. 5555-5564, Sep 2008.

[141] S. E. Holton, M. J. Walsh, and R. Bhargava, "Subcellular localization of early biochemical transformations in cancer-activated fibroblasts using infrared spectroscopic imaging," *Analyst,* vol. 136, pp. 2953-2958, 2011.

[142] S. E. Holton, M. J. Walsh, A. Kajdacsy-Balla, and R. Bhargavatt, "Label-Free Characterization of Cancer-Activated Fibroblasts Using Infrared Spectroscopic Imaging," *Biophysical Journal,* vol. 101, pp. 1513-1521, Sep 2011.

[143] D. Barkan, J. E. Green, and A. F. Chambers, "Extracellular matrix: A gatekeeper in the transition from dormancy to metastatic growth," *European Journal of Cancer,* vol. 46, pp. 1181-1188, May 2010.

[144] C. Thrasivoulou, G. Virich, T. Krenacs, I. Korom, and D. L. Becker, "Optical delineation of human malignant melanoma using second harmonic imaging of collagen," *Biomedical Optics Express,* vol. 2, pp. 1282-1295, May 2011.

[145] M. Sivaguru, S. Durgam, R. Ambekar, D. Luedtke, G. Fried, A. Stewart, and K. C. Toussaint, "Quantitative analysis of collagen fiber organization in injured tendons using Fourier transform-second harmonic generation imaging," *Optics Express,* vol. 18, pp. 24983-24993, Nov 2010.

[146] J. T. Kwak, R. Reddy, S. Sinha, and R. Bhargava, "Analysis of Variance in Spectroscopic Imaging Data from Human Tissues," *Analytical Chemistry,* vol. 84, pp. 1063-1069, Jan 2012.

[147] D. C. Fernandez, R. Bhargava, S. M. Hewitt, and I. W. Levin, "Infrared spectroscopic imaging for histopathologic recognition," *Nature Biotechnology,* vol. 23, pp. 469-474, Apr 2005.

[148] I. W. Levin and R. Bhargava, "Fourier transform infrared vibrational spectroscopic imaging: Integrating microscopy and molecular recognition," in *Annual Review of Physical Chemistry*. vol. 56 Palo Alto: Annual Reviews, 2005, pp. 429-474.

[149] D. A. Forsyth and J. Ponce, *Computer Vision: A Modern Approach.* Prentice Hall, 2011.

[150] H. F. Ding, F. Nguyen, S. A. Boppart, and G. Popescu, "Optical properties of tissues quantified by Fourier-transform light scattering," *Optics Letters,* vol. 34, pp. 1372-1374, May 2009.

[151] W. F. Cheong, S. A. Prahl, and A. J. Welch, "A review of the optical-properties of biological tissues," *IEEE Journal of Quantum Electronics,* vol. 26, pp. 2166-2185, Dec 1990.

[152] R. Richards-Kortum and E. SevickMuraca, "Quantitative optical spectroscopy for tissue diagnosis," *Annual Review of Physical Chemistry,* vol. 47, pp. 555-606, 1996.

[153] N. Lue, J. Bewersdorf, M. D. Lessard, K. Badizadegan, R. R. Dasari, M. S. Feld, and G. Popescu, "Tissue refractometry using Hilbert phase microscopy," *Optics Letters,* vol. 32, pp. 3522-3524, Dec 2007.

[154] I. Freund, M. Deutsch, and A. Sprecher, "Connective-tissue polarity - Optical 2nd harmonic microscopy, crossed-beam summation, and small-angle scattering in rat-tail tendon," *Biophysical Journal,* vol. 50, pp. 693-712, Oct 1986.

[155] P. J. Su, W. L. Chen, T. H. Li, C. K. Chou, T. H. Chen, Y. Y. Ho, C. H. Huang, S. J. Chang, Y. Y. Huang, H. S. Lee, and C. Y. Dong, "The discrimination of type I and type II collagen and the label-free imaging of engineered cartilage tissue," *Biomaterials,* vol. 31, pp. 9415-9421, Dec 2010.

[156] D. Ait-Belkacem, A. Gasecka, F. Munhoz, S. Brustlein, and S. Brasselet, "Influence of birefringence on polarization resolved nonlinear microscopy and collagen SHG structural imaging," *Optics Express,* vol. 18, pp. 14859-14870, Jul 2010.

[157] I. Gusachenko, G. Latour, and M. C. Schanne-Klein, "Polarization-resolved Second Harmonic microscopy in anisotropic thick tissues," *Optics Express,* vol. 18, pp. 19339-19352, Aug 2010.

[158] B. Y. Jiang and S. W. Chu, "Trigonal symmetry of type i collagen probed by shg polarization anisotropy," in *2008 Conference on Quantum Electronics and Laser Science Conference on Lasers and Electro-Optics, CLEO/QELS*, 2008.

[159] X. Han, R. M. Burke, M. L. Zettel, P. Tang, and E. B. Brown, "Second harmonic properties of tumor collagen: determining the structural relationship between reactive stroma and healthy stroma," *Optics Express,* vol. 16, pp. 1846-1859, Feb 2008.

[160] T. Hompland, A. Erikson, M. Lindgren, T. Lindmo, and C. D. Davies, "Second-harmonic generation in collagen as a potential cancer diagnostic parameter," *Journal of Biomedical Optics,* vol. 13, p. 11, Sep-Oct 2008.

[161] Z. Y. Zhuo, C. S. Liao, C. H. Huang, J. Y. Yu, Y. Y. Tzeng, W. Lo, C. Y. Dong, H. C. Chui, Y. C. Huang, H. M. Lai, and S. W. Chu, "Second harmonic generation imaging - A new method for unraveling molecular information of starch," *Journal of Structural Biology,* vol. 171, pp. 88-94, Jul 2010.

[162] O. De Wever and M. Mareel, "Role of tissue stroma in cancer cell invasion," *Journal of Pathology,* vol. 200, pp. 429-447, Jul 2003.

[163] S. J. Han, E. Makareeva, N. V. Kuznetsova, A. M. DeRidder, M. B. Sutter, W. Losert, C. L. Phillips, R. Visse, H. Nagase, and S. Leikin, "Molecular Mechanism of Type I Collagen Homotrimer Resistance to Mammalian Collagenases," *Journal of Biological Chemistry,* vol. 285, pp. 22276-22281, Jul 2010.

[164] E. Makareeva, S. J. Han, J. C. Vera, D. L. Sackett, K. Holmbeck, C. L. Phillips, R. Visse, H. Nagase, and S. Leikin, "Carcinomas Contain a Matrix Metalloproteinase-Resistant Isoform of Type I Collagen Exerting Selective Support to Invasion," *Cancer Research,* vol. 70, pp. 4366-4374, Jun 2010.

[165] M. Hidalgo and S. G. Eckhardt, "Development of matrix metalloproteinase inhibitors in cancer therapy," *Journal of the National Cancer Institute,* vol. 93, pp. 178-193, Feb 2001.

## APPENDIX A: PREPARATION OF TYPE I COLLAGEN SCAFFOLDS

The preparation of type I collagen scaffolds requires the following chemicals: high concentration rat tail collagen from BD Biosciences (Catalog no. 354236), sterile 10x phosphate buffer solution (PBS), sterile distilled water/ molecular grade water, and 1N sodium hydroxide (NaOH) solution. Details can be also found on BD biosciences website.

1. First, all the chemicals mentioned above contained in sterile test tubes are placed on ice for ~ 5-10 minutes. Meanwhile, coverslips, O-rings and mixing tube are sterilized using ethanol. The incubator temperature is set to 35°C.
2. Then, calculate the volume of the chemicals to be mixed. It is found that a desired concentration of 0.5 mg/ml collagen gel generates collagen fibers that are well separated, thereby making it easier to obtain measurements on individual fibers. The total volume of collagen solution is chosen to be 500 µl, which allows one to make many samples (in their respective wells/ petri-dish) of collagen scaffolds at different conditions.
   i. Volume of 10X PBS = Total volume/10 = 500/10 = 50 µl.
   ii. Volume of high concentration collagen = Total volume x desired concentration/ concentration in bottle = 500 x 0.5/10.68 = 23.4 µl.
   iii. Volume of 1N NaOH = Volume of high concentration collagen (ml) x 0.023 ml = 0.023x0.023 = 0.54 µl.
   iv. Finally, the volume of distilled water = Total volume - Volume of 10X PBS - Volume of high concentration collagen - Volume of 1N NaOH = 0.5 - 0.023 - 0.00054 - 0.05 = 426 µl.
3. Pipette the calculated volume of chemicals into the mixing tube and mix them well.
4. Take three coverslips and place O-rings on top of each coverslip. Then, pipette 100 µl each on to the coverslips from the mixing tube, place them in a small petri dish and cover them tight with a parafilm to avoid evaporation during the curing process. Place one of them in an incubator at 35°C for 1 hour; this produces thinner collagen fibers. Place the second one in the fridge at 4°C for 2 days; this produces fibers that are relatively thicker. Leave the third sample at room temperature for a day; this produces fibers with

thicknesses between the first and second sample. Some degree of control over fiber diameter can also be obtained through controlling the pH; however, we have noticed that the effect is roughly the same as controlling the temperature of curing.